Space-Time Rupture Properties of Large Earthquakes

by

Jeffrey Joseph McGuire

Submitted to the Department of Earth, Atmospheric, and Planetary Science
in partial fulfillment of the requirements for the degree of

Doctor of Philosophy

at the

MASSACHUSETTS INSTITUTE OF TECHNOLOGY

June 2000

Author ....
Department of Earth, Atmospheric, and Planetary Science
March, 21, 2000

Certified by ....
Thomas H. Jordan
Professor
Thesis Supervisor

Accepted by ....
Ronald G. Prinn
Department Head

Space-Time Rupture Properties of Large Earthquakes

by

Jeffrey Joseph McGuire

Submitted to the Department of Earth, Atmospheric, and Planetary Science
on March, 21, 2000, in partial fulfillment of the
requirements for the degree of
Doctor of Philosophy

Abstract

Slow earthquakes have been hypothesized to be compound events, i.e. comprised of both an ordinary earthquake and a smooth moment-release transient of longer duration. Low-frequency normal-mode based studies which support the compound event hypothesis have suggested that low-frequency source-spectra of some slow earthquakes require that the slow-component initiated before the fast component. We present observations of low-frequency P-wave energy arriving prior to the high-frequency, mainshock for two oceanic transform fault events. Both the 1994, M_w 7.0, Romanche and 1997, M_w 6.8, Prince Edward Island events show clear time-domain evidence for episodes of smooth moment release that preferentially radiated energy at low-frequencies. Inversions for the moment-rate functions of these events yield compound event sequences where the derivative of the moment-rate function is 2-3 orders of magnitude smaller during the slow event than during the ordinary fast event. The smoothness of the moment-rate function implies that the smooth components of the compound events have rupture and slip velocities which are orders of magnitude smaller than those during ordinary earthquakes.

Determining the space-time rupture histories of earthquakes that are only recorded teleseismically is a difficult and non-unique process. We developed a method to determine the 2nd degree polynomial moments of an earthquake's space-time moment-release distribution using frequency dependent measurements of global surface- and body-wave arrivals. Our method incorporates both current 3-D earth models and the physical constraint that the source-region have non-negative volume. The 2nd moments provide estimates of the duration, spatial extent, and directivity of an event's rupture. In addition, they can be used to systematically resolve the fault-plane ambiguity. Our values of the 2nd moments for the 1995, M_w 8.0, Jalisco Mexico earthquake agree well with those determined from local slip inversions, and our inversion for the 1st-degree moments of the 1995 Kobe earthquake shows that the measurement errors resulting from unmodeled lateral heterogeneity are small. By estimating the 2nd moments for a catalog of large earthquakes, we are able to systematically resolve the fault-plane ambiguity on a global scale.

While the 2nd moments of most large earthquakes are aligned along one of the candidate fault-planes of the event's moment tensor, the 2nd moments of the Romanche and Prince Edwards events are oriented at a high angle to both of their candidate fault-planes. The only type of source-model that can satisfy the observed 0th, 1st, and 2nd degree moments of these events is one that involves slip on two parallel faults. This observation agrees with subevent locations determined using travel-time picks which suggest that multiple parallel faults ruptured in both of these earthquakes. The geometry of both event sequences is consistent with a scenario in which a slow-event on the main transform fault redistributes stress in the region, triggering subevents on both the main and sub-parallel adjacent faults. This evidence for co-seismic rupture of multiple faults combined with other seismic and marine geologic data suggest that deformation at oceanic transforms can be distributed over a wide region (~100 km) on both long (geologic) and short (co-seismic) time-scales.

Thesis Supervisor: Thomas H. Jordan
Title: Professor

Acknowledgments

MIT has been a fascinating place to learn geophysics, and I'm grateful for the chance to have been a student here. Tom Jordan, my advisor, has shared with me both his astonishing grasp of seismology and his philosophy of how to solve seismological problems. I will definitely miss the process of working through my research difficulties on his office chalkboard. Perhaps the best thing Tom does for his students is to include them in a great research group. I am greatful to Li Zhao both for his collaboration on the technique for determining the 2nd moments of earthquake sources (Chapter 4) and for always knowing the answers to my questions. Pierre Ihmlé managed to teach me the inner workings of his various source-spectrum estimation codes over email and contributed significantly to Chapters 2 and 3. I've learned an enormous amount over the years from my fellow Jordan-group members; whether discussing the little tricks associated with GSDF or enjoying a post group meeting swim, I've benefited from being around Eliza Richardson, Jim Gaherty, Peter Puster, Rafi Katzman, Jun Korenaga, Rebecca Saltzer, Liangjun Chen, Margaret Boettcher, and Marion Freybourger.

My committee, Chris Marone, Rob van der Hilst, Leigh Royden, Jian Lin, and Tom Jordan, have greatly improved this thesis over the last few months. Chris Marone, Jim Rice, and Jereon Tromp taught the most interesting, effective, and useful geophysics classes I've ever taken. I've also benefited over the last five years from scientific discussions with John Collins, Jian Lin, Ross Stein, Göran Ekström, Chris Marone, and Greg Beroza. My fellow EAPS students have made life both within and beyond the Green Building educational and fun, particuraly Frederick Simons, Harfnkell Karason, John Castle, Sebastien Chevrot, Mark Behn, Shijie Zhong, Phil Tracadas, Laurent Montesi, Oded Aharonson, Steve Karner, Karen Mair, Kevin Frye, Katy Quin, Brendan Meade, Noah Snyder, Eric Kirby, and Olav van Genabeek.

I never would have discovered my interest in seismology or decided to enter graduate school without the influence of a few Wash-U people. Doug Wiens introduced me to seismology and really encouraged me to explore research. Now that I have more appreciation of the demands placed on a young professor's time, I am amazed at how much of his Doug spent on me. In addition to teaching me about good stuff like digitizing, nplot, P-waves, fortran, and focal mechanisms, Laura Reiser Wetzel and Megan Flanagan were great examples of what being a graduate student is all about. Megan continues to be an amazingly supportive friend. Rafi and Niva Katzman made my and Abby's first few years in Cambridge a lot more fun, and I miss them greatly. Since we met at field camp years ago, Clint Conrad and I have gone through many of the same decisions and experiences, making his friendship and perspective invaluable.

My brother, Mark, has always been both inspiring and unpredictable, and I hope he never stops. I'm grateful to my parents, Joe and Darlene McGuire, for providing me with every opportunity I could want and then giving me the support and encouragement to go after whatever I chose.

And Abby, as usual I'm completely amazed by her. Finishing a thesis is never fun, but I can't imagine pulling it off despite months of all-day 'morning' sickness and a spouse that was too preoccupied with his own thesis to be of much help. She's made grad-school both endurable and enjoyable, and I'm looking forward to moving on with her and the kicking one.

To my parents.

Contents

Chapter 1

Introduction

Faults in the Earth's crust rupture in slip events that range in duration from less than one second for small earthquakes to the nearly continuous creep that occurs along the central San Andreas fault. The spatial and temporal extent of any earthquake can be measured by the characteristic rupture length, L_c, and the characteristic duration, τ_c, which are defined in terms of the second central moments of the stress-glut-rate tensor [Backus and Mulcahy, 1976a, 1796b; Backus 1977a, 1977b; Silver and Jordan 1983, Chapter 4]. The ratio of these dimensions gives the characteristic rupture velocity, v_c. In an ordinary earthquake, the instability propagates at close to the shear-wave velocity of the surrounding elastic medium resulting in a v_c of ~3-4 km/s in the crust. However, various studies have shown that there are instabilities or fault-slip transients that have characteristic velocities which are orders of magnitude lower than what occurs in an ordinary earthquake but remain well above the velocities associated with steady-state creep (~10 cm/yr). These slow slip transients range over several orders of magnitude in both characteristic duration, τ_c, and velocity, v_c (Figure 1-1).

The term 'slow earthquake' ($v_c < \sim 1$ km/s) denotes events which include ordinary subevents that produce high-frequency radiation, but slow earthquakes have unusually long total durations for their seismic moments and produce a level of low-frequency excitation that is anomalously large relative to their high-frequency excitation. Silent earthquakes ($v_c < \sim 100$ m/s) are events that lack any periods of high-speed rupture propagation and hence do not radiate high-frequency energy.

Events associated with the band that includes the lower end of the slow-earthquakes ($v_c < \sim 0.5$ km/s) and the silent earthquakes are difficult to study. They are not always documented in the standard earthquake catalogs owing to their lack of high-frequency radiation. High quality data has been lacking for these events because they span the frequency range from the lower-most end of the seismic-spectrum, where background noise limits study to only the largest events (Beroza and Jordan, 1990), to the upper end of the geodetic spectrum where strain-meter instruments often do not sample at a fast-enough rate to capture the rupture propagation of the transient (Linde *et al.*, 1996). Additionally strain-meter type data is limited to only the most-well instrumented geographic areas. Despite these difficulties, geodetic observations have documented clear slow-slip transients with durations as short as 40 min (Linde *et al.*, 1996). Higher-sensitivity instruments have suggested that a single swarm of slow-earthquakes can have events ranging in duration from as short as 10 s to as long as 10^3 s (Crescentini *et al.*, 1999); however, these events were too small to be detected seismically. Seismic observations of large ($M_w \sim 8$) subduction zone thrust events have established that some events, such as the 1960 Peru (Pelayo and Wiens, 1990) and 1992 Nicaragua earthquakes (Kanamori and Kikuchi, 1993) can have durations ($\sim$ 100 s) that are at least a factor of 2 longer than ordinary M$\sim$8 earthquakes. In these events, the rupture front slows down to velocities of $\sim$0.5 km/s when it reaches the shallow portion of the thrust interface owing to either the low rigidity of the sediments in the acretionary wedge or to their velocity strengthening frictional character. Despite these well-established seismically and geodetically observed slow-slip transients the range of behavior between them has been difficult to constrain.

Several studies have targeted the region corresponding to durations from tens to thousands of seconds and sizes from $M_w \sim 5$ to $M_w \sim 7.5$ by examining excitations of the Earth's lowest frequency normal-modes. Beroza and Jordan (1990) used the data available in the 1980s from the IDA network and found excitation of these modes at times when no ordinary earthquake could account for it. This potential evidence for slow and silent earthquakes is hard to interpret both because of the

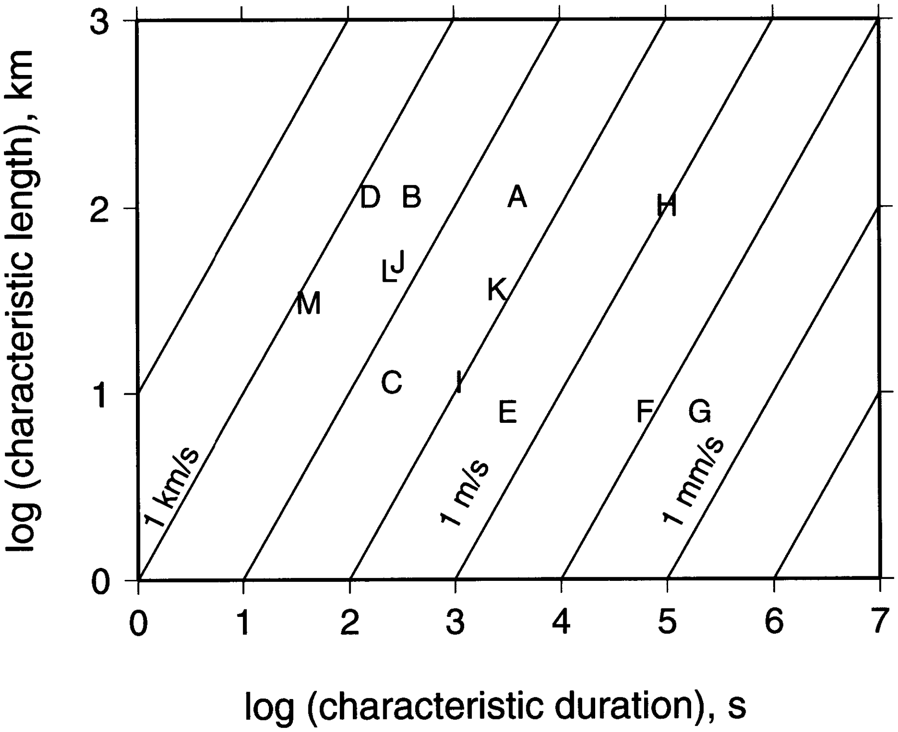

Figure 1-1: Slow and silent earthquakes, after Beroza and Jordan (1990). A June 6, 1960 Chile (Kanamori and Stewart, 1979), B the 1896 Sanriku earthquake (Kanamori, 1972), C the 1997 Apennines sequence (Crescentini *et al.*, 1999), D the 1960 Peru earthquake (Pelayo and Wiens, 1990), E-G San Andreas fault slow earthquakes (Linde *et al.*, 1996), H the 1992 Sanriku-Oki earthquake (Kawasaki *et al.*, 1995), I precursors to the 1976 Friuli earthquake (Bonafede *et al.*, 1983), J the 1946 Aleutian Islands earthquake (Kanamori, 1972; Abe, 1973), K the 1978 Izu-Oshima earthquake (Sacks *et al.*, 1981), L 1994 Romanche Slow earthquake (Chapter 2), M 1997 Prince Edwards earthquake, (Chapter 3).

limits of the IDA network and the more recent observation of continuous excitation of the Earth's normal-modes (Naoki and Kiwamu, 1998; Nawa, 1998; Suda *et al.*, 1998) possibly by atmospheric pressure variations. Shearer (1994) identified 40 slow events by applying a matched-filter algorithm to the IDA data in a slightly higher frequency band than that studied by Beroza and Jordan (1990). Jordan (1991), Ihmlé *et al.* (1993), and Ihmlé and Jordan (1994) targeted slow-slip events by looking for earthquakes that had sufficient high-frequency radiation to be included in earthquake catalogs but which also showed anomalously large excitation of low-frequency modes. They surmised that these earthquakes were "compound events" comprising both an ordinary event that accounted for the high-frequency radiation as well as a smooth transient of longer duration that accounted for the unexpectedly large excitation seen in the low-frequency modes.

One event in particular, the 1989 M_w 8.2 Macquarie ridge earthquake, showed unexpectedly large excitation of low-frequency modes and anomalies in the phase of these modes that could be explained by smooth moment-release prior to the event's high-frequency origin time (Ihmlé *et al.*, 1993; Park, 1990; Kedar *et al.*, 1994). However, there was a complete lack of any observable precursory energy arriving at nearby ($\Delta \sim 20°$) high-gain seismometers (Ihmlé *et al.*, 1993; Kedar *et al.*, 1994). Ihmlé *et al.* (1993) showed that the precursor would show no observable signal at the regional seismic stations if the source-time-function (STF) of the Macquarie earthquake was sufficiently smooth in the interval preceding the onset of ordinary seismic rupture. The STF, $\dot{\mathrm{M}}(t)$, is the time derivative of the seismic moment release function. For it to be smooth, its derivative, the moment acceleration, $\ddot{M}(t)$, must be small. In a simple model of a unilateral (Haskell) rupture on a rectangular fault $\dot{M}$ initially increases as, $\ddot{M} = 2\mu W v_r \Delta\dot{u}$, where μ is the shear modulus, W is the fault width, v_r is the rupture velocity, and $\Delta\dot{u}$ is the particle slip velocity. Thus, for the Macquarie precursor, which occurred at a depth >30km and had a seismic moment of 3x10^{20} Nm, to have had low values of $\ddot{M}$, the product of the rupture and particle slip velocities, $v_r\Delta\dot{u}$, must have been several orders of magnitude smaller than the value corresponding to an ordinary earthquake (i.e. the precursor probably had a small characteristic velocity, v_c). While such a slow precursor would not have been visible on the regional seismic recordings, Kedar *et al.* (1994) found the lack of an observable precursor before the high-frequency P-wave arrival time to be sufficient evidence to reject the slow-precursor hypothesis.

In Chapters 2 and 3 of this thesis we document observable low-frequency energy arriving before the high-frequency P-wave for two oceanic transform fault-events, the 1994, M_w 7.0, Romanche and 1997, M_w 6.8, Prince Edward's Island earthquakes. Low-pass filtered recordings of the P waves for these events show smooth ramps that began well before the arrival of the high-frequency waves from their mainshocks. These initial ramps require slip-events that released significant amounts of seismic moment while radiating little to no high-frequency energy. Both events show a strong roll-off in their amplitude spectra similar to the events studied by Ihmlé and Jordan (1994). We performed joint inversions of the low-frequency P waveforms and spectral data for these events to determine their STFs. The events show remarkably similar compound-event behavior. They are comprised of an episode of smooth moment release that lasts for 200 and 30 s for the Romanche and Prince Edwards events respectively, as well as an ordinary mainshock that accounts for the majority of the seismic moment in each event despite having an order of magnitude shorter duration than the respective slow component. For both events, the STFs have values of $\ddot{M}$ during the slow component that are 2-3 orders of magnitude smaller than those observed during the mainshock, implying lower values of v_r and/or $\Delta\dot{u}$.

Arrival-time picks of various subevents in the Romanche and Prince Edward's Island earthquakes suggest an unusual space-time relationship with the subevents rupturing more than one fault. This is a particularly important observation to constrain because the space-time distribution provides a clue to the mechanical relationship between the slow and fast episodes of deformation in these earthquakes. If the slow precursor ruptured the same section of the fault as the mainshock, the precursor might be an unusually large nucleation phase that accelerated into an ordinary rupture, similar to nucleation phases observed in California earthquakes (Ellsworth and Beroza, 1995). However, if the slow and fast events occurred on different faults, the slow event may have triggered the fast event by redistributing stress within the focal region. Unfortunately, owing to the lack of nearfield data for oceanic transform fault events, it is difficult to determine the precise spatial relationship. While the travel-time picks presented in Chapters 2 and 3 are suggestive of multiple faults failing in one event, they suffer from uncertainties in picking the later arrivals in the middle of the P-wave group.

Determining the space-time rupture history of an earthquake that is only recorded teleseismically is a difficult and non-unique inverse problem. Typical teleseismic inversions assume an *a priori* source model, such as a series of point-sources (Kikuchi and Kanamori, 1991) with triangular STFs, and find the contribution of each point-source that optimizes the fit to the P-wave data. Other methods solve for the slip in individual elements on a densely gridded fault-plane by stabilizing the inversion with a smoothing constraint. However, P waves can be insensitive to the total moment in a large earthquake (Ekström, 1989), and the choice of smoothing parameter is often arbitrary. Recently Ihmlé (1998) showed that for the M_w 8.2 Bolivia deep earthquake teleseismic P-wave inversions are unable to differentiate between a slip distribution composed of compact subevents and one composed of widely distributed slip due to the uncertainty in the smoothing parameter. This is a particularly discouraging observation for M$\sim$7 shallow earthquakes, such as the Romanche and Prince Edward's Island events, because determining the details of their rupture histories requires resolving finer spatial scales and modeling more complicated P-wave Green's functions than were involved in the Bolivia event. In Chapter 4 we develop a method for determining certain well-resolved properties of an earthquake's space-time rupture history, such as L_c, τ_c, and v_c, that go beyond a point-source representation without assuming an *a priori* source model or any ad hoc smoothing parameter.

The space-time distribution of moment release in an earthquake is described by the stress-glut rate tensor, $\dot{\mathbf{\Gamma}}(\mathbf{r}, t)$. In Chapter 4, we develop a method for determining the 1st and 2nd degree polynomial moments of $\dot{\mathbf{\Gamma}}(\mathbf{r}, t)$ from frequency-dependent measurements of the phase-delay and amplitude differences between data seismograms and synthetic seismograms calculated for a point-source in a 3-D Earth model. While the theory of 2nd degree moments was first developed in the 1970's (Backus and Mulcahy, 1976a,b), developing inversion methods that can determine these quantities has been difficult. The method presented in Chapter 4 has several advantages to its formulation, particularly the ability to utilize different frequency bands and phases depending on the earthquake's size and the incorporation of the physical constraint that the source region have non-negative volume which is non-linear in the elements of the 2nd moments. Additionally, since about 1995 the global seismic network has improved to the level where 2nd moments can be routinely determined for large earthquakes. In Chapter 5 we present the first systematic global catalog of 2nd degree moments of large ($M_w > 6.5$) earthquakes.

A point-source representation of an earthquake, such as the 0th and 1st degree moments of $\dot{\mathbf{\Gamma}}(\mathbf{r}, t)$ (i.e. the Centroid Moment Tensor, CMT), results in the well-known fault-plane ambiguity. By determining the 2nd degree moments of an earthquake's moment-release distribution we are able to resolve the fault-plane ambiguity. For simple earthquakes the 2nd spatial moment represents a characteristic rupture volume that is nearly planar and aligned along one of the fault planes of the event's moment tensor, thus specifying the true rupture plane. We are able to systematically resolve the fault-plane ambiguity for the catalog of events in Chapter 5 by calculating the characteristic rupture dimension in the direction normal to each of the two candidate fault-planes for an event, and choosing the one with the smaller value as the true fault-plane.

While the 2nd moments are clearly aligned along one of the nodal planes for most earthquakes, for complex faulting events this isn't always the case. In particular for the Romanche and Prince Edwards Island events, the 2nd spatial moment is oriented at a significant angle from either nodal plane (Chapter 6). The only type of faulting model that can produce the observed 0th, 1st, and 2nd degree moments of the Romanche and Prince Edward's Island events is one that involves slip on multiple sub-parallel transforms. Thus the 2nd-moment space-time inversion that is based primarily on the amplitudes of P-waves and Rayleigh waves confirms the travel-time based observations of complex faulting from Chapters 2 and 3.

The 2nd moments determined for the Prince Edwards Island and Romanche earthquakes in Chapter 6 demonstrate that the slow slip events that occurred during these earthquakes occurred ruptured separate faults from their respective mainshocks. Therefore the slow-precursors were not simply nucleation phases that accelerated into fast dynamic ruptures. To explain the apparently causative relationship between the slow-slip events and the mainshocks in these earthquakes, we calculated the changes in Coulomb failure stress that would have occurred at the location of the Romanche mainshock as a result of the slow-precursor. We find that the fault which failed in the Romanche mainshock was brought significantly closer to failure by the precursor (Chapter 6). A similar mechanism may also be responsible for triggering the off-fault mainshock in the Prince Edward earthquake.

Chapter 2

The 1994 Romanche Transform Earthquake

Published in *Science* by J. J. McGuire, P. F. Ihmlé, an T. H. Jordan, 274, 82-85, 1996. Copyright by the American Association for the Advancement of Science.

Abstract. Low-frequency spectral anomalies have indicated that some large earthquakes are preceded by extended episodes of smooth moment release, but the reality of these slow precursors has been debated because they have not been directly observed in the time domain. High-gain seismograms from the 14 March 1994 Romanche Transform event (M_w 7.0) show a precursory ramp with a moment of 7 x 10^{18} Newton-meters beginning about 100 seconds before the arrival of the high-frequency P waves. This precursor was the initial phase of a slow component of slip that released nearly half of the total moment of the earthquake. Such behavior may be typical for large earthquakes on the oceanic ridge-transform system.

2.1 Introduction

Since the early work of Kanamori and Cipar (1974) on the great 1960 Chilean earthquake, episodes of slow, smooth moment release have been postulated to precede and initiate some large earthquakes. New techniques have recently been developed for the detection and analysis of slow precursors using low-frequency seismic spectra (Jordan, 1991; Ihmlé *et al.*, 1993). Their application to a catalog of large events has revealed that slow precursors are rare in continents and convergence zones but appear to be common features of earthquakes on the oceanic ridge-transform system (Ihmlé and Jordan, 1994). For example, Ihmlé *et al.* (1993) found that the great Macquarie Ridge earthquake of 23 May 1989, which had a moment-magnitude (M_W) of 8.2, was preceded by a slow precursor with a moment release of about 3x10^{20} Newton-meters (N-m), equivalent to a M_w 7.6 event. However, no precursor was evident on high-gain, broadband seismograms in the interval immediately before the high-frequency P-wave arrival times (Ihmlé *et al.*, 1993). This observation has led some to reject the slow-precursor hypothesis (Kedar *et al.*, 1994).

2.2 Time Domain Signals

The detection of slow precursors as time-domain signals at teleseismic distances is difficult because the ambient level of seismic noise rises rapidly at frequencies below about 3 millihertz (mHz) (Agnew and Berger, 1978; Beroza and Jordan, 1990). Here we report the detection of such signals for the 14 March 1994 earthquake on the Romanche transform fault in the central Atlantic ocean (Figure 2.1). This large earthquake (M_w 7.0) comprised at least two ordinary ruptures, a small preshock (event A in Figure 2.2) followed approximately 16 s later by the mainshock (event B). At the lowest noise station, Tamanrasset, Algeria (TAM), a low-passed version of the P wave shows a distinct ramp in front of the mainshock (Figure 2.2). The amplitude of the ramp exceeded the noise level for at least 100 s before the high-frequency (A) arrival time, and there is some suggestion that its beginning may have preceded A by as much as 300 s.

Although TAM shows the precursor most clearly, the signal is visible at all other stations where the first swing of the low-passed, mainshock P wave was greater than a factor of three above the noise level (Figure 2.3). On each of the six records that satisfy this criterion, the mainshock P wave was preceded by a ramp of the same polarity,

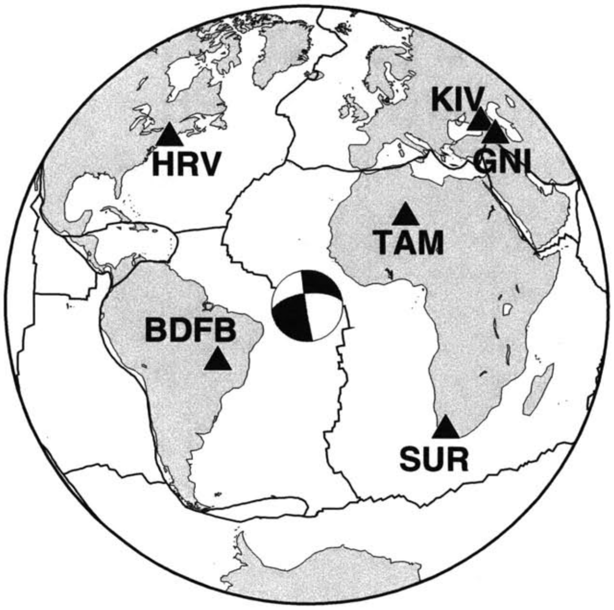

Figure 2-1: Map showing the Harvard Centroid Moment Tensor (CMT) location and mechanism of the 14 March 1994 Romanche Transform earthquake (7). Triangles are the locations of the six seismic stations used in the P-wave stack; these stations sample all four quadrants and lie away from nodes in the radiation pattern.

and in all six the ramp has a consistent relative slope and duration. Because the low-noise stations cover all four quadrants of the focal sphere and sample epicentral distances ranging from 28° to 73°, these observations confirm that the ramp is a source signal with a radiation pattern similar to the mainshock rather than a propagation effect. Given the coherency of the six low-passed records, we stacked them to obtain a composite waveform (lower part of Figure 2.3). When corrected for the group delay of the low-pass filter, the precursory ramp can be seen at least 90 s before the event-A arrival time. As illustrated in Figure 2.3, a similar stack of another strike-slip earthquake yielded no such precursor.

2.3 Directivity

The A and B subevents have an unusual space-time relationship that also suggests precursory moment release. We picked the P-wave times of the two subevents on

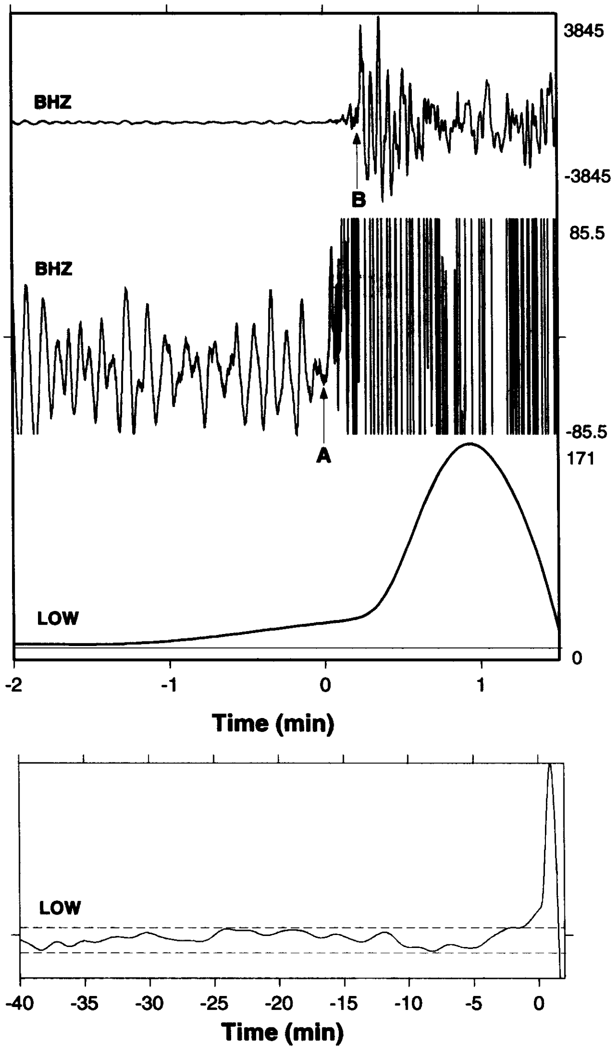

Figure 2-2: Vertical-component records of the P wave from the 1994 Romanche Transform earthquake at the high-performance seismic station TAM. Top panel contains the raw broadband trace at two magnifications (both labeled BHZ) and a detided, low-pass filtered version of the same seismogram (labeled LOW), revealing the precursory ramp beginning at least 1 min before the high-frequency arrival time (t = 0). The low-pass filter is a 4-pole Butterworth with a 6-mHz corner. Vertical scales are digital units of the seismogram (counts). Arrows are the arrival-time picks for subevents A and B, with zero time set to be the high-frequency (event-A) arrival time. A comparison of the lower two traces, which have the same magnification, shows that the amplitude of thehigh-frequency noise is substantially larger than that of the low-frequency precursor, masking the latter on the unfiltered record. The lower panel is the same low-passed record at a longer time scale, with dashed lines approximating noise level. The two low-passed records have not been corrected for the group delay of the filter, which is 10 s.

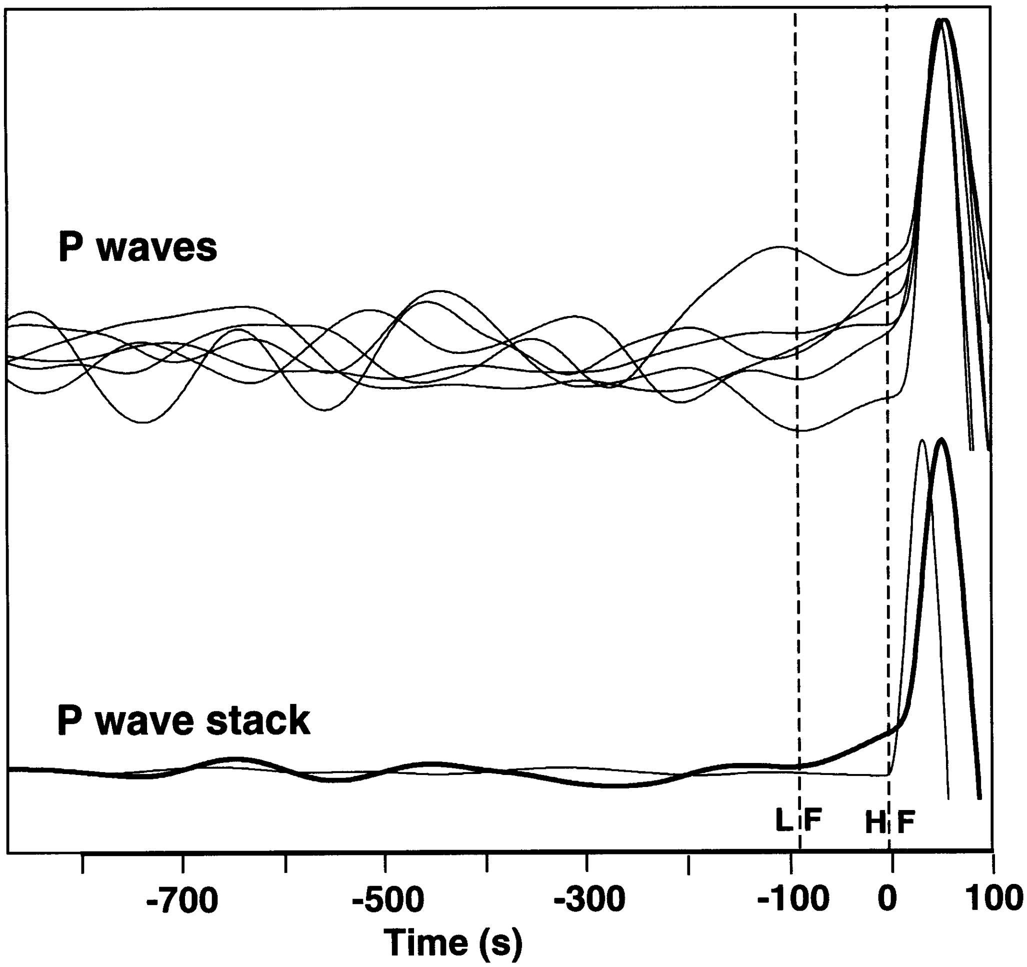

Figure 2-3: Fig. 3. Upper traces are vertical-component P waves for the 1994 Romanche Transform earthquake for the six, low-noise stations shown in Figure 2.1. These were the only stations where the first swing of the main shock P wave was greater than a factor of three above the noise level. All seismograms have been detided, low-pass filtered (4-pole Butterworth with a corner at 6 mHz), corrected for the group delay of the filter, detrended, and corrected for radiation pattern (flipped in polarity if dilatational and normalized to a common amplitude). Lower traces are a stack of these six seismograms (heavy line) and a similar, six-station stack for the large (Mw 7.0) Mendocino earthquake of 01 September 1994 (8) (light line). In both cases, zero time corresponds to the high-frequency arrival time (labelled HF). The Romanche Transform earthquake shows a precursory ramp beginning at or before 90 s (labelled LF), whereas the Mendocino earthquake does not. The delay in the arrival time of the high-amplitude P wave for the Romanche Transform earthquake corresponds approximately to the 16-s delay between event A, which is the first high-frequency arrival, and event B, which is the mainshock.

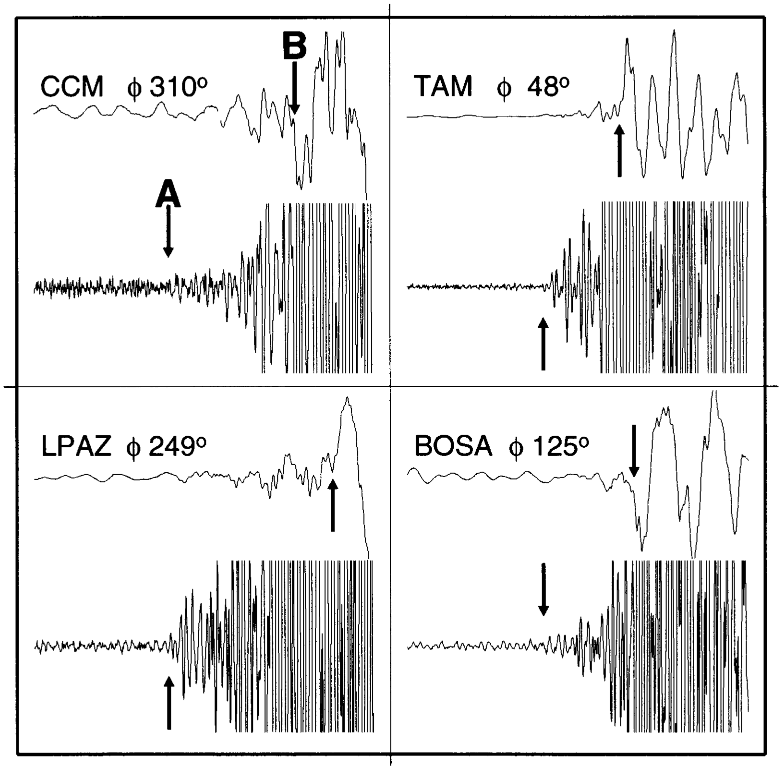

Figure 2-4: Vertical-component, P waves recorded at four stations, showing the arrival-time picks for event A on high-pass filtered seismograms (lower traces) and event B on unfiltered, broadband seismograms (upper traces). Each trace runs from 20 s before to 30 s after the event-A arrival. The high-pass filter is a 4-pole Butterworth with a 1-Hz corner. ϕ is the station azimuth. Stations to the northeast (e.g., TAM) have smaller B-A time differences than stations to the southwest (e.g., LPAZ), indicating that event B is northeast of event A.

Mainshock Delay Times

Station	Azimuth	Delta	B-A Time, s
ECH	25	56	12.4
SSB	25	53	11.3
TAM	48	37	10.8
LBTB	121	53	18.4
BOSA	125	54	14.5
BDFB	238	28	21.7
LPAZ	249	46	24.1
SJG	297	46	18.8
ANMO	305	85	14.5
CCM	310	73	16.8

Table 2.1:

all records with clear arrivals (Figure 2.4, Table 2.1), located them relative to the background seismicity using the clustered event algorithm of Jordan and Sverdrup (1981) which yields relative locations that are independent of common path anomalies. We relocated subevents A and B together with all events in the region having 30 or more P-wave arrival times in the International Seismological Centre catalog from 1964 to 1996. All event depths were fixed at 10 km. We then shifted the hypocentroid of the seismicity cluster 12 km in the direction N30°E to align the seismicity with the Africa-South America plate boundary on a high-resolution map of the altimetric gravity field (Figure 2.5). We found that the two subevents were separated by 83 ± 15 km and 16.7 ± 1.0 s. Therefore, a model of the rupture initiating at A and propagating directly to B requires a rupture velocity of 5.0 ± 1.0 km/s, which exceeds the shear-wave speed in the upper oceanic lithosphere and thus the typical rupture velocity of shallow-focus earthquakes (Scholz, 1990). Moreover, the A and B locations lie along an azimuth of N37 ± 8°E, which is at a significant angle to the strikes of the inferred fault planes for both subevents (Figure 2.5).

We determined the moment tensor in 1-mHz bands from 1 to 11 mHz, using the free-oscillation inversion method described by Riedesel *et al.* (1986); no significant frequency dependence of the source mechanism was observed, which implies that the

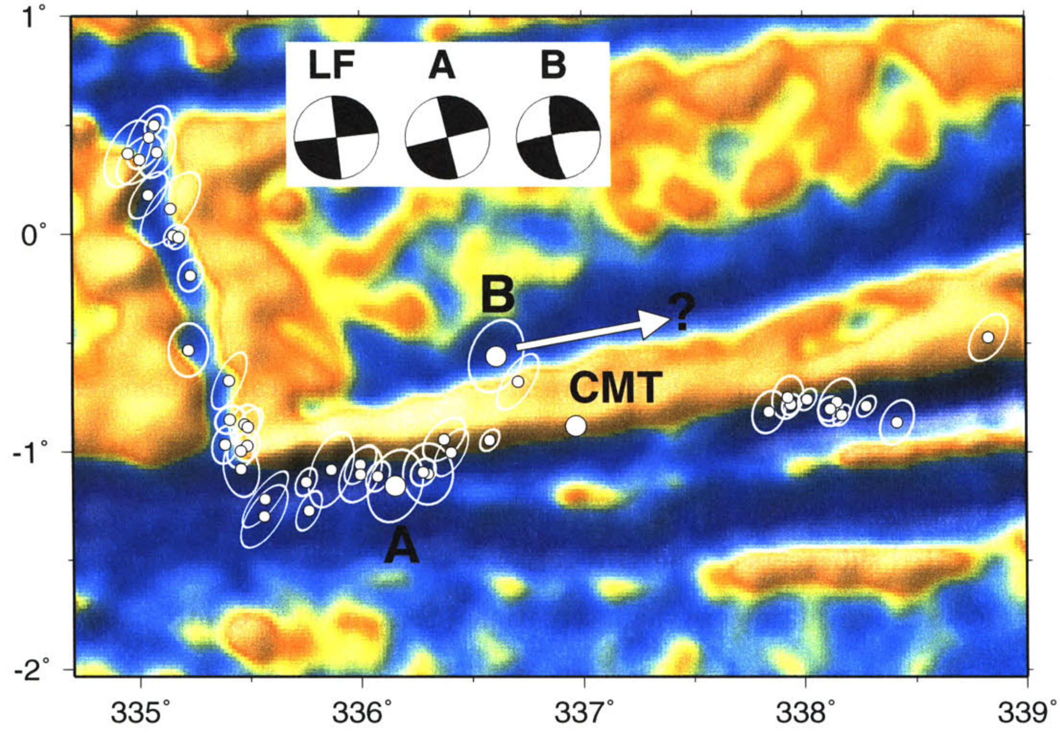

Figure 2-5: Map of the western part of the Romanche transform fault, showing the relocated earthquakes, plotted as points with 95% confidence ellipses (10), and the altimetric gravity field, plotted in color (Sandwell, 1995). Beachball insets are the low-frequency source mechanism (LF) and subevent mechanisms (A and B) for the 1994 Romanche Transform earthquake. Large dots are the epicenters of the A and B subevents and the Harvard CMT epicentroid, and the arrow emanating from B shows the direction and approximate length of the main rupture. The gravity anomalies range from -15 milligals (blue) to +15 milligals (red), and the relief is illuminated from the northwest.

slow component of the 1994 Romanche Transform earthquake had a radiation pattern similar to that of the main shock. The mechanism labeled LF in Figure 2.5 is the average across the frequency band 3 to 6 mHz. The source mechanisms of subevents A and B, also shown in Figure 2.5, were determined by waveform analysis. They are similar but not identical; for example, their long-period P-wave polarities are reversed at Nana, Peru (NNA). Thus all the subevents of the 1994 sequence ruptured on nearly E-W striking fault planes which is incompatible with the directivity observed between subevents A and B. These data suggest that the two events occurred on separate fault planes and were initiated by a common precursor.

The morphology of the western portion of the Romanche Transform is extremely complex, exhibiting multiple paleotransform valleys that resulted from past changes in plate motions (Bonatti *et al.*, 1994). The location of event A, the small preshock (M_w 6), is consistent with it being on the primary active trace of the Romanche transform fault, but event B, the mainshock, is located significantly north of this feature, in a fault valley with a trend nearly parallel to the main transform fault. The directivity inferred from the azimuthal variation of the P waveforms indicates that the mainshock propagated to the east. No aftershocks were teleseismically recorded, so we could not determine its rupture length, but standard scaling relations would imply that it was 50 to 70 km (Scholz, 1990). This approximates the length of a seismic gap just south of the mainshock, where the valley of the main fault trace is interupted by a large bathymetric high (Searle *et al.*, 1994) (Figure 2.5).

It is not possible to locate the slow precursor relative to the mainshock, but moment-tensor inversions exclude the possibility that the precursor occurred on a fault connecting the A and B events. One scenario consistent with the available data (among many) is that smooth slip at depth in the normally aseismic region redistributed stress in the region and triggered seismicity in both the westernmost portion of the Romanche (A event) and the neighboring fault valley to the north of the seismic gap (B event).

2.4 Source Time Function Estimation

We also investigated the 1994 Romanche Transform earthquake using the spectral synthesis and inversion methods applied in previous studies of slow earthquakes (Jordan, 1991; Ihmlé *et al.*, 1993; Ihmlé and Jordan, 1994). We estimated the amplitude (total-moment) spectrum $M_T(\omega)$ and phase delay (time-shift) spectrum $\delta t(\omega)$ of the source at 1-mHz intervals from 1 to 50 mHz using a combination of body waves, surface waves, and free oscillations. The source spectra shown in Figure 2.6 were obtained using the Harvard CMT (Dziewonski *et al.*, 1994) and the PREM velocity and attenuation structure (Dziewonski and Anderson, 1981) corrected for the 3-D elastic structure of Su *et al.* (1994). The fundamental modes above 7 mHz were also corrected for smaller scale heterogeneity using the degree-36 phase velocity maps of Ekström *et al.* (1993). The different wave types yielded consistent results throughout their regions of overlap. The phase-delay spectrum is nearly constant across the entire frequency band, but the amplitude spectrum shows a sharp break at about 10 mHz. This pattern is similar to that observed for other slow earthquakes by Jordan (1991) and Ihmlé and Jordan (1994) which they interpreted as compound sources. According to this hypothesis, the amplitude break results from the superposition of an ordinary fast rupture, which dominates the spectrum at high frequencies, and a smooth transient of longer duration, which dominates at low frequencies. The lack of a corresponding break in the phase-delay spectrum requires that the centroid times of the two events are nearly equal, thus implying that the slower event begins first. The break in the amplitude spectrum is also visible in measurements of the source spectra made on transverse component records (Figure 2.7). The roll-off in the amplitude spectra for the transverse component is nearly identical to that observed for the vertical component, but is somewhat less well-constrained due to the higher-noise levels on ths component.

To quantify these statements, we performed a joint inversion of the spectra and the P-wave stack for the source time function (Figure 2.6). The results show an event sequence that comprises a slow earthquake beginning 110 s before the high-frequency

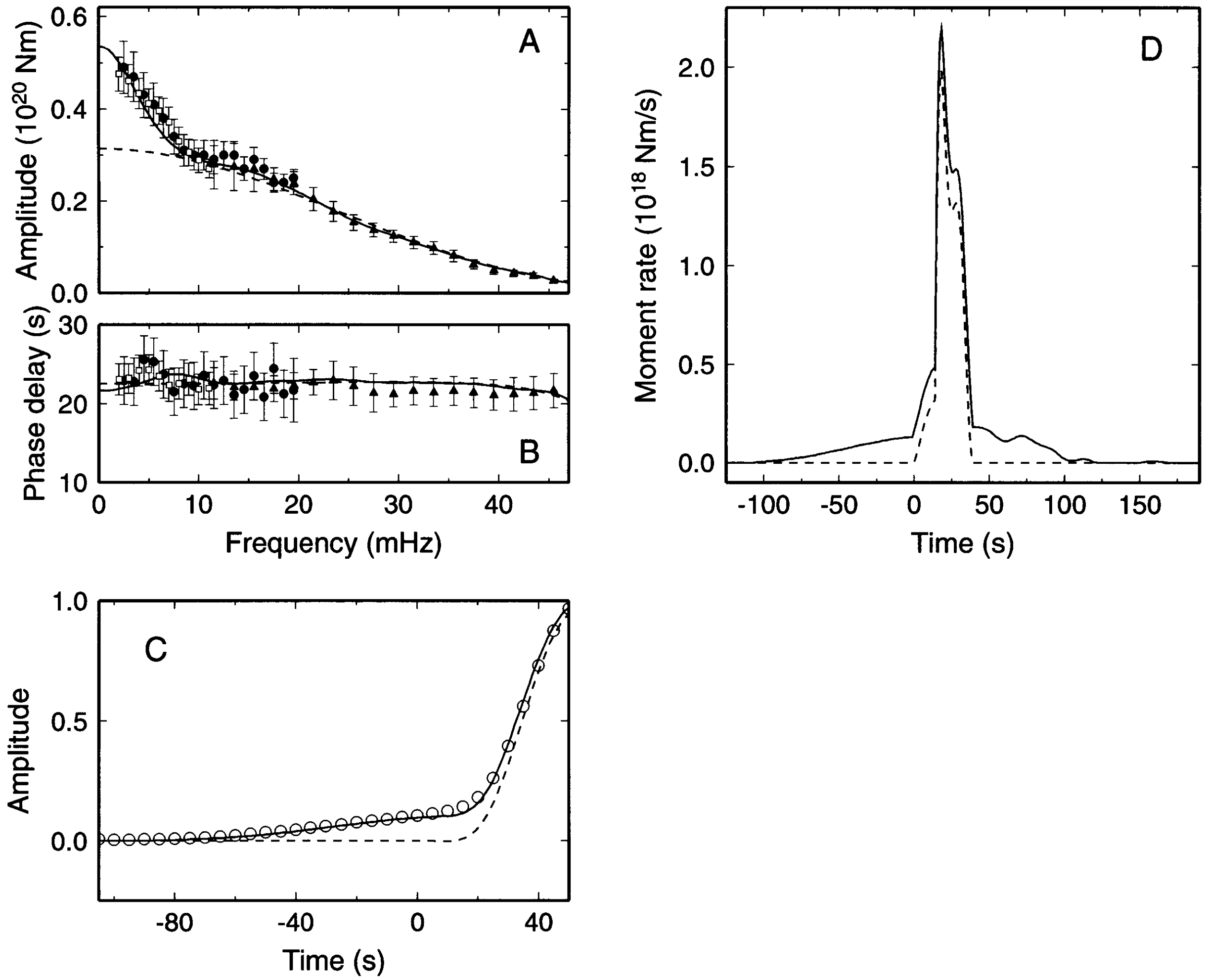

Figure 2-6: (A) Amplitude and (B) phase-delay spectra for the 1994 Romanche Transform earthquake. Points are estimates with one-sigma error bars obtained from propagation-corrected spectra, averaged over a global network of 32 broadband stations (16); wave types used in the measurements are spheroidal free oscillations (solid circles), Rayleigh waves (open squares), and long-period body wavetrains (solid triangles). Solid and dashed lines are the spectra obtained by Fourier transforming the source time functions in panel D. The phase-delay spectrum is referenced to the NEIC high-frequency origin time (7), which corresponds to the initiation of event A. (C) Comparison of the observed P-wave stack from Figure 2.3 (open circles) with synthetic seismograms (solid and dashed lines) computed from the source time functions in panel D. (D) Solid line is the source time function obtained by the joint inversion of the spectral-domain data in panels A and B and time-domain data in panel C. Dashed line is from the inversion of just the spectral data in the 10-50 mHz band, where the time function was restricted to be zero for time less than 0 s and greater than 45 s.

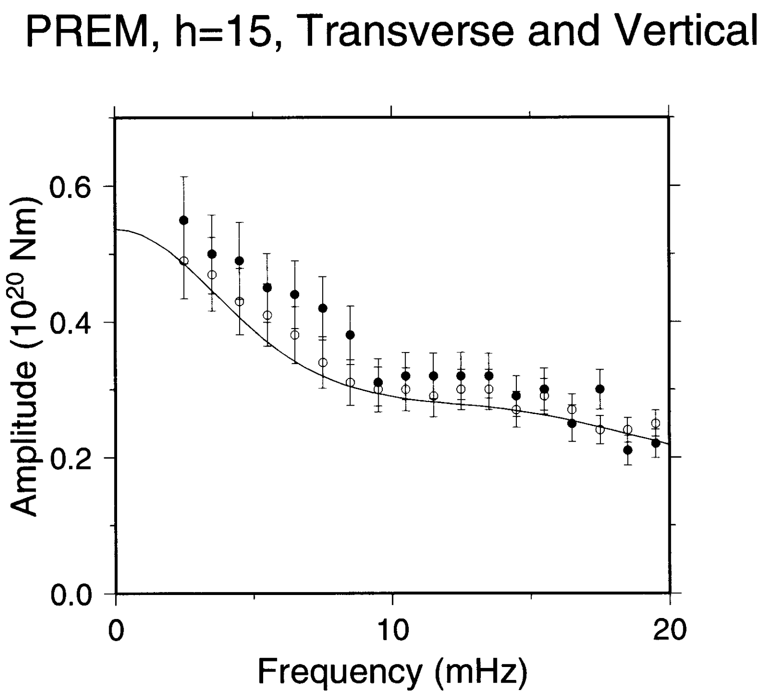

Figure 2-7: Comparison of the amplitude spectra for the 1994 Romanche event derived from the transverse (solid circles) and vertical (open circles) component data. Both types of measurements were made with the technique of Silver and Jordan (1982) using synthetic seismograms calculated for the Harvard CMT and PREM velocity structure. The solid line shows the fit to the amplitude spectra for the source-time function in Figure 2.6d

origin time (t = 0) and continuing for about 250 s, a preshock initiating at 0 s, and a 29-s pulse of high moment release beginning at 16 s. This compound-event model fits the amplitude and phase-delay data across the entire frequency range, as well as the precursor observed in the waveform stack. We also inverted the spectral data alone, allowing no moment release at $t \leq 0$, but found that we could not simultaneously satisfy the large amplitudes and flat phase-delays at low frequencies. Hence, the spectral data confirm the existence of the slow precursor seen in the P-wave stack.

The best-fitting source time function has a total static (zero-frequency) moment of 5.4 $\times 10^{19}$ N-m. Comparing its amplitude spectrum to one from a source time function confined to the interval $0 \leq t \leq 40$ s (Figure 2.6) indicates that the static moment released by the slow component is about 2.3 x 10^{19} Nm, or 43% of the total. About 0.7 x 10^{19} Nm (13%) is released in the slow precursor.

The amplitude spectrum shown in Figure 2.6 is dependant on the centroid-location, moment-tensor, and earth-structure which are assumed in the calculation of the mode-sum synthetics utilized by the various spectral estimation techniques. It has been suggested by Abercrombie and Ekstrom (1999) that the roll-off in the amplitude spectrum at low-frequencies ($\leq$ 10 mHz) is due to the use of the PREM earth-model and CMT centroid depth (15 km) in the synthetic seismogram calculation. To check the dependance on elastic-structure, we calculated estimates of the amplitude spectrum using the oceanic velocity model PA5 Gaherty *et al.* (1996) which has a 5 km thick water-layer and a crustal thickness of 7 km (these layers are 3 and 21.4 km thick respectively in PREM) combined with the PREM Q-model. We used the same latitude, longitude, and centroid time as in Figure 2.6, but the centroid depth was shifted from 15 to 18 km to agree with the depth determined by Abercrombie and Ekstrom (1999) from body-wave fitting. We preformed moment-tensor inversions using the free-oscillation technique of Riedesel *et al.* (1986) and used the resulting values (M_{rr} = -.28 , $M_{\theta\theta}$= 1.0, $M_{\phi\phi}$= -.73, $M_{r\theta}$= -1.4 , $M_{r\phi}$= -.62, $M_{\theta\phi}$= -4.1, x10^{19} Nm) to calculate the synthetics used in the amplitude spectrum estimation procedures. The amplitude spectrum for this oceanic model is shown in Figure 2.8 (note the phase-delay spectrum in Figure 2.8 is the same as the one in Figure 2.6). While the roll-off in the amplitude spectrum is slightly less pronounced than in the PREM amplitude spectrum, the compound nature of the Romanche event remains very clear. Inverting this amplitude spectrum along with the P-wave stack and phase-delay spectrum from Figure 2.6 yields the source-time function shown in Figure 2.8D. This source-time function shows an event sequence that comprises a slow earthquake beginning 100 s before the high-frequency origin time ($t = 0$) and continuing for about 250 s, a preshock initiating at 0 s, and a 15-s pulse of high moment release beginning at 15 s. While the precursor for this model has slightly less seismic-moment than for the PREM velocity model (Figure 2.6), it still fits the precursory ramp seen in the P-

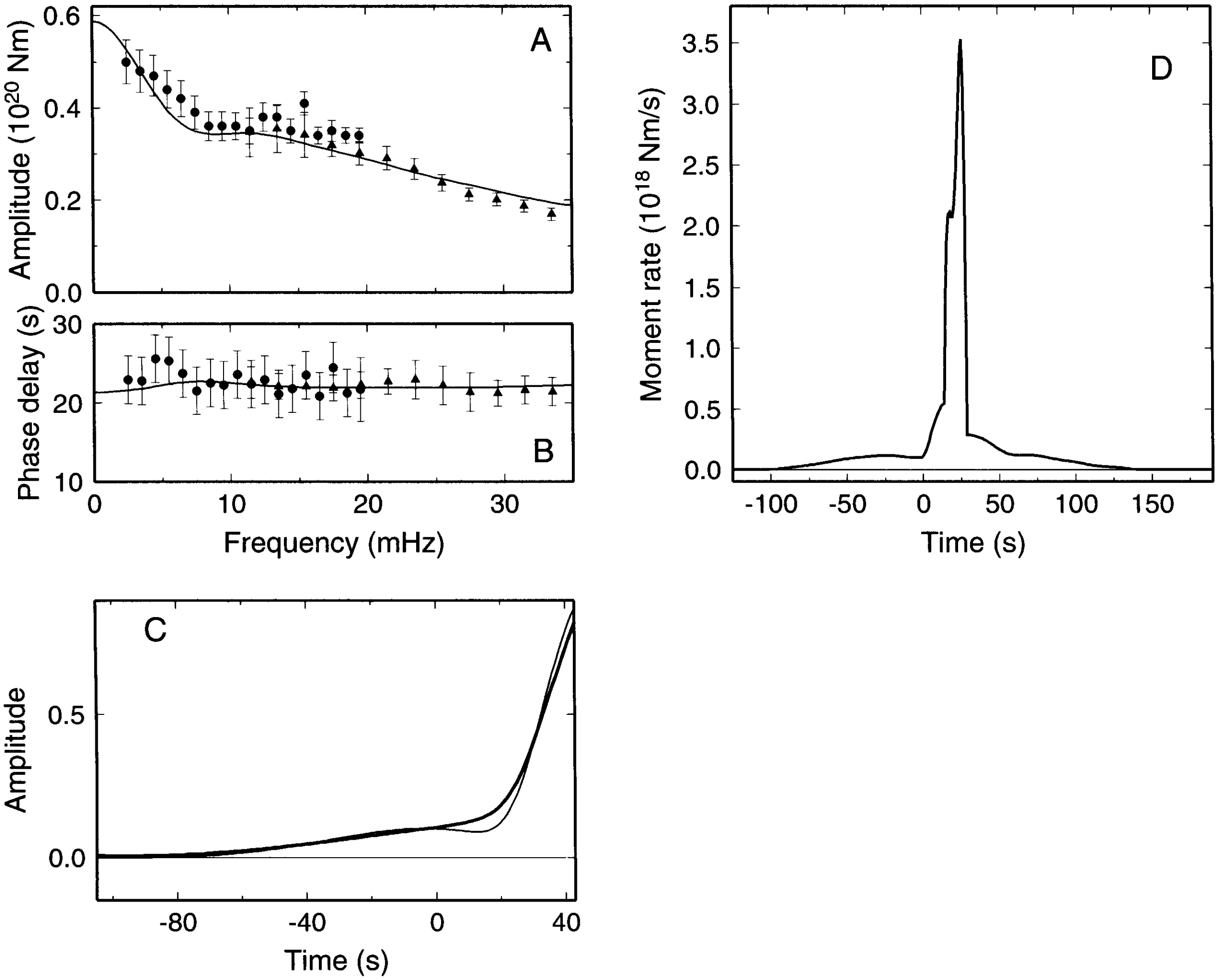

Figure 2-8: (A) Amplitude and (B) phase-delay spectra for the 1994 Romanche Transform earthquake determined using the oceanic velocity structure PA5. Points are estimates with one-sigma error bars obtained from propagation-corrected spectra, averaged over a global network of 32 broadband stations (16); wave types used in the measurements are spheroidal free oscillations (solid circles), Rayleigh waves (open squares), and long-period body wavetrains (solid triangles). Solid lines are the spectra obtained by Fourier transforming the source time function in panel D. The phase-delay spectrum is referenced to the NEIC high-frequency origin time, which corresponds to the initiation of event A. (C) Comparison of the observed P-wave stack from Figure 2.3 (thick line) with a synthetic seismogram (thin line) computed from the source time function in panel D. (D) Solid line is the source time function obtained by the joint inversion of the spectral-domain data in panels A and B and time-domain data in panel C.

waves. Thus the measurements for an oceanic-velocity model also support the P-wave observations of a slow-precursor for the Romanche event.

2.5 Discussion

Since slow earthquakes occur most frequently along oceanic transform faults, Ihmlé and Jordan (1994) proposed that the intrinsic stratification of oceanic lithosphere may be responsible for their compound-event character. According to this hypothesis, fast ruptures in the shallow seismogenic zone are initiated by the loading due to slower episodes of slip in the subjacent, serpentinized upper mantle. The superposition of a fast event in the middle of a slow event, as seen in the source time function of Figure 2.6, is most easily explained by this depth relationship.

The data presented here indicate that the slow precursor of the Romanche earthquake grew for at least 100 s before it triggered a fast rupture, and the total moment released during the entire slow event was comparable to that of the mainshock. This behavior appears to be common on oceanic transform faults, but it is in marked constrast to the nucleation phases observed for other earthquakes, which are small and accelerate quickly into inertia-dominated instabilities (Ellsworth and Beroza, 1995). The shape of the waveform stack and the absence of any observable high-frequency energy prior to event A indicate that the precursor's moment rate increased smoothly at a nearly linear rate due to values of $\ddot{M}$ which were 2-3 orders of magnitude smaller than those during the mainshock. This implies that the product of the rupture and particle velocities during slow phase of slippage must be at least two orders of magnitude smaller than that during the mainshock (see Chapter 1). Hence, the designation "slow precursor" is truly warranted.

Chapter 3

Further Evidence for the Compound Nature of Slow Earthquakes: The Prince Edward Island Earthquake of April 28, 1997

Published in *Journal of Geophysical Research* by J. J. McGuire and T. H. Jordan, 105, 7819-7828, 2000.

Abstract. Seismograms of the April 28, 1997, Prince Edward island transform fault earthquake (M_w 6.8) show clear evidence for the superposition of two types of rupture, a normal earthquake and a slow component which primarily radiated energy at low frequencies. We combined low-frequency spectral data with P waveform data to invert for a source time function that satisfied data from 0.001 to 2.5 Hz. The results show that the earthquake started with a slow event which began ~15 s before the fast mainshock and was part of a slow earthquake which lasted over 30 s. The smoothness of the initial event is inferred from the low amplitude of high-frequency energy at

regional stations during the initial portion of the P wave arrival. Directivity analysis shows that the two components of the rupture occurred on different faults. The slow event occurred on the main transform, and the fast event occurred on a parallel fault 40 km to the east. A similar compound sequence, involving both slow and fast components and rupture on multiple faults, occurred on the Romanche transform in 1994. These and other results for slow earthquakes suggest that many large events on oceanic transform faults are compound events.

3.1 Introduction

Fault slip events are classified as slow earthquakes when the ratio of low-frequency to high-frequency radiated energy is anomalously large. This classification has been applied to events with durations raging from ~1 s (Kanamori and Hauksson, 1992) to 10^6 s (Linde *et al.*, 1996). Slow earthquakes are particularly common on oceanic transform faults (Okal and Stewart, 1982) and may represent the majority of earthquakes on such faults (Ihmlé and Jordan, 1994). The preferential radiation of low-frequency energy results from a smoother than normal moment rate function, which is generally ascribed to the event having a low rupture velocity v_r and/or particle slip velocity $\Delta\dot{u}$. For instance, for a unilateral (Haskell) rupture on a rectangular fault with constant $\Delta\dot{u}$, the moment rate will initially increase at a rate $\ddot{M} = 2\mu W v_r \Delta\dot{u}$, where W is the fault width and μ is the shear modulus. Thus an earthquake with low rupture and particle slip velocities will produce a slower initial rise in the moment rate function, $\dot{M}(t)$.

Recently, Jordan (1991) and Ihmlé and Jordan (1994) proposed that slow events represent the superposition of a ordinary, fast earthquake, which dominates the source spectrum at high frequencies, and a smooth transient of longer duration, which dominates at low frequencies. This compound event model has been based primarily on breaks in the source amplitude spectrum measured from low-frequency surface waves and normal-mode excitations (Ihmlé and Jordan, 1994) rather than on clear body waveform data. For instance, the M_w 7.0 1994 Romanche transform event showed a break in its source amplitude spectrum at ~7-8 mHz below which the amplitude increased rapidly (McGuire *et al.*, 1996). This type of spectral break implies the superposition of a normal earthquake with an event of much longer duration which primarily radiated energy below 7 mHz. The best fitting moment rate function for the Romanche event included both a 200-s-long slow earthquake and a 20-s-long mainshock. In addition, the spatial relationship between the two modes of rupture has been difficult to determine. The two high-frequency subevents of the Romanche earthquake occurred on separate, parallel faults. However, the signal to noise ratio of the teleseismic *P*-waves was too poor below 7 mHz to determine which fault was ruptured by the slow component. In contrast, the compound nature and the relative location of the two modes of rupture are much more obvious for the 1997 Prince Edwards Island earthquake.

3.1.1 April 28, 1997, Event

The April 28, 1997, oceanic transform fault slow earthquake (m_b 5.7, M_w 6.8) occurred near Prince Edward Island (Figure 3.1) on the northernmost section of the Discovery II transform fault (Fisher and Sclater, 1983), and it was recorded by a network of temporary broadband seismometers in southern Africa (James *et al.*, 1998). These high-quality, nearby records show clear evidence of a compound source process involving both a normal earthquake and an event which preferentially radiated energy at low frequencies. At high frequencies (>1 Hz) the *P* wave recordings at the southern African stations began with a low-amplitude arrival which lasted ~10-15 s and was approximately the amplitude of the arrival observed for a m_b 4.4 aftershock (Figure 3.2). However, when viewed at lower frequencies (< 60 mHz), the initial arrival has an amplitude that requires significant moment release before the arrival of the mainshock *P* wave. The low-frequency ramp can also be seen at teleseismic stations such as KMBO and TAM (Figure 3.3). Low-pass-filtered version of the *P* waveforms from a nearby event which occurred on May 21, 1998 (M_w 6.3, located 150 km to the southwest), are also shown in Figures 3.2 and 3.3 for comparison. The initial low-frequency arrival is not present in either regional or teleseismic recordings

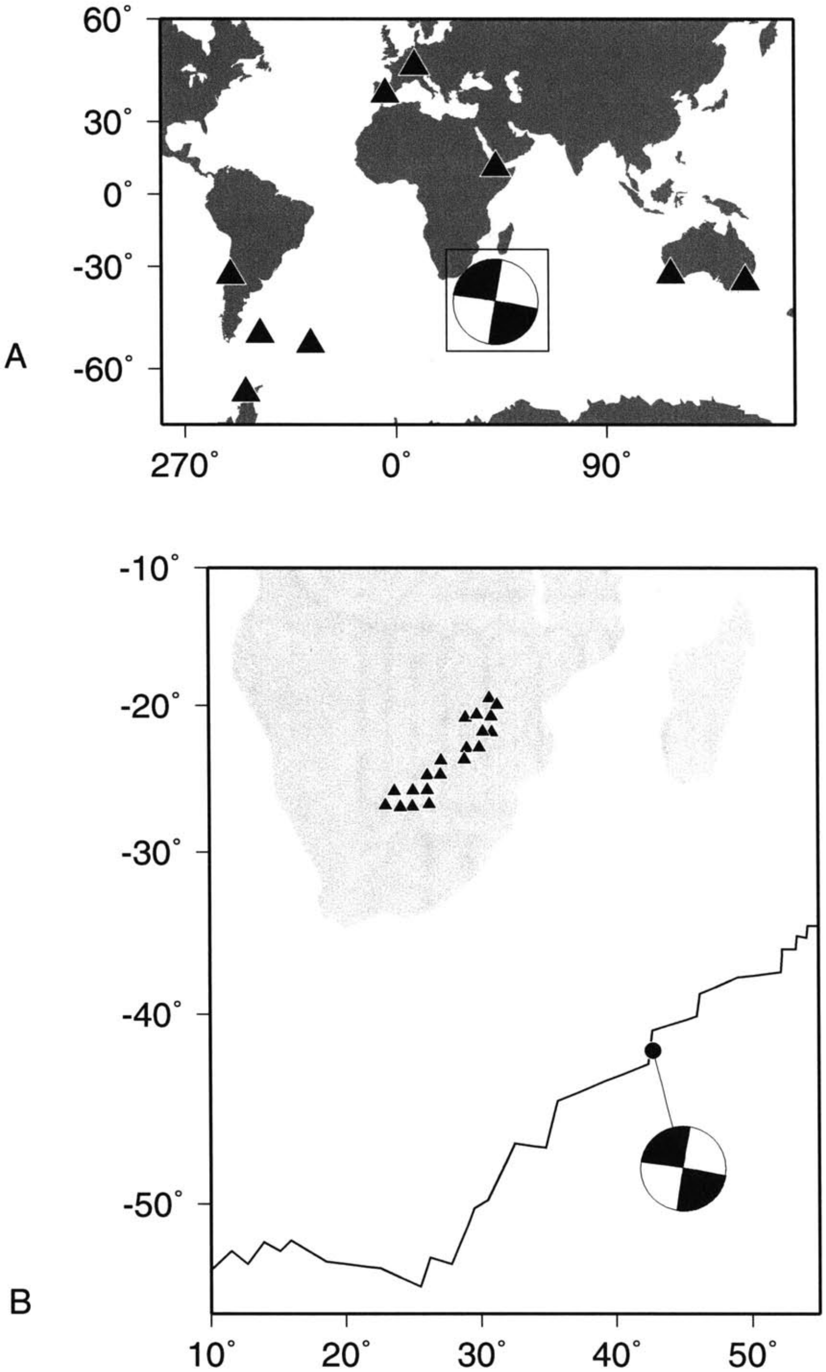

Figure 3-1: (a) Map showing the location and focal mechanism of the April 28, 1997, Prince Edward Island earthquake. Large solid triangles show the locations of teleseismic stations used in our directivity analysis. Solid lines show the location of plate boundaries. (b) Enlargement of the boxed region in Figure 3.1a. Small triangles show the locations of temporary stations in southern Africa used in determining the relative locations of the slow event and its aftershocks. The square shows the location of the 1997 event.

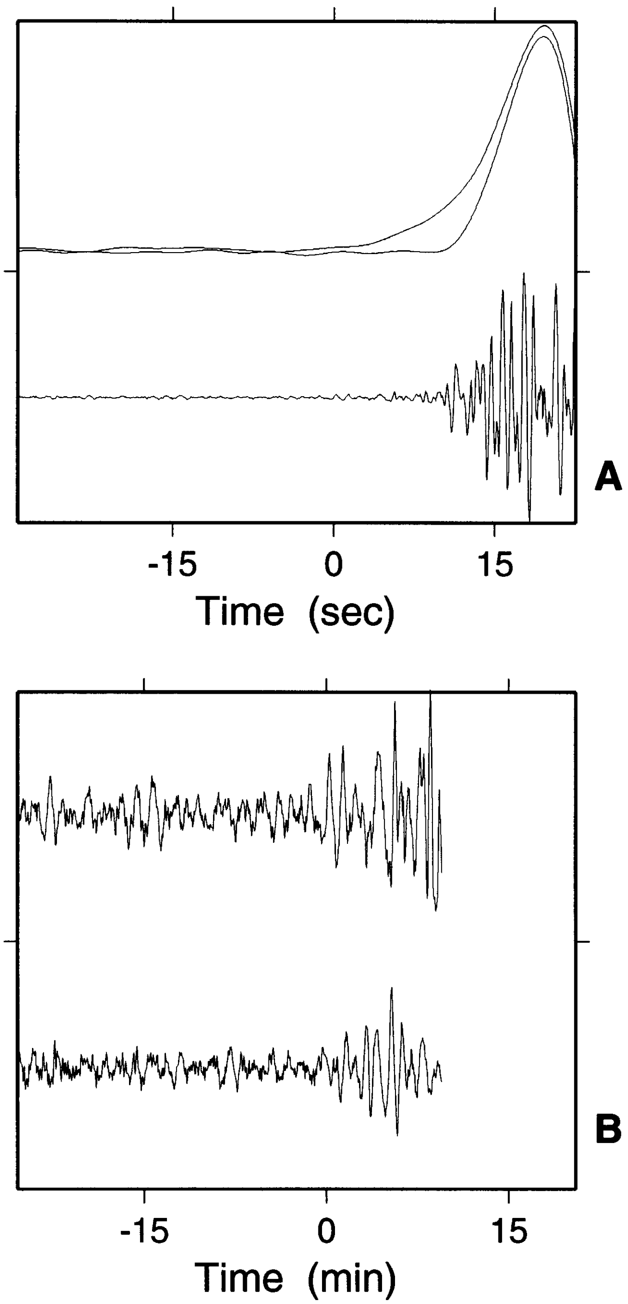

Figure 3-2: (a) (top) Low-passed and (bottom) high-passed vertical component recordings of the *P* wave arrival at station SA18 (-28.63°N 24.3056°E, $\Delta = 20°, \Phi = 306°$). The amplitude during the initial 10-15 s of the arrival appears much larger in the low-frequency version. The *P* wave arrival from the May 1998 event is also shown with the same low-pass filter to emphasize the low-frequency ramp in the 1997 event. (b) (top) The April 28 *P* wave recording (i.e. the high-passed seismogram from Figure 3.2a) and (bottom) the high-passed *P* wave arrival from a m_b 4.4 aftershock on April 29, 1997, shown at the same amplification. Zero time is the high-frequency arrival time in both Figures 3.2a and 3.2b for the April 28 event (12 12:02.9 GMT) and the April 29 event (10 29:33.2 GMT).

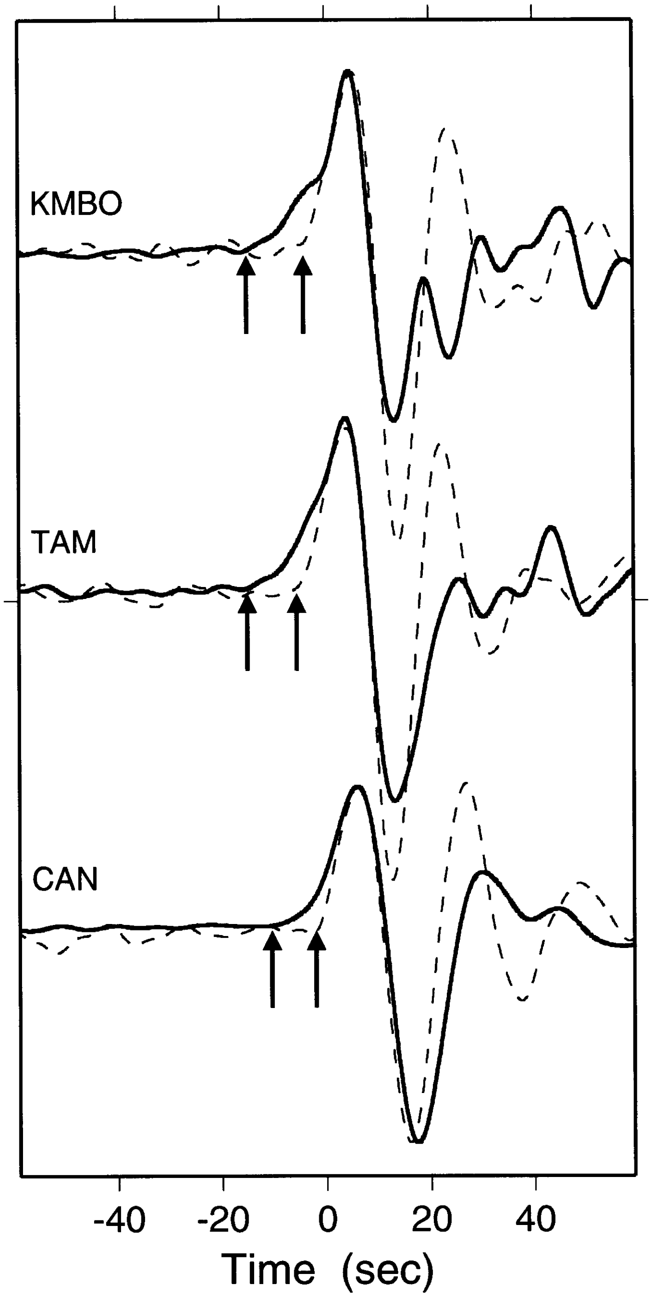

Figure 3-3: Teleseismic P waves at stations KMBO($\Delta = 41°, \Phi = 351°$), TAM ($\Delta = 73°, \Phi = 325°$), and CAN ($\Delta = 78°, \Phi = 127°$). The traces have been low-pass-filtered using a four pole (six pole for CAN due to higher noise level) Butterworth filter with a corner at 50 mHz. The solid traces show the recordings for the April 28, 1997, event, and the dashed traces show the recordings for the May 21, 1998, event. Zero on the time axis corresponds to the P wave arrival time expected from the Harvard CMT location. Arrows show the actual P-wave arrival times (for KMBO 1997, day 118, 12 15:17.50 GMT and 1998, day 141, 22 39:19.7 GMT, for TAM 1997, day 118, 12 19:04.35 GMT and 1998, day 141, 22 43:00.8 GMT and for CAN 1997, day 118, 12 19:33.95 and 1998, day 141, 22 43:24.9).

from the 1998 event. At low frequencies, P waves from these two events should have experienced nearly identical propagation effects. The complete lack of the initial low frequency ramp in the P waves from the 1998 event demonstrates that this unusual signal must have been produced by the source characteristics of the 1997 event rather than by any propagation effect. Thus the 1997 event appears to have begun with a 10-15 s long episode of moment release which predominately radiated energy at low frequencies.

3.2 Source Time Function Estimation

To quantify this observation of a slow beginning to the 1997 Prince Edwards Island earthquake, we inverted for a source time function (STF) that is consistent with both the high- and low-frequency character of the event.

3.2.1 Source Spectrum Measurements

We obtained estimates, shown in Figure 3.4, of the amplitude (total moment) $M_T(\omega)$ and phase delay (time shift) spectrum $\delta t(\omega)$ of the 1997 event at 1-mHz intervals from 1 to 50 mHz. All estimates were obtained using vertical component recordings from global stations and synthetic seismograms computed by mode summation from PREM (Dziewonski and Anderson, 1981), corrected for three-dimensional elastic structure using the degree 12 aspherical model of Su *et al.* (1994) and the asymptotic approximations of Woodhouse and Dziewonski (1984). We also corrected fundamental modes above 7 mHz for smaller-scale heterogeneity using the degree 36 phase velocity maps of Ekström *et al.* (1993). The Harvard centroid moment tensor (CMT) was used, although the depth was shifted from 15 to 25 km (i.e., below the PREM M discontinuity) to produce better overlap between the various spectral estimates. Estimates determined from spheroidal free oscillations (solid circles in Figure 3.4) were calculated using the methods of Silver and Jordan (1982) and Riedesel and Jordan (1989). We also obtained estimates of the source spectrum using the phase coherent method of Ihmlé *et al.* (1993). We used this method to determine $M_T(\omega)$ and $\delta t(\omega)$

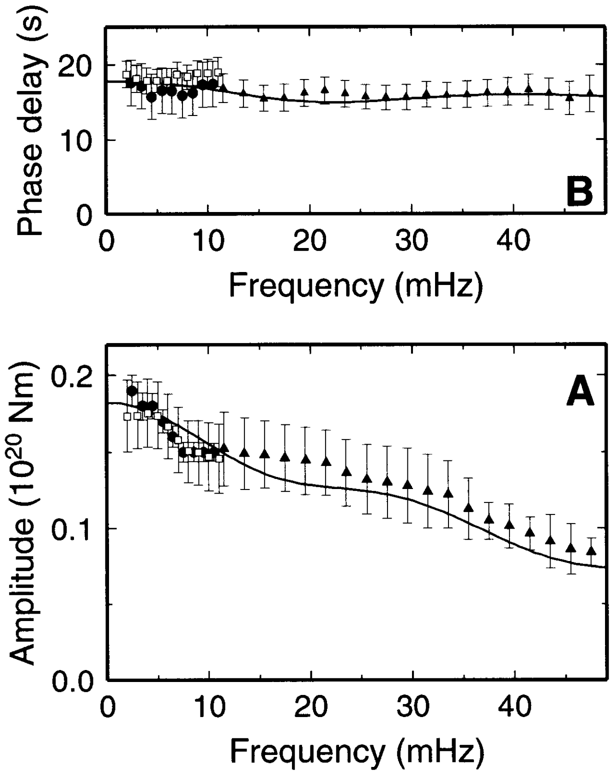

Figure 3-4: The (a) amplitude and (b) phase-delay spectra are estimates with 1σ error bars obtained from propagation-corrected vertical component spectra, averaged over a global network of 52 stations; wave types used in the measurements are spheroidal free oscillations (solid circles), first orbit Rayleigh waves (open squares), and long-period body waves (solid triangles). The solid lines show the spectra obtained by Fourier transforming the source time function in Figure 3.6. Zero time in Figure 3.4b is our determination for the high-frequency origin time (12 07:29.2 GMT).

for both first orbit Rayleigh waves (1-11 mHz) and long-period body wave trains (10-50 mHz). For each wave group a complete mode-sum synthetic was windowed around the arrival to create a isolation filter. The isolation filters were then cross-correlated with both the synthetic and data seismograms, producing two broad-band cross correlagrams for each phase/station pair. The cross correlagrams were windowed in the time domain, and a series of narrow-band Gaussian filters were applied to them at 1-mHz intervals. The lag time between the peaks of the two filtered cross correlagrams was used as the estimate of the differential phase delay, which was then averaged over all of the stations to determine $\delta t(\omega)$. The differential amplitude between observed seismograms and synthetics was obtained from the ratio of the narrow-band cross-correlogram peak amplitudes. $M_T(\omega)$ was estimated by multiplying the median of the differential amplitudes from all the stations by the scalar moment. These approximations are valid for an appropriate choice of windows and filters which are discussed by Ihmlé (1994). The amplitude estimates for the 1997 event show a roll-off with frequency that is diagnostic of a slow event, while the phase delay spectrum is relatively flat (Figure 3.4).

3.2.2 Inversion for the Source Time Function

We jointly inverted the spectral estimates with a low-passed version of the P wave from station KMBO ($\Delta = 41°, \Phi = 351°$), shown in Figure 3.5a, using an algorithm similar to that of Ihmlé and Jordan (1995). To ensure that the resulting STF was consistent with the regional high-frequency arrivals, we added a linear inequality constraint (Lawson and Hanson, 1974) that required that the convolution of the STF with an empirical Green's function (EGF) be smaller than an envelope function derived from one of the South African recordings (SA57) (see Figure 3.5b). Although the aftershock used for the EGF was too small to determine its focal mechanism, we can reasonably assume that it has approximately the same focal mechanism as the initial portion of the mainshock because the events were located near each other on the main transform fault. The stations KMBO and SA57 are both located to the NNE of the event, so differential effects of directivity should be small. However, owing to directivity (see section 4), stations at this azimuth show the longest durations for the initial portion of the slow event, so we slightly overestimated the time between the initiation of the slow component and the mainshock by ~2 s. We also constrained the STF to be nonnegative.

Figure 3.6 shows the STF resulting from our inversion procedure. The event began with a slow event which ruptured for ~12 s before the start of the fast event(mainshock) which lasted ~5 s. The smooth moment release continued after the end of the mainshock for about another 15 s. This STF fits both the spectral

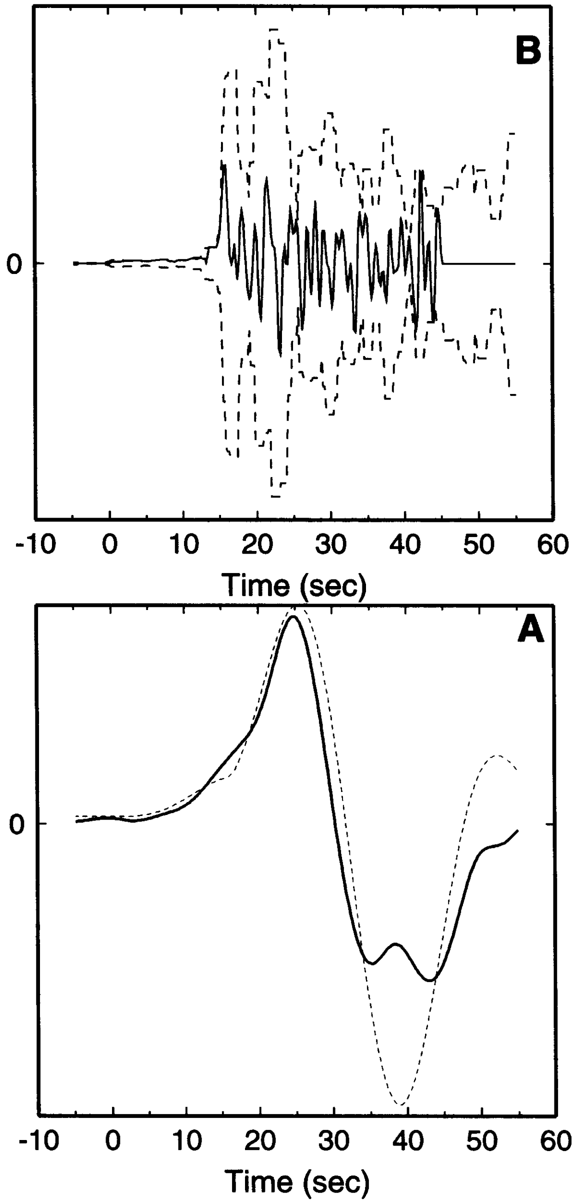

Figure 3-5: (a) A low-passed version (four pole butterworth, corner at 40 mHz) of the P wave at station KMBO (solid line), and the synthetic (dashed line) produced by convolving the source time function in Figure 3.6 with a Green's function calculated by normal mode summation. (b) The envelope function derived from a high-passed version (corner 1.5 Hz) of the P wave recording at station SA57 (dashed line), and the synthetic (sold line) resulting from the convolution of the source time function in Figure 3.6 with an empirical Green's function derived from an aftershock recording (see Figure 3.2b). Zero time in Figures 3.5a and 3.5b corresponds to the high-frequency arrival times at stations KMBO (12 15:13.2 GMT) and SA57 (12 12:17.4 GMT), respectively.

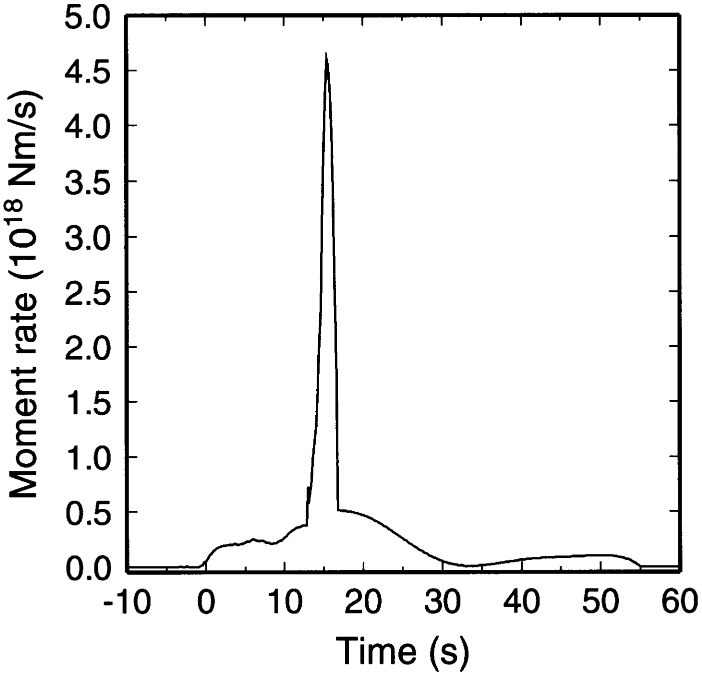

Figure 3-6: The source time function obtained by joint inversion of the spectral data (Figure 3.4) with the P waveform from station KMBO (Figure 3.5a) subject to the high-frequency constraint from the local network (E) (Figure 3.5b). Zero time is our determination for the high-frequency origin time (12 07:29.2 GMT).

data and the low-frequency waveform data while satisfying the high-frequency constraint from the local stations (fits are shown in Figures 3.4 and 3.5). There is a tension in the inversion between fitting the amplitude spectrum in the 10 to 30 mHz band and fitting the sharpness of the first downswing in the KMBO P wave. The inversion result shown in Figure 3.6 provides a good fit to both but is somewhat more weighted toward fitting the amplitude spectrum because these network averaged quantities should be less sensitive to the affects of directivity and the details of the synthetic Green's function. The initial portion of the KMBO P wave is weighted higher than the latter to ensure that the behavior in the first 20 s is well modeled. This is the most well determined part of the STF because of the high-frequency waveform constraint. The large initial ramp in the low-frequency P waveform requires that a significant amount of moment release occurred before the mainshock. In the inversion presented in Figure 3.6 we smoothed the 0-12 s interval more than the mainshock interval. However, the STFs resulting from inversions with equal regularization at all times were very similar to the one shown in Figure 3.6 because the high-frequency envelope constraint effectively requires the moment release to be smooth in the 0-12 s interval. The continuation of the slow component from roughly 17 to 30 s is required by the flatness of the phase delay spectrum.

The initial portion of the slow component of the Prince Edward Island earthquake had a moment of 3×10^{18} Nm (M_w 6.3) despite having produced only an amplitude corresponding to a m_b 4.4 event at high frequencies (Figure 3.2). The initial duration of 12 s is large for an event of this seismic moment. For comparison, the 1995 Kobe earthquake ($M_o = 2 \times 10^{19}$ Nm) had a duration of <12 s even though its seismic moment was an order of magnitude larger (Ide *et al.*, 1996). Additionally, the 1994 Northridge event ($M_o = 1 \times 10^{19}$ Nm) had a duration of ~7 s (Dreger, 1994) despite being significantly larger than the initial slow component of the Prince Edward event. The total duration of the slow event, 30 s, is even longer. In contrast, the mainshock had a moment of 8×10^{18} Nm and only lasted ~5 s, a size and duration comparable to the Northridge event. Thus the Prince Edward Island event was a compound earthquake comprising both an ordinary, fast event (the mainshock), and a much longer duration episode of smooth moment release which primarily radiated energy at low frequencies. The high-frequency waveform constraint requires that the average moment acceleration during the initial portion of the slow event was ~2 orders of magnitude smaller than the moment acceleration during the mainshock. For a simple unilateral rupture the low initial moment accelerations imply that the product of the rupture and particle slip velocities was ~2 orders of magnitude smaller during the slow event than during the fast event.

3.3 Directivity

The low-frequency ramp resulting from the initial portion of the slow event is visi-

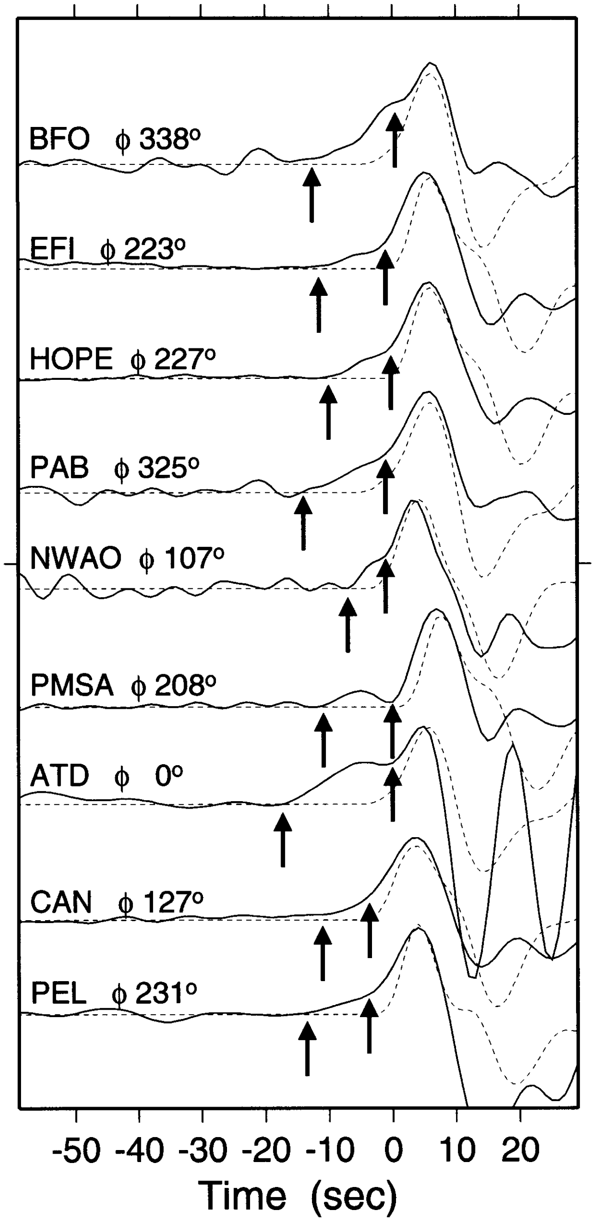

Figure 3-7: Vertical component displacement recordings (solid lines) of the P wave arrival at teleseismic stations shown in Figure 3.1a and Table 3.1. The records have been band-pass-filtered using a six pole butterworth filter with corners at 2 and 100 mHz. The traces are labeled with the station name and azimuth from north. Zero on the time axis corresponds to the P wave arrival time expected from the Harvard CMT location. Arrows show our picks for the arrivals of the initial low-frequency event and the mainshock. Stations to the north and northwest (PAB and KIEV) have the largest separation between arrivals, while stations to the southeast (NWAO) have the shortest separation. Epicentral distances for the stations are RAYN $\Delta = 65°$, NWAO $\Delta = 58°$, PMSA $\Delta = 59°$, EFI $\Delta = 64°$, HOPE $\Delta = 52°$, PAB $\Delta = 92°$, KIEV $\Delta = 93°$, and KIV $\Delta = 86°$. Synthetic seismograms are also shown (dashed lines) for a source at 15 km depth in an oceanic structure.

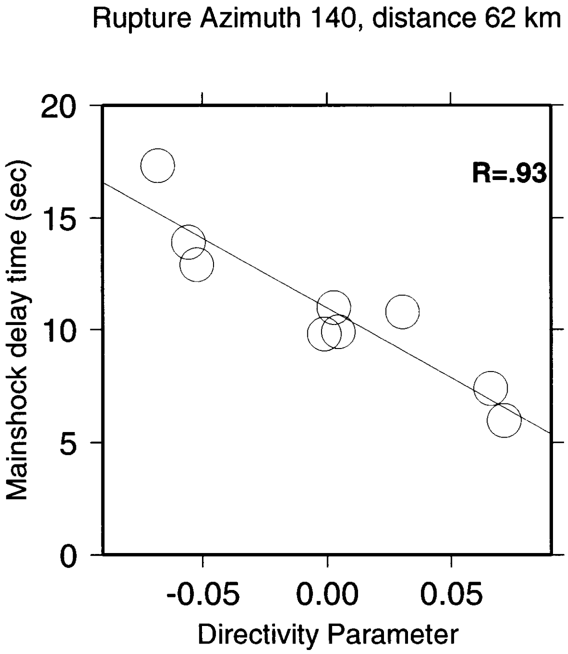

Figure 3-8: Delay times of the initiation of the mainshock relative to the start of the low-frequency ramp as a function of directivity parameter $p_i\cos(\phi_i)$ (where p_i is the ray parameter of the ith P wave and ϕ_i is the angle between the rupture direction and the ith station azimuth). The best fitting solution has a rupture azimuth of 45°. south of east, and a separation of 62 km and 11 s. The correlation coefficient for this solution is 0.93.

ble in teleseismic P waves at all azimuths. However, it varies significantly in duration and shape. At stations to the north and northwest the slow event starts almost 15 s before the mainshock and appears as a separate peak in the P wave (see Figure 3.7), while at stations to the southeast it begins <10 s before the mainshock and forms a short ramp. The variation with azimuth in the duration and character of the initial ramp suggests that the mainshock occurred significantly to the southeast of the slow event. While this variation is clear in the raw records, it is difficult to pick arrival times because of the low-pass filter required to see the slow event. To ensure a good signal-to-noise ratio and consistent features between stations, we picked the arrival of the slow event and the arrival of the mainshock on the nine teleseismic P waves for which both arrivals were clear on vertical component displacement records (which were band-pass-filtered between 2 and 100 mHz). We only used stations for which synthetic seismograms, calculated using a propagator matrix technique (Langston and Helmberger, 1975), showed impulsive first motions (Figure 3.7). The synthetic seismograms, like the observations of the 1998 event, demonstrate that the ramp is not a depth phase or other propagation effect. We then used the directivity parameter method (Beck and Ruff, 1984) to determine the azimuth of directivity and the spatial and temporal separation between the initiation of the slow component and the initiation of the mainshock. The differential arrival times T_i (Table 1) were fit to the expression $T_i = -p_i\cos(\phi_{\mathrm{rup}} - \phi_i)X + \tau$, where p_i is the ray parameter of the ith P wave, ϕ_i is the station azimuth (clockwise from north) for the ith P wave, ϕ_{rup} is an assumed rupture direction, and X and τ are the spatial and temporal separation between the two events, respectively. The rupture direction was determined by maximizing the correlation coefficient between the observed and computed differential times. For the delay times between the start of the slow event and the mainshock, the rupture direction with the highest correlation coefficient was $\phi_{\mathrm{rup}} = 140^\circ$ (R=0.93), and the estimates of the space and time separations were 62 ± 18 km and 11.0 ± 1 s (Figure 3.8). The apparent rupture velocity implied by this solution (5.6 ± 1.9 km/s) is probably larger than the shear wave velocity in the oceanic upper mantle (4.6 km/s).

We used high-frequency travel time picks from the South African array and other regional stations to perform a relative relocation of the initiation of the slow event with aftershocks and other nearby seismicity. At all of the stations with good signal-to-noise ratio, the first arrival times at high and low frequencies are indistinguishable. Thus, we believe that by using high-frequency first arrival picks we can get an accurate estimate of the location of the beginning of the slow event. The relocations were done using the hypocentroidal decomposition algorithm of Jordan and Sverdrup (1981), which yields both relative locations that are independent of common path anomalies and an estimate of the absolute position of the centroid of the cluster of events. Figure

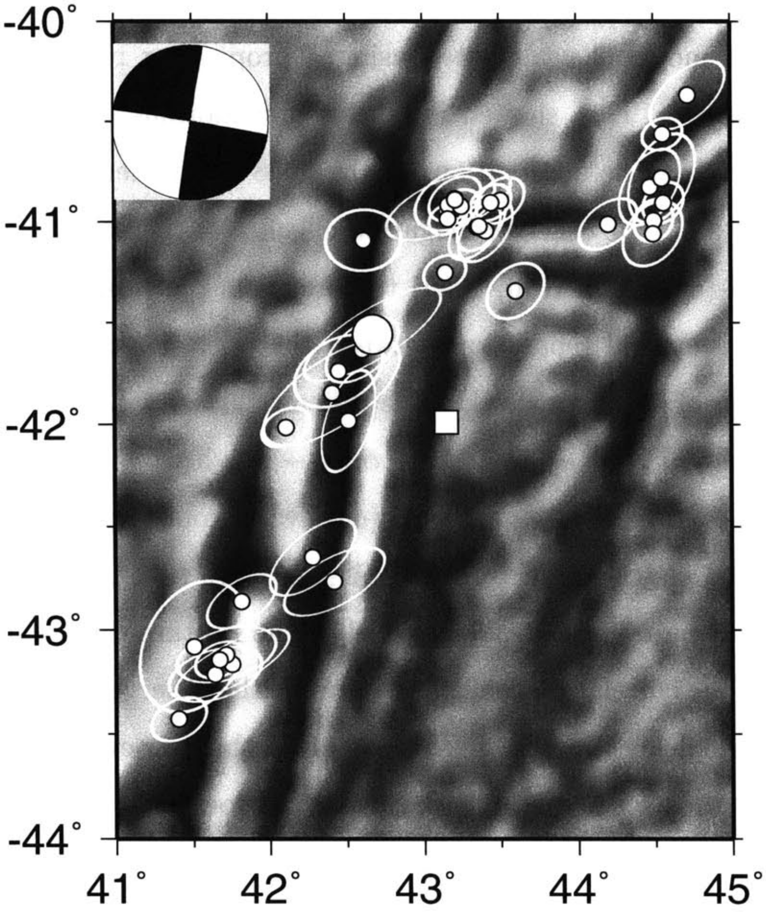

Figure 3-9: Map of the region of the April 28, 1997 earthquake. Relocated seismicity is plotted as points with 95% confidence ellipses along with the altimetric gravity field (Sandwell, 1995). The large circle in the main transform valley denotes the location of the initiation of the slow component, while the large square in the adjacent valley shows the initiation of the mainshock. The CMT focal mechanism is shown in the inset at the top left. The slow event and the mainshock appear to have ruptured separate faults because the nearly N-S striking nodal plane matches the strikes of both valleys and the strike of the conjugate plane does not match the relative rupture direction found in the directivity analysis.

Mainshock Delay Times

Station	Azimuth	Delta	Delay Time, s
BFO	337	95	12.9
EFI	228	64	11.0
HOPE	227	51	9.9
PAB	325	92	13.9
NWAO	107	58	6.0
PMSA	209	59	10.8
CAN	126	78	7.4
PEL	231	83	9.8
ATD	0	53	17.3

Table 3.1:

3.9 shows the results of the relocation plotted on top of the satellite gravity field (Sandwell, 1995). Between 41.25°S and 42.5°S, the Discovery II transform comprises two parallel, north-south striking valleys. The western valley has a stronger gravity signature and thus appears to be the main transform. The epicenter of the slow component and most of the background seismicity lie along this fault. Using the directivity (62 km at an azimuth of 140°) determined in section 3, we can plot the location of the mainshock on Figure 3.9 even though it was not part of the relocation inversion due to the limited number of arrival times. The mainshock was located in the parallel fault valley to the east of the main transform. Both the strike of the main transform fault and the moment tensor of the Prince Edward Island event preclude the possibility that rupture occurred on a fault connecting the epicenter and the mainshock (i.e., one with a strike of 140°).

3.4 Discussion

The 1997 Prince Edward Island earthquake comprised events of at least two characteristic durations, an ordinary, fast event of the order of a few seconds long and a slow event of the order of a few tens of seconds long. A foreshock (m_b 4.3) that occurred 2.5 hours prior to the main event may be indicative of a process of even longer duration. The slow component and the mainshock resulted from two types of rupture

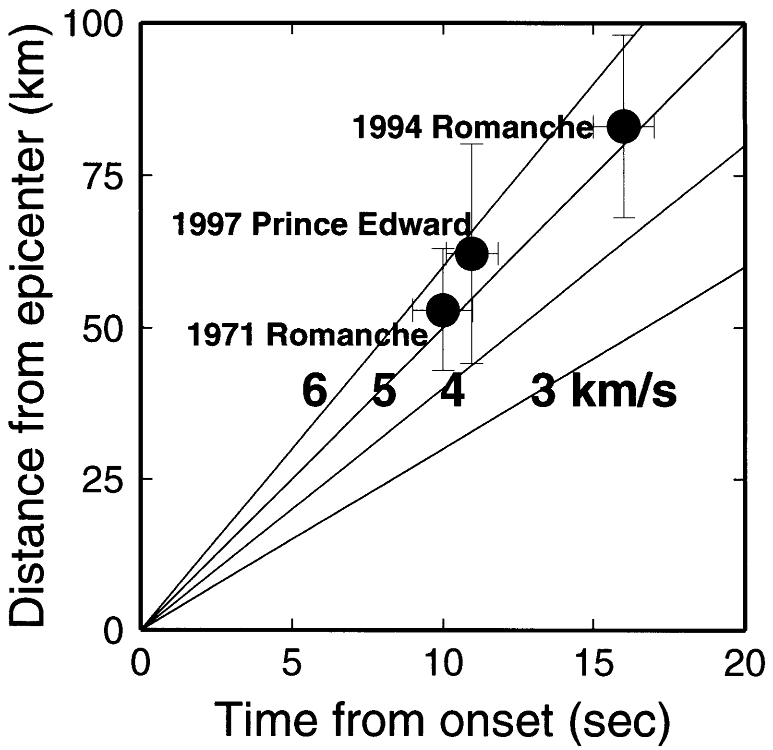

Figure 3-10: Comparison of the spatial and temporal separation between the epicenter and the location of the initiation of the mainshock for three oceanic transform fault events. For the events on the Romanche transform fault, the time and space separations were determined using the relative location algorithm described in the text and by McGuire *et al.* (1996) (the 1971 location is from Chapter 6 and Forsyth *et al.* (1986)). The Prince Edward event values were taken from Figure 8.

with very different kinematic properties. These differences, in rupture and/or particle slip velocities, resulted in lower moment accelerations during the slow component. The directivity signal shows that these two types of rupture occurred on different faults, suggesting that the variation in kinematical properties between events may be associated with differences in frictional properties of the two faults. The western fault is more prominent in the gravity field as well as the background seismicity and thus appears to accommodate the majority of the slip on this plate boundary. Although we do not yet understand the mechanism of slow earthquakes, the occurrence of the lower stress drop slow earthquake on the main transform relative to the fast event on the less active fault to the east is consistent with the idea that faults strengthen between slip events (Kanamori and Allen, 1986). This analogy may suggest that the more active transform had less time to heal between events and therefore ruptured in a lower stress drop event.

The Prince Edward Island event shows many similarities to the 1994 Romanche transform earthquake (McGuire *et al.*, 1996). The most striking similarity is that both events involved slip on two parallel transform faults. This also appears to be true for a M_s 7.0 event in 1971 on the Romanche [Forsyth et al. 1986, J. J. McGuire and T. H. Jordan, unpublished material, 1999]. In all three cases the apparent rupture velocity between the event on the main transform and the event on the secondary parallel fault was of the order of 5 km/s (Figure 3.10). This implies that any causal relationship between the initial rupture and the mainshock would have to occur due to some dynamic mechanism related to the passage of the P wave. However, in the case of the 1994 Romanche event, a 100-s slow precursor also occurred which could have triggered the mainshock through quasi-static loading. While the mechanism which causes multiple faults to rupture in one event remains undetermined, the Prince Edward event provides further evidence that some oceanic transform fault earthquakes are "slow" because they involve both a component of rupture which primarily radiates energy at low frequencies and a normal, fast earthquake.

Acknowledgments. We would like to thank the entire Kaapvaal Working Group (James *et al.*, 1998) for providing the best collection of nearby recordings we have seen for an oceanic transform fault slow earthquake. In particular, we thank Rebecca Saltzer for help with using the South Africa data set. All figures were generated using the GMT software freely distributed by Wessel and Smith (1991).

Chapter 4

Measuring the Second-Degree Moments of Earthquake Space-Time Distributions

Abstract

Determining detailed descriptions of the space-time distribution of an earthquake's rupture using only teleseismic data is often a difficult and non-unique process. However, a description of an earthquake which goes beyond a point source is often needed for many seismo-tectonic problems. We have developed a method which inverts measurements of the travel-time and amplitude of various seismic phases at global stations for the second degree polynomial moments of an event's space-time distribution. Our values for the 2nd moments of the 1995, M_w 8.0, Jalisco, Mexico, thrust event correspond to a characteristic rupture length of 121±32 km along strike, a characteristic rupture width of 76±36 km downdip, a characteristic duration of 29±5 s, and a direction of rupture propagation along the strike of the subduction zone to the NW. For the 1995, M_w 7.2, Gulf of Aqaba earthquake, our estimates of the 2nd moments correspond to a characteristic rupture length of 65±14 km, a characteristic duration of 9±1 s, and rupture propagation to the NE along the strike of the Dead Sea Trans-

form. Our estimates of the 1st and 2nd moments agree well with values from local seismic and geodetic networks. For both the Jalisco and Aqaba events, we are able to resolve the fault-plane ambiguity associated with the events' moment-tensors using our estimates of the 2nd spatial moment.

4.1 Introduction

The spatial and temporal distribution of earthquake moment release has a large effect on the displacement field observed at locations near the fault. This strong dependence has enabled seismologists to image the space-time evolution of the rupture of earthquakes recorded by nearby instruments in remarkable detail (Wald and Heaton, 1994; Ide *et al.*, 1996). However, abundant near-field data has been lacking except in regions of dense regional seismic networks, such as California and Japan. This has motivated a large amount of work on imaging earthquake ruptures from teleseismic data. Such far-away observations have limited resolution, however, Ihmlé (1998) recently showed that P-wave inversions for the M_w 8.2 Bolivia deep earthquake, which had good teleseismic coverage and relatively simple P-wave propagation, were unable to differentiate between a slip distribution composed of compact subevents and one composed of widely distributed slip. This inherent non-uniqueness is often associated with a choice of the spatial smoothing parameter that is used to regularize these inversions (Ihmlé, 1998). Imaging the slip distribution of large earthquakes is further complicated because P waves provide only weak constraints on the total moment of an event (Ekström, 1989). Thus, attempts to determine the details of slip distributions for earthquakes that are only recorded teleseismically are at best extremely non-unique. There are several important properties of an earthquake's space-time behavior that do not require this type of detailed finite-fault inversion, such as resolution of the fault-plane ambiguity, approximate extent of the rupture area, duration, and the direction of rupture propagation. In this paper, we develop a method for robustly estimating these large-scale features of the slip distribution from teleseismic data.

In the normal-mode formulation, the spatial and temporal extent of an earthquake's rupture enters the equation for the displacement $\mathbf{u}$ at a position $\mathbf{x}$ through the stress-glut rate tensor $\dot{\mathbf{\Gamma}}(\mathbf{r}, t)$:

$$\mathbf{u}(\mathbf{x}, t) = Re \sum_{k} (i\omega_k)^{-2} \mathbf{s}_k(\mathbf{x}) \mathrm{C}_k \exp(-i\omega_k t \; - \; \alpha_k t), \tag{4.1}$$

where

$$C_k = \iint \dot{\mathbf{\Gamma}}(\mathbf{r}, t) : \mathbf{E}_k^*(\mathbf{r}) e^{i\omega_k t} \, dV \, dt \,, \tag{4.2}$$

and $\mathbf{s}_k$ is the eigenfunction of the kth mode which has eigenfrequency ω_k, attenuation parameter α_k, and associated strain $\mathbf{E}_k$. $\dot{\mathbf{\Gamma}}(\mathbf{r}, t)$, introduced and described in detail by Backus and Mulcahy (1976a,b), is non-zero only in the region of non-elastic deformation, i.e. the source volume. In this paper, we assume that $\dot{\mathbf{\Gamma}}(\mathbf{r}, t)$ has the form

$$\dot{\mathbf{\Gamma}}(\mathbf{r}, t) = \hat{\mathbf{M}} \, \dot{f}(\mathbf{r}, t), \tag{4.3}$$

where $\hat{\mathbf{M}}$ is a unit-norm moment tensor and $\dot{f}(\mathbf{r}, t)$ is the scalar space-time function. For slip on a simple fault, this assumption is equivalent to requiring a constant orientation of the fault plane and slip vector, but it allows also slip on parallel faults. In contrast to near-field inversions which seek to determine a detailed parameterization of $\dot{f}(\mathbf{r}, t)$, we will invert for the polynomial moments of $\dot{f}(\mathbf{r}, t)$, $\mu^{(i,j)}$, which have spatial degree i, temporal degree j, and total degree $i + j$. The zeroth degree moment

$$\mu^{(0,0)} = \iint \dot{f}(\mathbf{r}, t) \, dV \, dt \tag{4.4}$$

is the standard seismic moment, M_0, while the normalized first degree moments

$\boldsymbol{\mu}^{(1,0)}/M_0$ and $\mu^{(0,1)}/M_0$ give the spatial and temporal centroids, respectively.

$$\boldsymbol{\mu}^{(1,0)} = \iint \dot{f}(\mathbf{r},t)\ \mathbf{r}\, dV\, dt, \qquad \mu^{(0,1)} = \iint \dot{f}(\mathbf{r},t)\, t\, dV\, dt\,. \tag{4.5}$$

The degree-two moments about a point $\mathbf{r}_0$ and time t_0 are called central moments when $\mathbf{r}_0 = \boldsymbol{\mu}^{(1,0)}/M_0$ and $t_0 = \mu^{(0,1)}/M_0$:

$$\hat{\boldsymbol{\mu}}^{(2,0)} = \begin{bmatrix} \hat{\mu}_{rr} & \hat{\mu}_{r\theta} & \hat{\mu}_{r\phi} \\ \hat{\mu}_{r\theta} & \hat{\mu}_{\theta\theta} & \hat{\mu}_{\theta\phi} \\ \hat{\mu}_{r\phi} & \hat{\mu}_{\theta\phi} & \hat{\mu}_{\phi\phi} \end{bmatrix} = \iint \dot{f}(\mathbf{r},t)\ (\mathbf{r}-\mathbf{r}_0)(\mathbf{r}-\mathbf{r}_0)^{\mathrm{T}}\, dV\, dt\,, \tag{4.6}$$

$$\hat{\mu}^{(0,2)} = \iint \dot{f}(\mathbf{r},t)\ (t-t_0)^2\, dV\, dt, \qquad \hat{\boldsymbol{\mu}}^{(1,1)} = \iint \dot{f}(\mathbf{r},t)\ (\mathbf{r}-\mathbf{r}_0)\ (t-t_0)\, dV\, dt\,. \tag{4.7}$$

The coordinate system axes (r, θ, ϕ) correspond to radius, co-latitude, and longitude respectively. If the degree two moments are calculated about a point that is slightly offset from the true centroid location, there is a small difference between the 2nd moment and the 2nd central moment:

$$\hat{\boldsymbol{\mu}}^{(2,0)} = \boldsymbol{\mu}^{(2,0)} - \boldsymbol{\mu}^{(1,0)}\boldsymbol{\mu}^{(1,0)^{\mathrm{T}}} \tag{4.8}$$

The second central moments describe the spatial and temporal extent of the source. Following Backus (1977a) and Silver and Jordan (1983), we can define the characteristic dimension, $x_c(\hat{\mathbf{n}})$, of the source region in a direction $\hat{\mathbf{n}}$, the characteristic duration τ_c, the characteristic (or apparent rupture) velocity v_c and the average velocity of the instantaneous spatial centroid, $\mathbf{v}_0$:

$$x_c(\hat{\mathbf{n}}) = 2\sqrt{\hat{\mathbf{n}}^{\mathrm{T}}\left[\hat{\boldsymbol{\mu}}^{(2,0)}/\mu^{(0,0)}\right]\hat{\mathbf{n}}}\,,\ \tau_c = 2\sqrt{\hat{\mu}^{(0,2)}/\mu^{(0,0)}}\,,$$

$$v_c = L_c/\tau_c\,,\ \mathbf{v}_0 = \hat{\boldsymbol{\mu}}^{(1,1)}/\hat{\mu}^{(0,2)}, \tag{4.9}$$

where L_c is the maximum value of x_c and denotes the characterisitc rupture length along the direction of the eigenvector associated with the largest eigenvalue of $\hat{\boldsymbol{\mu}}^{(2,0)}$.

A number of theoretical papers on 2nd moments have examined the non-uniqueness in source inversions and the relationships between 2nd moments and standard source-models (Backus, 1977b; Okal, 1982; Doornbos, 1982a,b; Pavlov, 1994; Das and Kostrov, 1997), but prior observational work on determining the polynomial moments of an earthquakes has been limited to the inversion of body-waveform data (Gusev and Pavlov, 1988) or surface-wave amplitude spectra assuming a fault plane *a priori* (Bukchin, 1995). In this paper, we develop a formalism for inverting frequency-dependent travel-time and amplitude measurements for the source moments of polynomial degrees zero, one, and two. Data are obtained for arbitrary wavegroups, such as surface waves and body waves, as differential measurements relative to synthetics computed for a point source in a three-dimensional earth model.

4.2 Frequency-Dependent Phase and Amplitude Data

We measure the phase and amplitude of a target wave group relative to a synthetic seismogram using the GSDF technique of Gee and Jordan (1992). The synthetic seismogram, $\tilde{s}$, is represented as a sum over traveling wave groups, indexed by mode number n. In the frequency domain, it is assumed that the data seismogram, s, can be related to the synthetic by small differences in phase delay, $\delta\tau_p^n$, and amplitude reduction time, $\delta\tau_q^n$:

$$s(\omega) = \sum_n \tilde{s}_n(\omega)\, e^{i\omega\delta\tau_p^n(\omega)\, -\, \omega\delta\tau_q^n(\omega)} \tag{4.10}$$

GSDF measurements of the generalized travel time, $\delta\tau_p^n(\omega)$, have been utilized in a variety of structural inverse problems (Gaherty *et al.*, 1996; Katzman *et al.*, 1998) because the relationships between $\delta\tau_p^n(\omega)$ and structural model parameters are easily linearized. In these studies, synthetic seismograms were calculated for short-duration earthquakes ($M_w \sim 6$) using a one-dimensional earth model, and the phase delays of

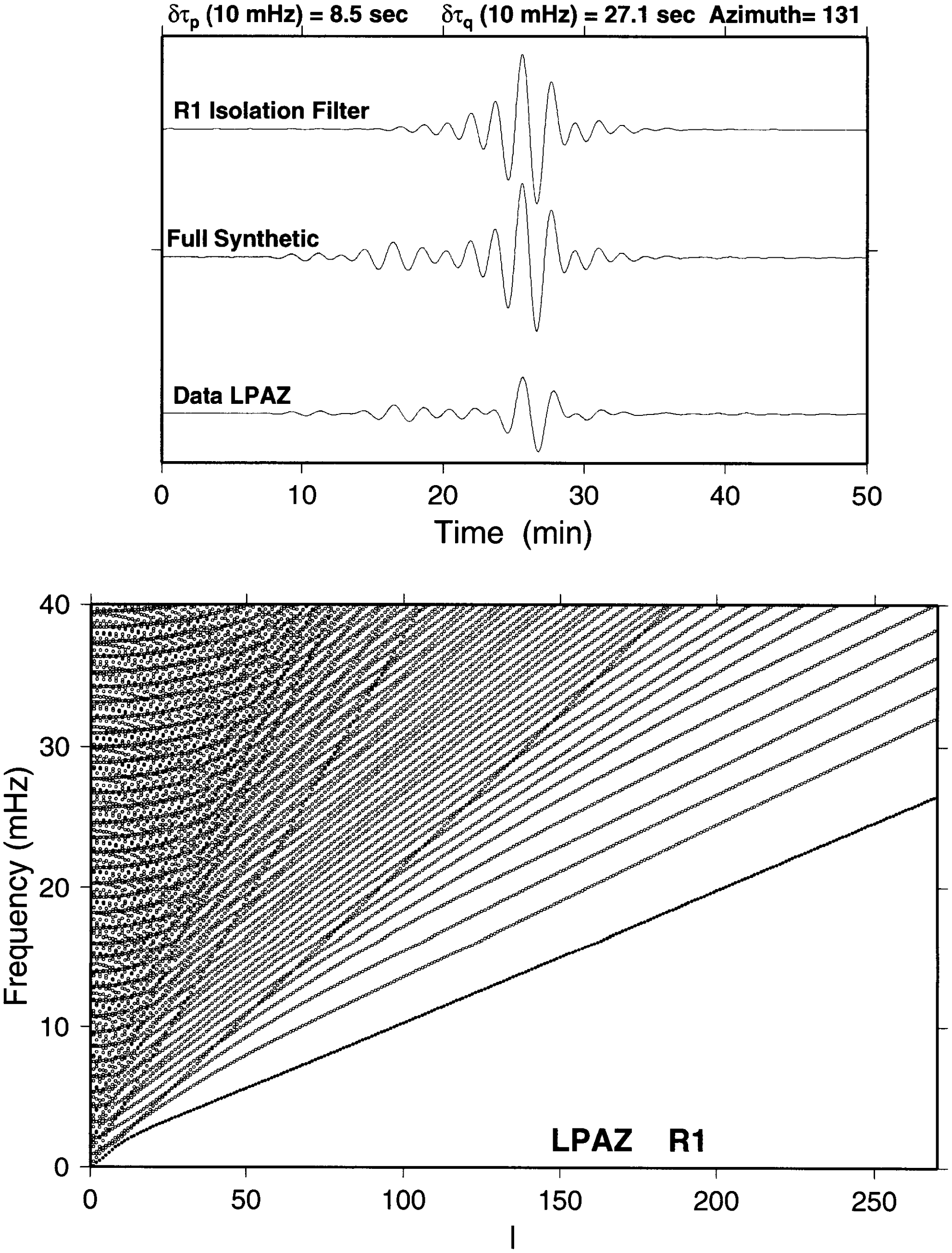

Figure 4-1: Examples of isolation filters. The R1 isolation filter in the top panel was made by summing only the modes in shown in blue in the PREM dispersion diagram in the bottom panel. The full synthetic was calculated by summing all the spheroidal modes of the PREM earth model (ie the bottom panel). All three traces in the top panel have been narrow-band filtered around 10 mHz.

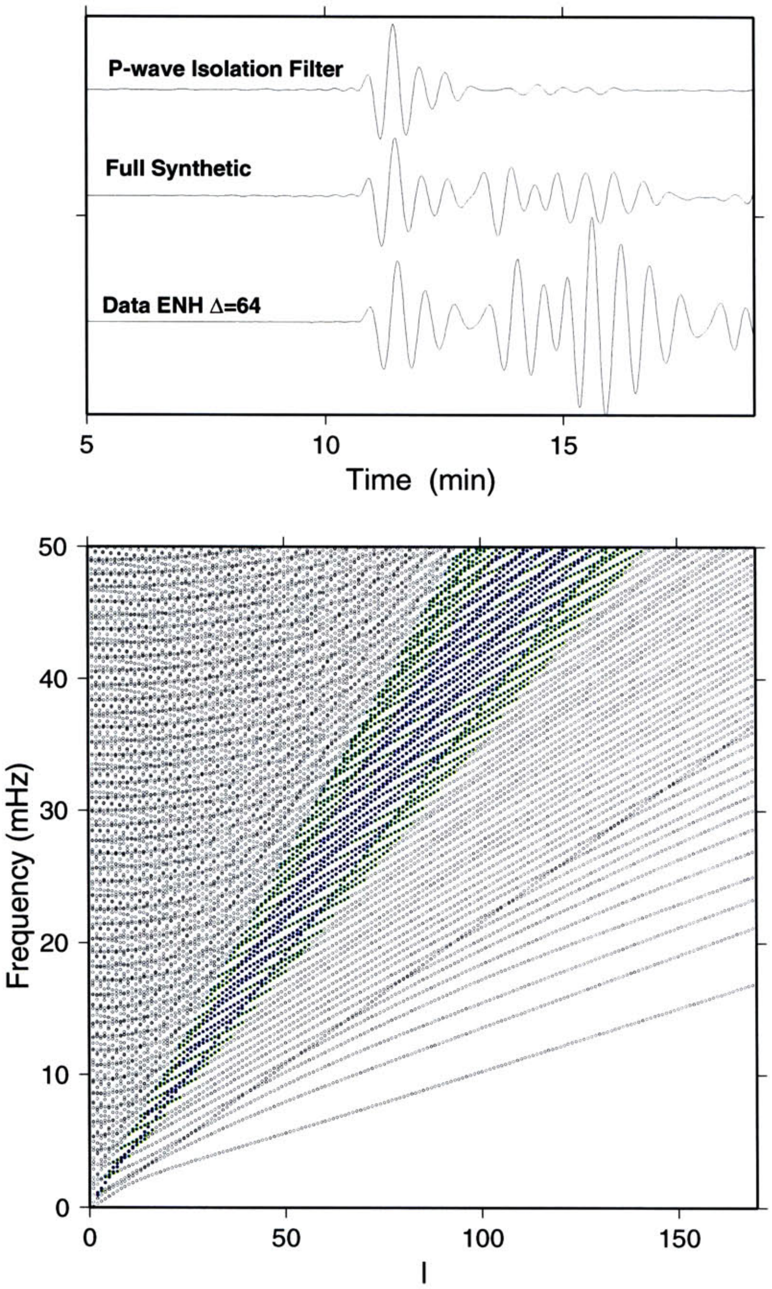

Figure 4-1: Examples of isolation filters. The P-wave isolation filter in the top panel was made by summing the modes shown in green and blue in the bottom panel. The modes shown in blue had weights of 1, and they approximate P-wave branches on the dispersion diagram. The modes shown in green were somewhat down-weighted for the isolation filter calculation but not for the full synthetic calculation. Modes shown in black were not included in the summation for the isolation filter, but were included (at weight=1) in the full synthetic. All three traces were narrow-band filtered around 35 mHz.

the data were attributed to structural variability along the path between the source and station. Here, we study large earthquakes ($M_w \geq 7.0$) that cannot adequately be represented as point sources, even at low-frequencies. We make approximate corrections for earth structure using a three-dimensional earth model, so that our measurements of $\delta\tau_p^n$ and $\delta\tau_q^n$ can be attributed primarily to properties of the seismic source.

The synthetic seismograms in this study were calculated for a point source in both space and time through normal-mode summation for the PREM earth model (Dziewonski and Anderson, 1981), corrected for three dimensional elastic structure using the degree-12 aspherical model of Su *et al.* (1994) and the asymptotic approximations of Woodhouse and Dziewonski (1984). We also corrected fundamental modes above 7 mHz for smaller scale heterogeneity using the degree-40 phase-velocity maps of Ekström *et al.* (1997). The 3-D corrections only offset the phase of the surface-wave arrivals; no corrections are made to the amplitudes for the effects of 3-D anelastic structure or focusing and defocusing. The source is specified by a centroid location, centroid time, and moment tensor from the Harvard CMT catalog (Dziewonski *et al.*, 1999). To limit any contributions to our measurements by lateral heterogeneity unaccounted for by the 3-D models, we restricted our measurements of surface waves to low-frequencies ($\leq$ 20 mHz), and we omitted any stations for which our synthetic seismograms did not closely resemble the observed seismograms.

The first step in the measurement process was the creation of an isolation filter by a weighted summation of normal modes. The isolation filter was designed to approximate the complete synthetic in the time interval containing a target wavegroup and decay to zero outside that interval (Figure 4-1). The isolation filter is then cross-correlated with both the complete synthetic and the data seismograms. The resulting cross-correlagrams were windowed to localize the signals in the time domain and then put through a series of narrow-band filters (with center frequencies ω_i) to localize them in the frequency domain. The windowed and filtered cross-correlagrams were then fit with two 5 parameter Gaussian wavelets from which the phase and amplitude parameters, $\delta\tau_p(\omega_i)$ and $\delta\tau_q(\omega_i)$, were calculated (Gee and Jordan, 1992). This procedure corrects for the interference between the phase targeted by the isolation filter and other arrivals on the seismogram, as well as the biases introduced by the windowing and filtering operations. For shallow earthquakes, we typically made measurements on vertical component seismograms for fundamental mode Rayleigh waves at frequencies between 3 and 20 mHz and for P waves between 10 and 50 mHz.

4.3 Effects of an Extended Source on GSDF Measurements

To relate the differences between the point-source synthetic and data seismograms to our source parameterization, we determined the partial derivatives of $\delta\tau_p^n$ and $\delta\tau_q^n$ with respect to the polynomial moments of $\dot{f}(\mathbf{r}, t)$. A Taylor-series expansion truncated to second order gives the expression relating a point source seismogram, $\tilde{s}$, to the seismogram resulting from an extended source, s:

$$\begin{aligned} s(\mathbf{r}_\mathrm{R}, \omega) = \frac{1}{M_0}[M_0 + i\omega\mu^{(0,1)} + \boldsymbol{\mu}^{(1,0)} \cdot \boldsymbol{\nabla}_\mathrm{S} - \frac{\omega^2}{2}\mu^{(0,2)} \\ + i\omega\boldsymbol{\mu}^{(1,1)} \cdot \boldsymbol{\nabla}_\mathrm{S} + \frac{1}{2}\boldsymbol{\mu}^{(2,0)} : \boldsymbol{\nabla}_\mathrm{S}\boldsymbol{\nabla}_\mathrm{S}]\tilde{s}(\mathbf{r}_\mathrm{R}, \mathbf{r}_\mathrm{S}, t_\mathrm{S}, \omega) \, , \end{aligned} \tag{4.11}$$

where $\mathbf{r}_\mathrm{R}$ and $\mathbf{r}_\mathrm{S}$ are the receiver and point-source locations respectively, t_S is the point source time, and $\boldsymbol{\mu}^{(1,0)}$ and $\mu^{(0,1)}$ represent any deviation of the centroid $(\mathbf{r}_0, t_0)$ from the point-source location. In the GSDF formalism, $\tilde{s}$ and s are represented as sums over traveling modes:

$$\tilde{s}(\omega) = \sum_n e^{i\omega\tau_p^n(\omega) \, - \, \omega\tau_q^n(\omega)} \, , \tag{4.12}$$

$$s(\omega) = \sum_n e^{i\omega(\tau_p^n(\omega)+\delta\tau_p^n(\omega)) \, - \, \omega(\tau_q^n(\omega)+\delta\tau_q^n(\omega))} \, . \tag{4.13}$$

To obtain the explicit expression for $\tilde{s}$, we converted the expression for the synthetic seismogram from a sum over normal modes to a sum over traveling modes using the Poisson-sum formula (Appendix A):

$$\tilde{s}(\omega) = \sum_n [A_n(\omega) + iB_n(\omega)] e^{i(\lambda_n + \delta\lambda_n)\Delta - i\pi/4} \,, \tag{4.14}$$

where Δ is the epicentral distance, $A_n(\omega)$ and $B_n(\omega)$ depend on the eigenfunctions of the PREM earth model, the assumed centroid moment tensor, and the epicentral distance. The perturbations to the continuous wavenumber, $\delta\lambda_n$, account for the corrections made to the synthetics for three dimensional Earth structure (Appendix A). Equations (12) and (14) yield expressions for $\tau_p^n(\omega)$ and $\tau_q^n(\omega)$:

$$\tau_p^n(\omega) = [(\lambda_n + \delta\lambda_n)\Delta + \arctan(B_n/A_n) - \pi/4]/\omega \,, \tag{4.15}$$

$$\tau_q^n = -(1/\omega)\ln(\sqrt{A_n^2 + B_n^2}) \,. \tag{4.16}$$

Substituting equations (12) and (13) into (11) and making the low-frequency approximation,

$$e^{i\omega\delta\tau_p^n(\omega) \, - \, \omega\delta\tau_q^n(\omega)} \approx 1 + i\omega\delta\tau_p^n(\omega) \; - \; \omega\delta\tau_q^n(\omega) \,, \tag{4.17}$$

gives the following formula for $\delta\tau_p^n(\omega)$ and $\delta\tau_q^n(\omega)$:

$$\begin{aligned} \delta\tau_p^n(\omega) = \frac{1}{M_0}[\mu^{(0,1)} &+ \boldsymbol{\mu}^{(1,0)} \cdot \boldsymbol{\nabla}_{\mathrm{S}}\tau_p^n + \omega\boldsymbol{\mu}^{(1,1)} \cdot \boldsymbol{\nabla}_{\mathrm{S}}\tau_q^n \\ &+ \boldsymbol{\mu}^{(2,0)} : (\boldsymbol{\nabla}_{\mathrm{S}}\boldsymbol{\nabla}_{\mathrm{S}}\tau_p^n - \omega\boldsymbol{\nabla}_{\mathrm{S}}\tau_p^n\boldsymbol{\nabla}_{\mathrm{S}}\tau_q^n - \omega\boldsymbol{\nabla}_{\mathrm{S}}\tau_q^n\boldsymbol{\nabla}_{\mathrm{S}}\tau_p^n)], \end{aligned} \tag{4.18}$$

$$\delta\tau_q^n(\omega) = \frac{1}{M_0}[\boldsymbol{\mu}^{(1,0)} \cdot \boldsymbol{\nabla}_{\mathrm{S}}\tau_q^n + \frac{\omega}{2}\mu^{(0,2)} + \omega\boldsymbol{\mu}^{(1,1)} \cdot \boldsymbol{\nabla}_{\mathrm{S}}\tau_p^n \\ + \boldsymbol{\mu}^{(2,0)} : (\boldsymbol{\nabla}_{\mathrm{S}}\boldsymbol{\nabla}_{\mathrm{S}}\tau_q^n + \omega\boldsymbol{\nabla}_{\mathrm{S}}\tau_p^n\boldsymbol{\nabla}_{\mathrm{S}}\tau_p^n - \omega\boldsymbol{\nabla}_{\mathrm{S}}\tau_q^n\boldsymbol{\nabla}_{\mathrm{S}}\tau_q^n)]. \tag{4.19}$$

Expressions for the terms involving τ_q^n and τ_p^n are calculated from (15) and (16). The partial derivatives of $\delta\tau_p^n$ and $\delta\tau_q^n$ with respect to the 14 independent elements of $\mu^{(0,1)}$, $\boldsymbol{\mu}^{(1,0)}$, $\mu^{(0,2)}$, $\boldsymbol{\mu}^{(1,1)}$, and $\boldsymbol{\mu}^{(2,0)}$ can be simply read off from equations (18) and (19). We have also calculated the partial derivatives of the GSDF measurements with respect to changes in the moment tensor elements, M_{ij}, using the expressions:

$$\frac{\partial\tau_p^n(\omega)}{\partial M_{ij}} = \frac{\partial\tau_p^n(\omega)}{\partial A_n}\frac{\partial A_n}{\partial M_{ij}} + \frac{\partial\tau_p^n(\omega)}{\partial B_n}\frac{\partial B_n}{\partial M_{ij}}, \tag{4.20}$$

$$\frac{\partial\tau_q^n(\omega)}{\partial M_{ij}} = \frac{\partial\tau_q^n(\omega)}{\partial A_n}\frac{\partial A_n}{\partial M_{ij}} + \frac{\partial\tau_q^n(\omega)}{\partial B_n}\frac{\partial B_n}{\partial M_{ij}}. \tag{4.21}$$

In practice, isolation filters for most phases involve contributions from a large number of normal modes ranging over multiple values of the overtone number n. Thus the measured values of $\delta\tau_p$ and $\delta\tau_q$ will be a weighted sum over the $\delta\tau_p^n$ and $\delta\tau_q^n$ for the individual branches that contribute to the isolation filter. The partial derivative of a GSDF measurement can also be calculated by a weighted sum of the partial derivatives of the individual branches [Gee and Jordan, 1992, equations 94-95]. Figure 4-1 shows examples of the isolation filters for the P wave and the Rayleigh wave from a shallow source along with the normal-mode weights used to calculate the filters. Only the fundamental mode branch is needed to match the Rayleigh wave, while contributions from several branches are needed to match the P wave. While all of the GSDF measurements in this paper were made on vertical component records of either fundamental mode Rayleigh waves or P-waves, the technique is completely generalizable to an arbitrary waveform. Thus, intermediate and deep earthquakes can be studied by the inclusion of higher-mode surface waves. Additionally, 2nd-orbit surface waves can be used to increase azimuthal coverage of the source (Appendix A). In the future, we will incorporate Love and other S_{H} waves to improve our resolution of the higher moments.

4.3.1 Examples of Partial Derivatives

Several intuitive properties can be seen in the partial derivatives (Figure 4-2) for the Rayleigh-wave isolation filter shown in Figure 4-1. The effect of a shift in centroid time, $\mu^{(0,1)}$, on the frequency-dependent arrival times $\delta\tau_p(\omega)$ is independent of azimuth, and this type of shift has no effect on the frequency-dependent amplitude parameter $\delta\tau_q(\omega)$. $\partial\delta\tau_p/\partial\mu_\phi^{(1,0)}$ shows a cosine dependence on azimuth with a maximum at 270°. This pattern corresponds to late arrivals at stations to the west and early arrivals at stations to the east owing to an eastwardly shift in the centroid location. A similar pattern, shifted by 90°, is found for $\partial\delta\tau_p/\partial\mu_\theta^{(1,0)}$. These travel time shifts due to a mislocated $\mathbf{r}_S$ are independent of frequency. From the Taylor-series approximation (10), we see that the centroid depth, $\mu_r^{(1,0)}$, is the only component of the 1st-degree moment that perturbs the amplitude reduction time, $\delta\tau_q$. In contrast, the degree-2 moments primarily perturb the $\delta\tau_q$ measurements, having almost no influence on $\delta\tau_p$. $\partial\delta\tau_q/\partial\hat{\mu}_\phi^{(1,1)}$ approximates a cosine in azimuth and increases in amplitude with frequency. This behavior is just the directivity pattern of Ben-Menahem (1961), which has been used in many studies to infer directivity from surface waves. The $\phi\phi$ component of $\hat{\boldsymbol{\mu}}^{(2,0)}$ is non-zero for sources with finite extent in the east-west direction. $\partial\delta\tau_q/\partial\hat{\mu}_{\phi\phi}^{(2,0)}$ has positive values (i.e., decreased data amplitudes) at stations to both the east and west due to destructive interference (Figure 4-3). $\partial\delta\tau_q/\partial\hat{\mu}^{(0,2)}$ is independent of azimuth, but increases in amplitude with frequency, corresponding to the spectral roll-off expected for a source of finite duration.

Figure 4-3 shows the GSDF measurements that result from two simple models of an extended earthquake source, unilateral and bilateral rupture. In these calculations, the centroid and moment tensor are known exactly, and $\dot{f}(\mathbf{r},t)$ is symmetric about the centroid, so the dominant contribution comes from the 2nd moments. In both cases,

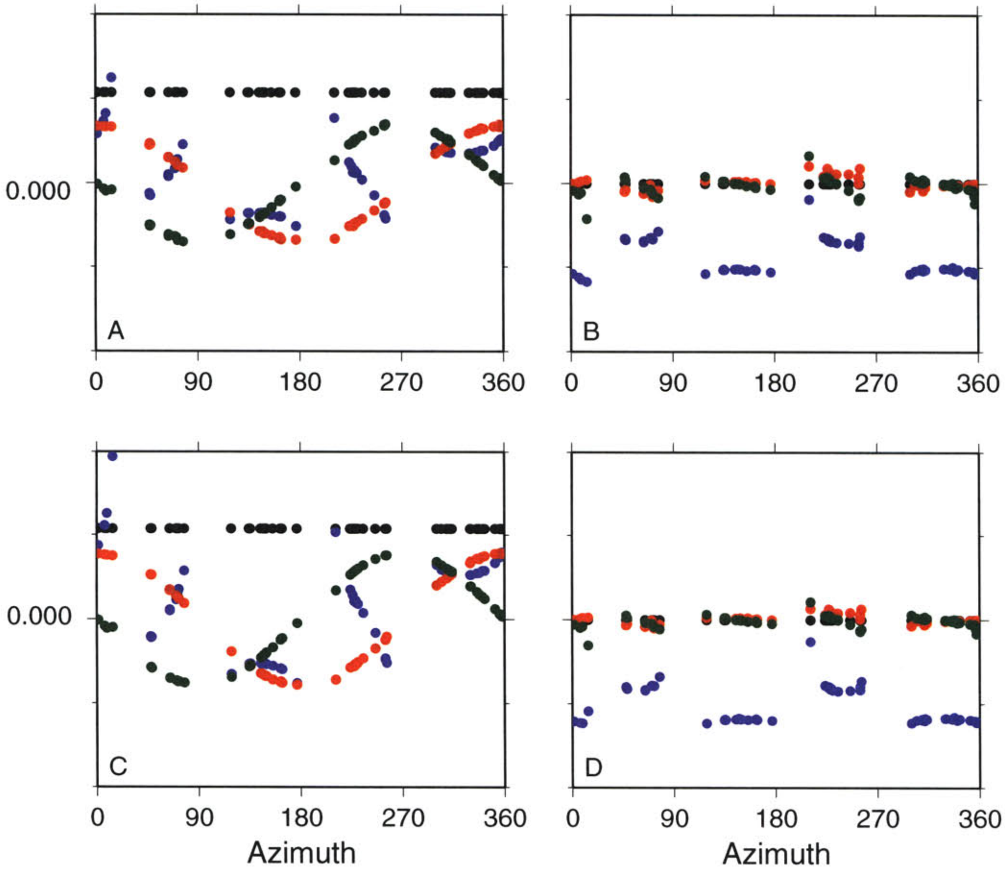

Figure 4-2: Examples of the partial derivatives of the GSDF measurements for the fundamental mode Rayleigh wave. The partials are for $\delta\tau_p(\omega)$ (A,C,E,G) and $\delta\tau_q(\omega)$ (B,D,F,H) at frequencies of 3.5 mHz (A,B,E,F) and 5.0 mHz (C,D,G,H) mHz. A-D) Partials with respect to the 1st moments, centroid time (black), longitude (green), co-latitude (red), and depth(blue). Y-axis tick marks are every .0026 $\mathrm{s}/(10^{20}\mathrm{Nm}-\mathrm{s})$, .001 $\mathrm{s}/(10^{20}\mathrm{Nm}-\mathrm{km})$, .0008 $\mathrm{s}/(10^{20}\mathrm{Nm}-\mathrm{km})$, and .0008 $\mathrm{s}/(10^{20}\mathrm{Nm}-\mathrm{km})$, for $\mu^{(0,1)}$, $\mu_r^{(1,0)}$, $\mu_\theta^{(1,0)}$, and $\mu_\phi^{(1,0)}$ respectively.

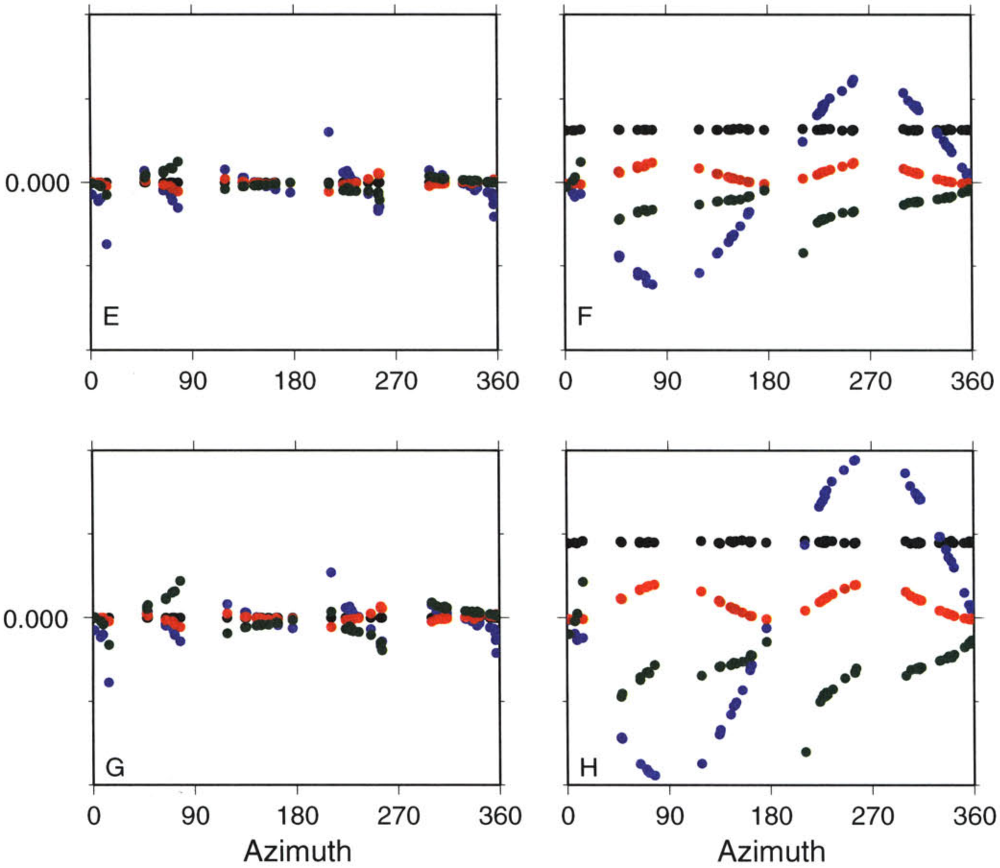

Figure 4-2: E-H) partials with respect to the 2nd moments $\hat{\mu}_{\phi\phi}^{(2,0)}$ (red),$\hat{\mu}_{rr}^{(2,0)}$ (green) $\hat{\mu}^{(0,2)}$ (black), $\hat{\mu}_{\phi}^{(1,1)}$ (blue). Y-axis tick marks are every .000053 $\mathrm{s}/(10^{20}\mathrm{Nm}-\mathrm{s}^2)$, .000011 $\mathrm{s}/(10^{20}\mathrm{Nm}-\mathrm{km}-\mathrm{s})$, and .000011 $\mathrm{s}/(10^{20}\mathrm{Nm}-\mathrm{km}^2)$ for $\mu^{(0,2)}$, $\mu_{\phi}^{(1,1)}$, and $\mu_{\phi\phi}^{(2,0)}$ respectively.

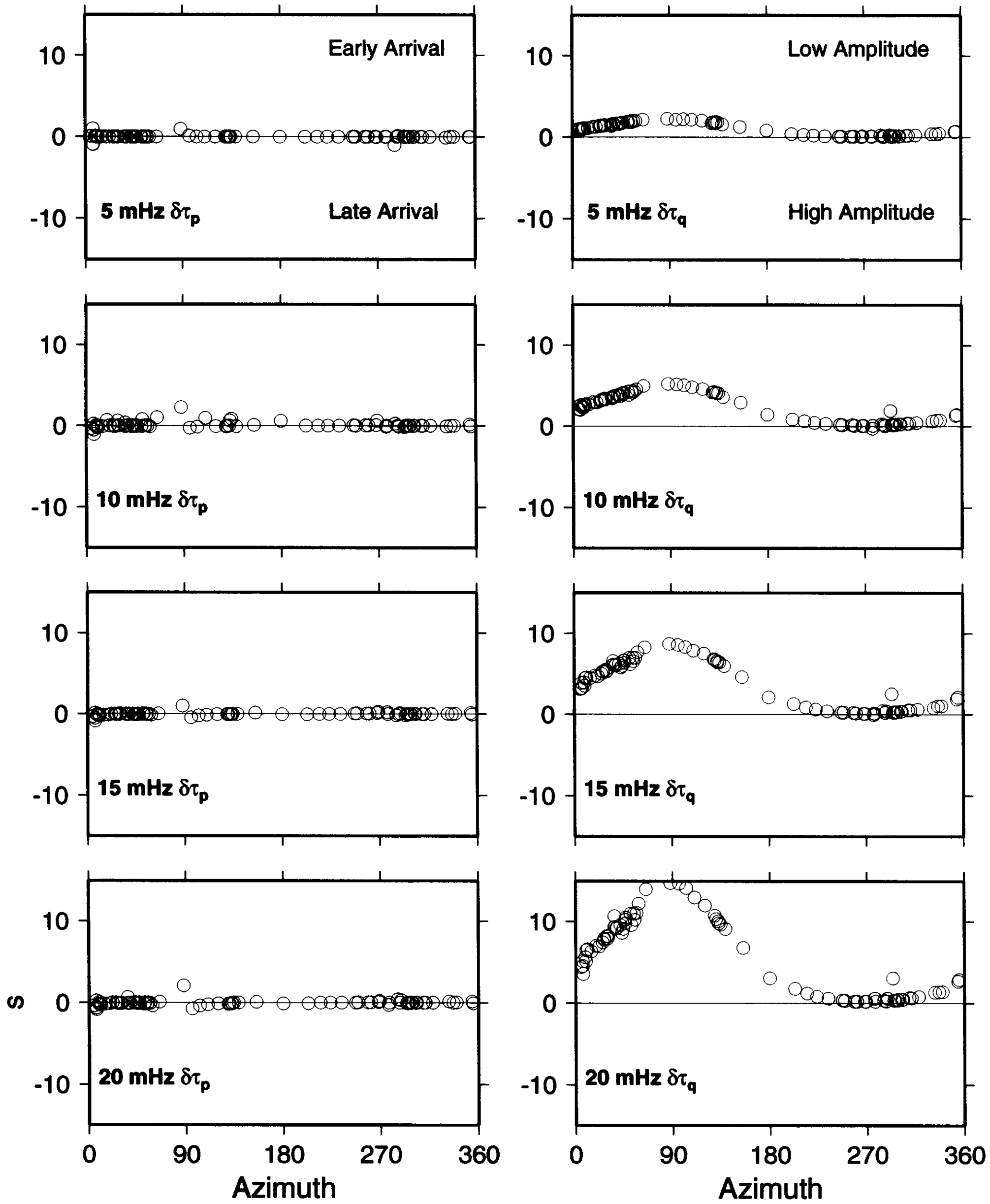

Figure 4-3: A. GSDF measurements of the fundamental-mode Rayleigh wave from 'synthetic data' constructed for a unilateral rupture model.

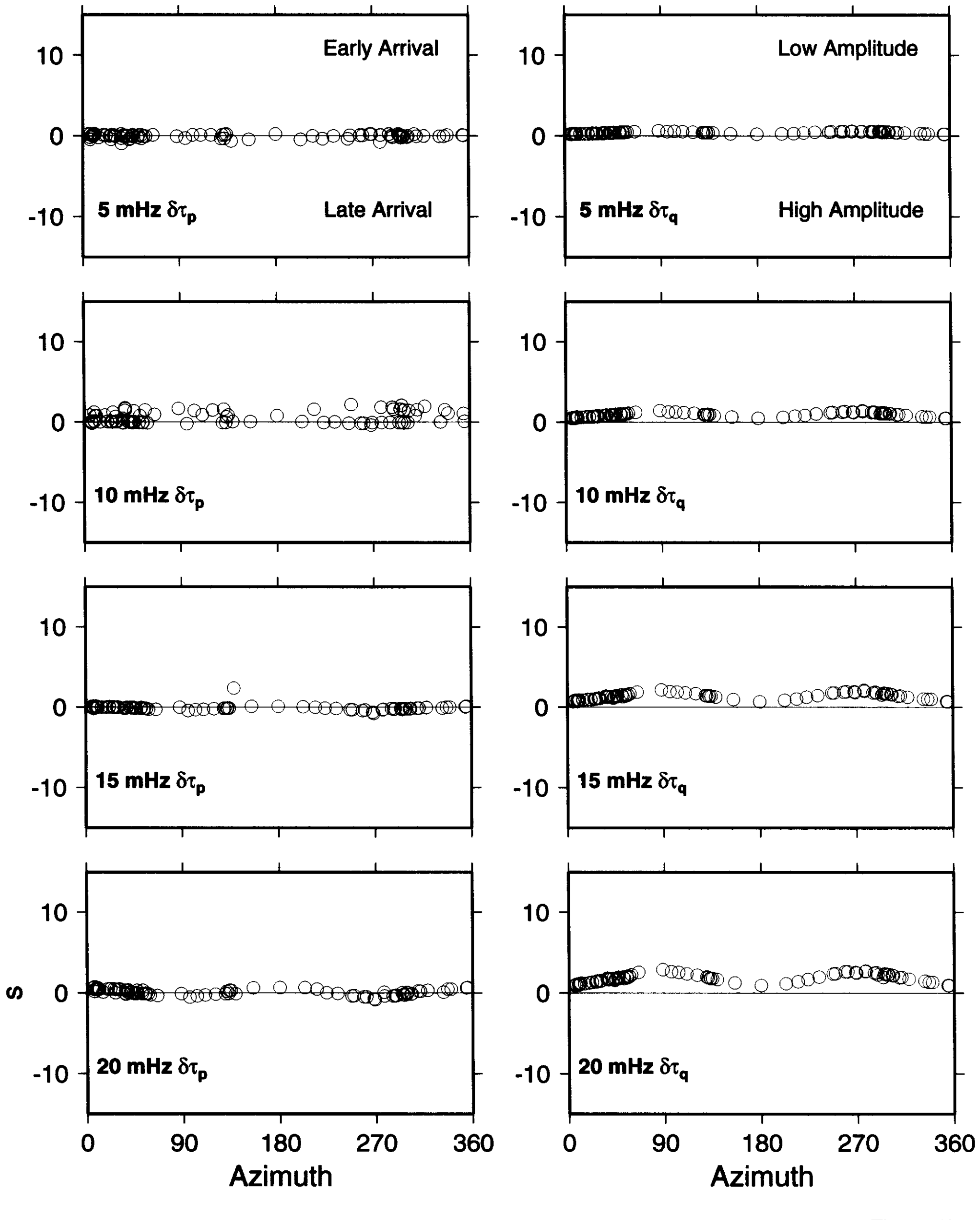

Figure 4-3: B. GSDF measurements of the fundamental-mode Rayleigh wave from 'synthetic data' constructed for a bilateral rupture model.

almost no deviation from the point-source synthetic is measured at low-frequencies, but a characteristic pattern emerges in the $\delta\tau_q$ measurements as frequency increases. For unilateral rupture (Figure 4-3A), the effects of $\hat{\boldsymbol{\mu}}^{(1,1)}$ and $\hat{\boldsymbol{\mu}}^{(2,0)}$ approximately cancel in the direction of rupture propagation, while they add constructively in the opposite direction. Thus a 'half-cosine' pattern emerges in the $\delta\tau_q(\omega)$ measurements, with the smallest data amplitudes occurring 180° away from the direction of rupture propagation. We observe this azimuthal pattern which is diagnostic of a predominately unilateral rupture for both the 1995 Jalisco and Gulf of Aqaba earthquakes, which are discussed in the results section. In the bilateral case (Figure 4-3B), $\hat{\boldsymbol{\mu}}^{(1,1)}$ is zero, so the $\hat{\boldsymbol{\mu}}^{(2,0)}$ term dominates, producing small amplitudes in both directions along the strike of the fault. For both of these examples, the finite duration of the source shifts the $\delta\tau_q$ measurements to positive values with increasing frequency, owing to spectral roll-off.

Directivity effects are often assumed to average to zero in source-time-function and source-spectrum estimation techniques if sufficent azimuthal coverage is available. The amplitude pertubations owing to finite-source effects shown in Figure 4-3 have only positive values of $\delta\tau_q$ indicating a reduction in the data amplitude relative to the point-source synthetic. While the pertubations due to the propagation of the centroid, $\partial\delta\tau_q/\partial\mu^{(1,1)}$ (Figures 4-2F and 4-2G), average to zero as a function of azimuth, the pertubations owing to $\hat{\boldsymbol{\mu}}^{(2,0)}$ do not (Figure 4-2F and 2G). The amplitude increases in the direction of rupture propagation resulting from $\hat{\boldsymbol{\mu}}^{(1,1)}$ are canceled in the unilateral case by the decreases resulting from $\hat{\boldsymbol{\mu}}^{(2,0)}$ (Figure 4-3A). In the perfectly bilateral case (Figure 4-3B), $\hat{\boldsymbol{\mu}}^{(1,1)}$=0 so only the amplitude reductions resulting from $\hat{\boldsymbol{\mu}}^{(2,0)}$ occur. Thus techniques that assume amplitude effects resulting from directivity average to zero will underestimate the earthquake's seismic moment.

4.4 Inversion Method

4.4.1 Optimization Technique

We can formulate a linear inverse problem to minimize $||\mathbf{Am} - \mathbf{b}||$ for a vector $\mathbf{m}$, which contains the 14 independent elements of $\mu^{(0,1)}$, $\boldsymbol{\mu}^{(1,0)}$, $\mu^{(0,2)}$, $\boldsymbol{\mu}^{(1,1)}$, and $\boldsymbol{\mu}^{(2,0)}$ as well as the 6 independent elements of $\mathbf{M}$. The data vector, $\mathbf{b}$, contains the GSDF measurements and $\mathbf{A}$ contains the partial derivatives calculated using equations 17-20. For sources that obey the assumption in (3), the moments of $\dot{f}(\mathbf{r}, t)$ are uniquely determined by the displacement field (Bukchin, 1995), making the linear inverse problem theoretically solvable. In practice, however, owing to errors in the assumed moment-tensor, the effects of umodelled lateral heterogeneity, and the small relative size of the minimum eigenvalue of $\boldsymbol{\mu}^{(2,0)}$, a linear least-squares inversion does not result in a robust solution. Das and Kostrov (1997) incorporated linear inequality constraints among the moments to stabilize their inversion; however, their constraints, which are based on the Hausdorff inequalities, required *a priori* information about the maximum size of the source region. The power of these constraints depended strongly on the *a priori* limits on the source region size Das and Kostrov (1997). To avoid setting *a priori* limits on the extent of the source region, we stabilized our inversion by incorporating the physical constraint that the 4 dimensional source region have non-negative volume. This constraint, which is an inherent property of all earthquakes, is equivalent to requiring the 4 x 4 matrix,

$$\begin{bmatrix} \hat{\boldsymbol{\mu}}^{(2,0)} & \hat{\boldsymbol{\mu}}^{(1,1)} \\ \hat{\boldsymbol{\mu}}^{(1,1)^{\mathrm{T}}} & \hat{\mu}^{(0,2)} \end{bmatrix}, \tag{4.22}$$

to be positive semi-definite. This constraint is non-linear in the elements of $\mathbf{m}$ and encompasses the constraints placed on the 2nd degree moments of $\dot{f}(\mathbf{r}, t)$ by other authors through the use of Bessel inequalities [Bukchin, 1995; see also Appendix B]. Methods for solving linear problems subject to matrix inequality constraints such as (21) have recently been developed in the optimization literature. We use the semidefinite programming approach of Vandenberghe and Boyd (1996). To put our problem into this form, it is necessary to restate the non-linear (least-squares) objective function as a linear objective function subject to a non-linear (quadratic) constraint. We introduce a dummy variable, c, such that $||\mathbf{Am} - \mathbf{b}|| \leq c$. Then our problem can be restated as:

$$\text{minimize} \quad \text{c}$$

$$\text{subject to} \quad \begin{bmatrix} c & \mathbf{Am} - \mathbf{b} \\ (\mathbf{Am} - \mathbf{b})^{\mathrm{T}} & \mathbf{I}^{N} \end{bmatrix} \geq 0\,, \tag{4.23}$$

$$\text{and} \quad \begin{bmatrix} \hat{\boldsymbol{\mu}}^{(2,0)} & \hat{\boldsymbol{\mu}}^{(1,1)^{\mathrm{T}}} \\ \hat{\boldsymbol{\mu}}^{(1,1)} & \hat{\mu}^{(0,2)} \end{bmatrix} \geq 0\,,$$

where $\mathbf{I}^{N}$ is the identity matrix with dimension equal to the number of GSDF measurements, N, and ≥ 0 indicates the matrix is positive semidefinite. The equivalence between the linear least-squares problem and (22) can be seen by calculating the eigenvalues of the $N+1$ by $N+1$ matrix in (22), which are non-negative when the matrix is positive semi-definite. This restatement of the problem is known as using Schur complements to represent a nonlinear constraint as linear matrix inequality (Vandenberghe and Boyd, 1996). The semi-definite programming algorithm also allows us to incorporate a variety of linear inequality constraints, such as requiring the source to lie on one of the fault planes of the moment-tensor or constraining the source to occur below the free surface, when appropriate for a particular event. The physical constraint (22) greatly reduces the non-uniqueness in the minimization problem without requiring any *a priori* information about the extent of the source.

Any difference between the assumed point source location $(\mathbf{r}_{\mathrm{S}}, t_{\mathrm{S}})$ and the true centroid location$(\mathbf{r}_{0}, t_{0})$ will result in a slight difference between the estimated value of the 2nd moments and the values of the 2nd central moments (see equation 4.8).

Correcting the estimates of the 2nd moments for a change in centroid location can violate the positive definite constraint (22). Thus we prefer to iterate the inversion (by updating the CMT parameters) until the correction term is negligible. Usually only one additional iteration is necessary for the elements of $\mathbf{m}$ corresponding to the changes in the CMT parameters to be negligible.

4.4.2 Error Analysis

We have also incorporated the non-negative volume constraint (22) into our estimates of the errors in our solution. This is important because the optimal solution to a semi-definite programming problem will often lie on the boundary of the feasible region defined by the matrix inequality constraints (Vandenberghe and Boyd, 1996). Standard linear estimates do not account for the existence of an infeasible zone, but one method that can is the grouped jacknife (Tukey, 1984). The jacknife technique relies on the assumption that different elements of a dataset are independent. In our datasets of GSDF measurements, errors in the measurements at a given station are likely to be correlated from one frequency to the next. For instance, all the arrivals at one station may be early owing to fast velocity anomalies along the path. Thus, to provide a more conservative (larger) estimate of the variance of our model, we created M subsets of data by deleting all the measurements in each of M aziumthal bins (usually 12 bands of 30°) to create the ith subset. The jackknife method then gives an estimate of the covariance matrix, $\mathbf{C}_{mm}$, of our model parameters:

$$\mathbf{C}_{mm} = \frac{1}{M-1}\sum_{i}^{M}(\hat{\mathbf{m}}_i - \hat{\mathbf{m}}_{(.)})^2 , \tag{4.24}$$

where $\hat{\mathbf{m}}_i$ is the estimate produced by the semi-definite program technique using the ith subset of the data, and $\hat{\mathbf{m}}_{(.)}$ is the average of the M values of $\hat{\mathbf{m}}_i$. The diagonal elements of $\mathbf{C}_{mm}$ give the variances of the individual model parameters.

The jacknife estimate of $\mathbf{C}_{mm}$ can also be used to determine the variances of derived quantities such as the characteristic rupture dimension, x_c, in a direction $\hat{\mathbf{n}}$.

The equation for our estimate of x_c, eq. (8), can be rewritten in vector form as:

$$x_c = 2\sqrt{\mathbf{z} \cdot \hat{\mathbf{m}}}\,, \tag{4.25}$$

where $\mathbf{z}$ is a function of $\hat{\mathbf{n}}$, and $\hat{\mathbf{m}}$ contains the elements of our estimate of $\hat{\boldsymbol{\mu}}^{(2,0)}$. Using standard error propagation equations [*Bevington and Robinson*, 1992, p. 41], we can also estimate the variance in our estimate of l_c:

$$\sigma^2_{x_c} = \sum_i \sum_j z_i z_j C_{ij} / (\mathbf{z} \cdot \hat{\mathbf{m}})\,. \tag{4.26}$$

4.5 Results

4.5.1 1995 Kobe Earthquake

The 1995, M_w 6.9, Kobe earthquake was recorded exteremely well by the Japanese strong motion network, allowing for a good comparison of our teleseismic results with more accurate estimates determined from the local data. In particular, we use it to check for biases in the 0th and 1st degree moments of $\dot{f}(\mathrm{r}, \mathrm{t})$. For this event we initially calculated synthetics using the Harvard CMT (Dziewonski *et al.*, 1996) (20:46:59.4, 34.78°N, 134.99°E, 20 km depth). We then made measurements, shown in Figure 4-4, of the fundamental mode 1st-orbit Rayleigh wave at 46 global stations for which our synthetics closely resembled the observed seismograms. The $\delta\tau_p(\omega)$ measurements showed a pattern of late arrivals at stations to the south and early arrivals at stations to the north, while the $\delta\tau_q$ measurements were essentially a flat function of azimuth indicating the data amplitudes were slightly larger than the synthetics. The lack of a clear directivity signal in the amplitude measurements is because the measurements were made at wavelengths for which an event of this size is well represented by a point-source.

Owing to the lack of a clear directivity signal in the amplitude measurements, we only inverted for changes to the first moments and moment tensor. The results of the inversion are given in Table 1 and Figure 4-5, and the fit to the data is displayed

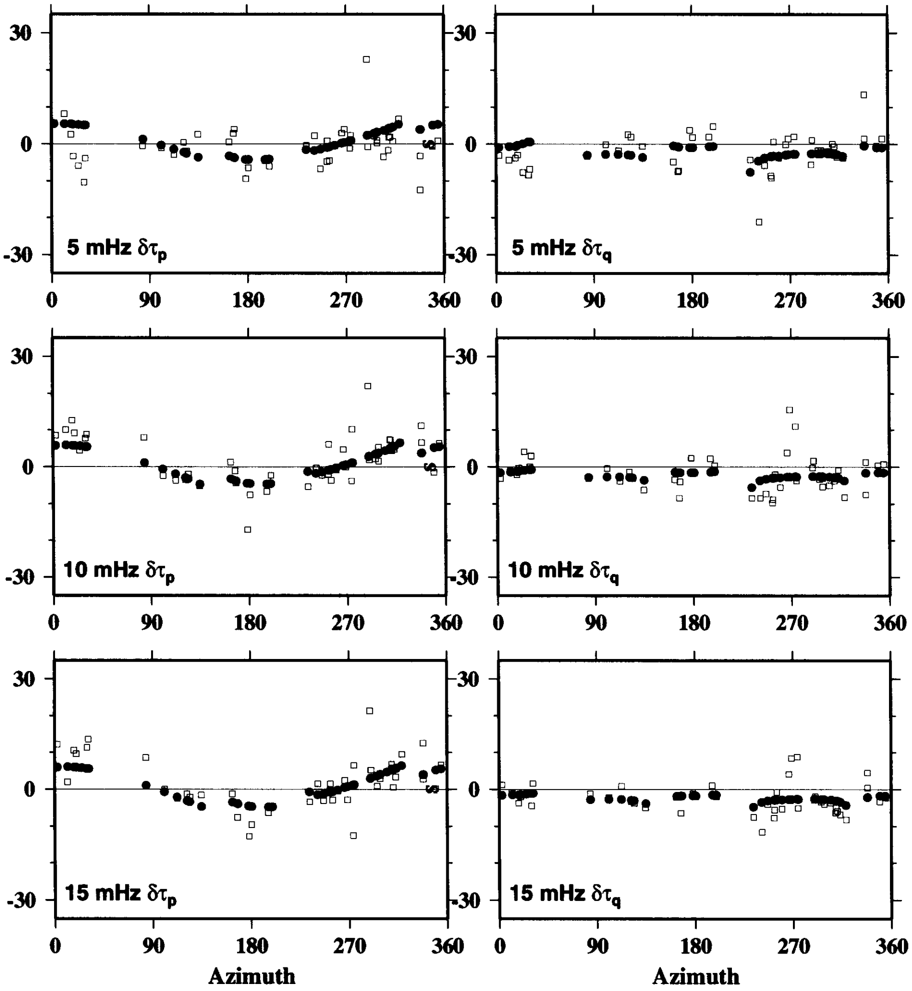

Figure 4-4: GSDF measurements (open squares) for the Harvard CMT as a function of station azimuth for the fundamental-mode, first-orbit, Rayleigh wave, for the 1995 Kobe event at global stations. Black circles denote the fit to the measurements from our inversion procedure. A value of zero indicates that no pertubation of the data relative to the synthetic was observed.

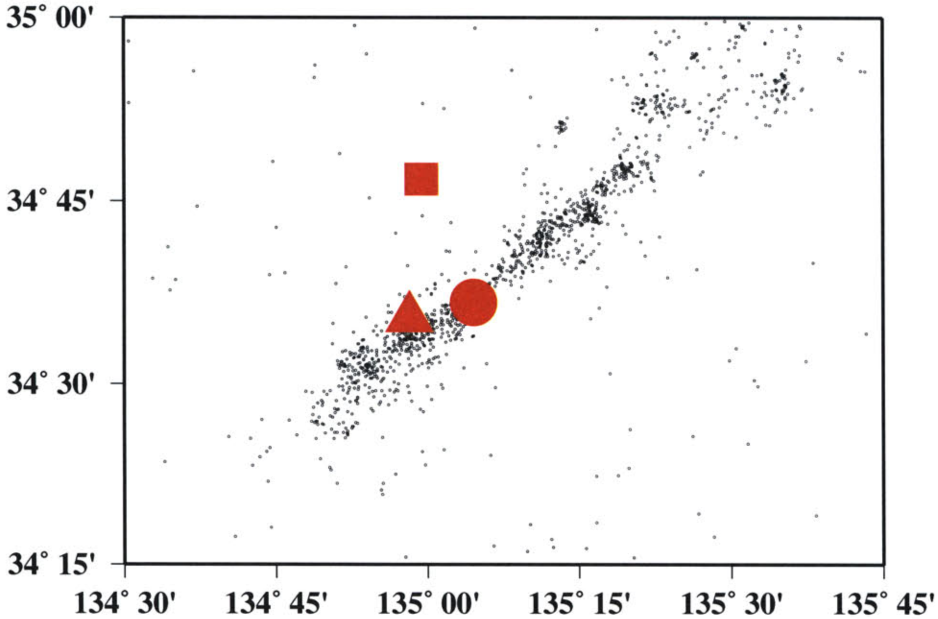

Figure 4-5: Map of the 1995 Kobe earthquake. Small black dots denote the location of aftershocks from 1/25/95 to 2/09/95 as determined by the Japanese University Group for Urgent Joint Observation of the 1995 Hyogo-ken Nanbu Earthquake. Centroid locations determined by the Harvard CMT, Ide et al, and this study are shown as the square, circle, and triangle respectively.

in Figure 4-4. The centroid location moved 24 km to the south, which fits the $\delta\tau_p$ pattern, and 5 km shallower. The changes in the moment-tensor slightly increased in the seismic moment while retaining approximately the same focal-mechanism. However, the changes to the $M_{r\theta}$ and $M_{r\phi}$ components are not well constrained. The new centroid location is about 10 km from the value determined by Ide and Takeo (1997) (34.61°N, 135.075°E, 9.2 km) using local data and provides a better estimate than the starting Harvard CMT values (Figure 4-5). We have calculated synthetic seismograms for the revised CMT and remeasured the data (Figure 4-6). The results show essentially flat functions of azimuth at a value of zero for both $\delta\tau_p$ and $\delta\tau_q$. Inversion of these remeasured data produces extremely small ($\leq\sim$ 1 km) shifts in the centroid location and correspondingly small shifts in the moment tensor, which are below our resolution limit. The residual scatter in Figure 4-6, which has an average r.m.s. amplitude of 4-7 seconds depending on frequency band, is indicative of the

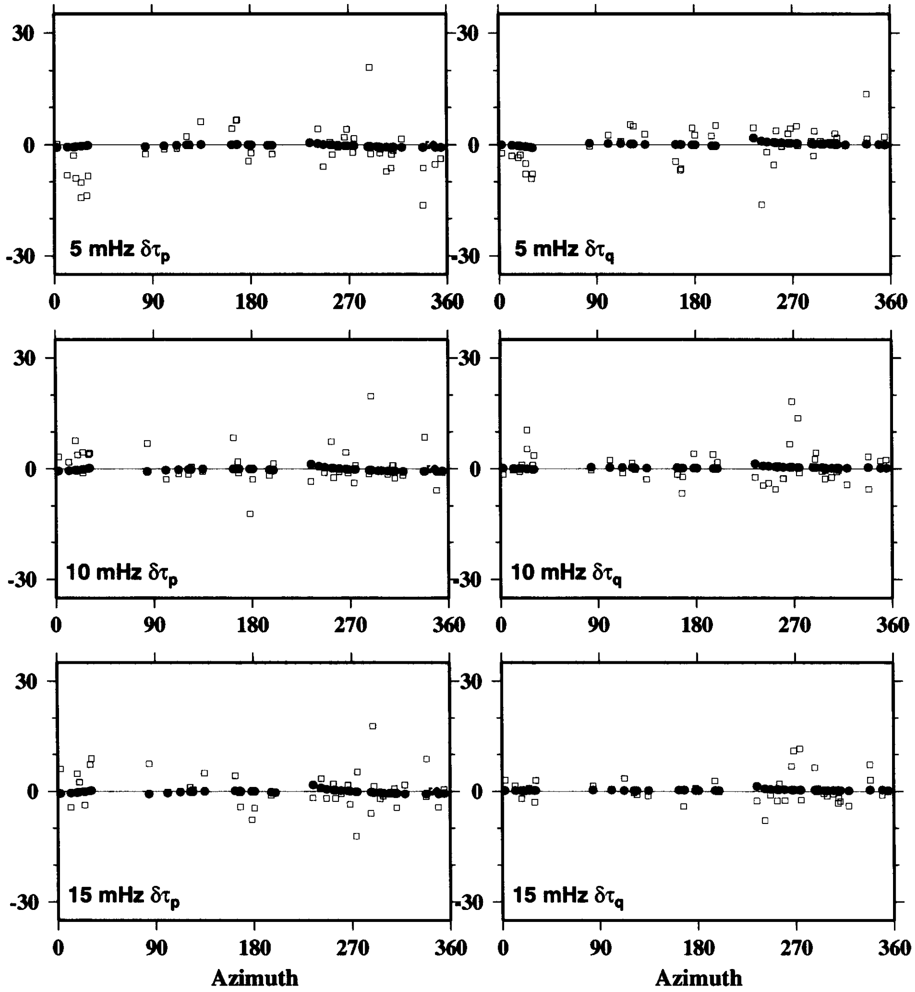

Figure 4-6: GSDF measurements (open squares) for the Kobe event using the revised centroid given in Table 1, and the fit to them (black circles) after inversion. A value of zero indicates that no pertubation of the data relative to the synthetic was observed.

amount of error in our measurements due to unmodelled propagation effects.

4.5.2 1995 Jalisco Earthquake

The 1995, M_w 8.0 Jalisco, Mexico, earthquake occurred on a shallow thrust plane from the subduction of the Rivera Plate under the North American plate (Figure 4-7). A good test of our method comes from comparing our estimate of $\hat{\mu}^{(2,0)}$ with the slip distribution determined from a local GPS study by Melbourne *et al.* (1997). We preformed an initial inversion for changes in the centroid and moment tensor. The

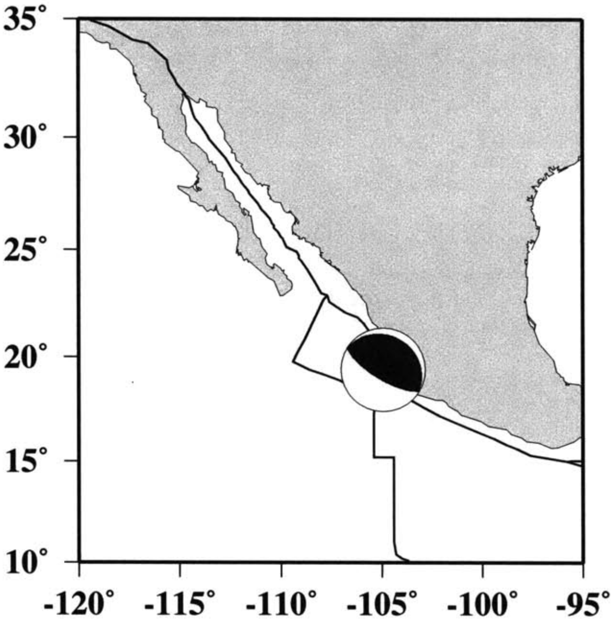

Figure 4-7: Map of the region around the 1995 Jalisco Mexico earthquake. The focal mechanism shown is for the Harvard CMT.

new centroid location (15:36:28.80, 19.43° N, 104.92° W, 8.0 km) corrected the early R1 arrivals at stations to the southeast found for the Harvard CMT (Dziewonski *et al.*, 1997). For most shallow sources, the $M_{r\theta}$ and $M_{r\phi}$ components were not well constrained, so we settled on a moment-tensor ($M_{rr} = 4.6, M_{\theta\theta} = -3.2, M_{\phi\phi} = -1.3, M_{r\theta} = 5.0, M_{r\phi} = -3.0, M_{\theta\phi} = 1.9, *10^{20}$ Nm) through a process of forward modelling. Measurements for synthetics calculated from this CMT are shown in Figure 4-8. The primary signals visible in the data are low R1 amplitudes at stations to the SE. The magnitude of these signals increases with frequency as expected for a finite source. The baseline level of the amplitude reduction times, $\delta\tau_q$, also shifts upward from about 8 s at 5 mHz to about 12 s at 10 mHz. This overall decrease in amplitude with frequency is indicative of the spectral roll-off caused by the finite duration of the source time function. We inverted the data in Figure 4-8 under the non-negative volume constraint (22) and under constraint that the characteristic length in the radial direction, $x_c(\hat{\mathbf{r}})$, be ≤ 10 km. This added constraint ensured that the source volume did not extend above the free surface.

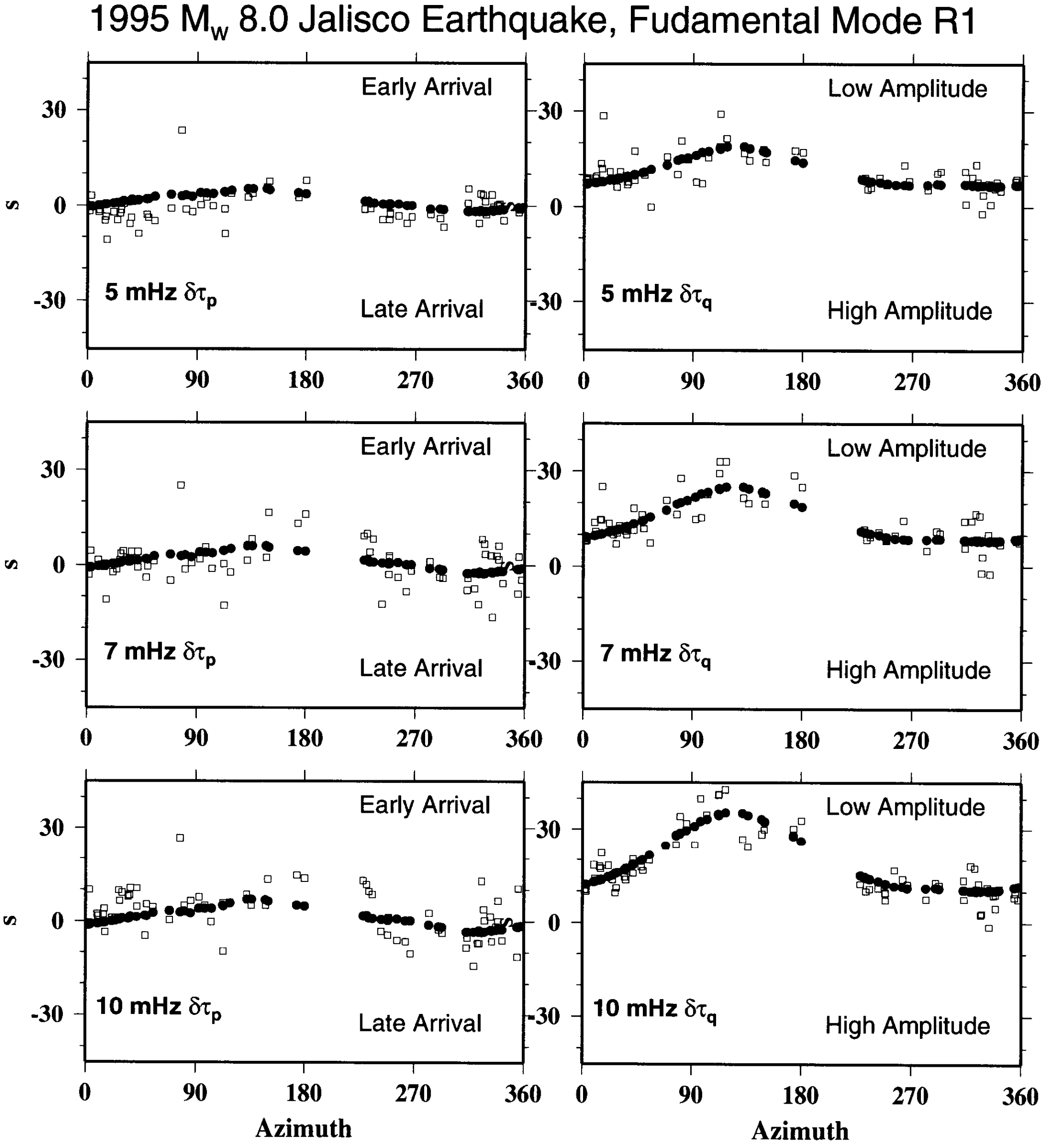

Figure 4-8: GSDF measurements (open squares) for the Jalisco event using the revised centroid given in Table 1, and the fit to them (black circles) after inversion.

Our inversion (Tables 4.1, 4.2, and 4.3) yielded a characteristic duration τ_c of 29±5 seconds, a centroid velocity $\mathbf{v}_0$ of 3.7±.5 km/s in at an azimuth of 307°, a characteristic rupture length L_c of 121±32 km along the strike of the subduction zone, a characterisitic width w_c of 76±36 km downdip, and a characteristic rupture velocity v_c of 4.1±.4 km/s. The three eigenvalues of $\hat{\boldsymbol{\mu}}^{(2,0)}$ specify the semi-axes lengths of an ellipsoid whose axes are oriented in the direction of the associated eigenvectors. This characteristic source volume shown for the Jalisco event in Figure 4-9, is an estimate of the region that contributed significantly to the moment-release. The source ellipsoid is nearly planar with its longest dimension oriented NW-SE along the strike of the subduction zone. The ellipsoid dips slightly to the NE as expected for a shallow thrust plane. Figure 4-10 compares our estimate of the characteristic source dimensions (blue ellipse) to the GPS slip inversion of Melbourne *et al.* (1997). Our centroid location agrees well with the value calculated from the slip distribution and the Harvard CMT. The NEIC epicenter is displaced about 80-100 km to the SE. The position of the centroid relative to the epicenter agrees with the direction of the characteristic velocity. We calculated the characteristic dimensions for Melbourne et al.'s distribution (red ellipse in Figure 4-10), which was confined to a single plane (strike 302°, dip=16°). Its larger dimension is along strike, L_c =91 km, and its smaller dimension is oriented downdip, $w_c = 50$ km. Thus, our estimate of $\hat{\boldsymbol{\mu}}^{(2,0)}$ is consistent with the local inversion.

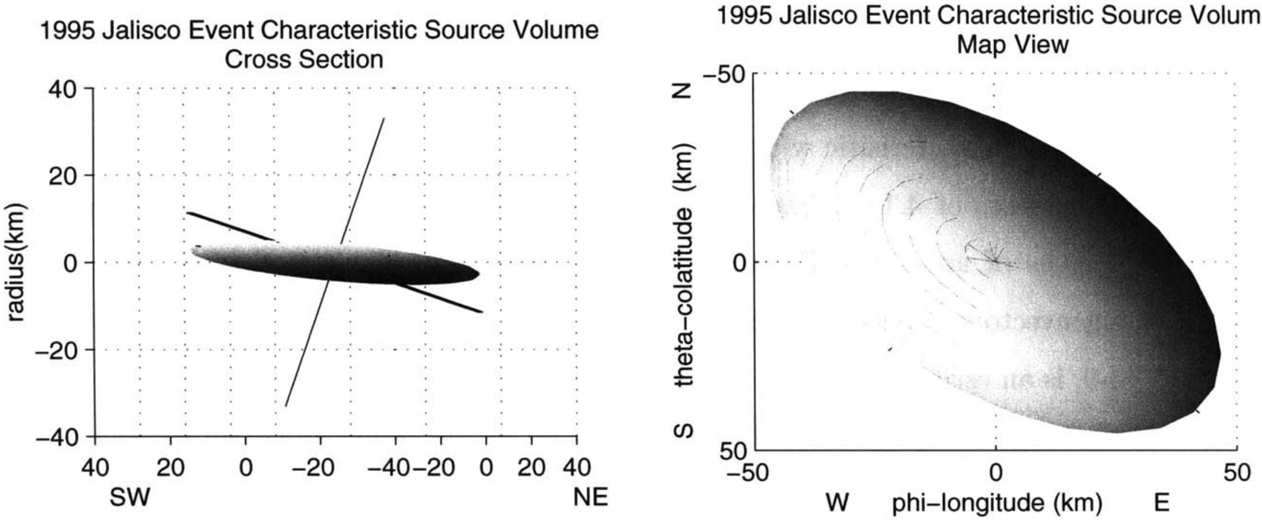

Figure 4-9: Plots of the characteristic source volume of the Jalisco event defined by $\boldsymbol{\mu}^{(2,0)}$. Shading indicates deeper depths. A) Cross-sectional view. Planes show the fault-planes of the event's moment-tensor B) Map view.

Table 4.1: 1st moments inversion results

earthquake	$\mu^{(0,1)}$		$\underline{\mu}^{(1,0)}$	
	time	lat.	lon.	dep.
Kobe	20:47:00.0±1.2	34.59±.06°N	134.97±08°E	15.2±5.2
Jalisco	15:36:30.5±.4	19.48±.03°N	105.02±.03°W	14.4±2.6
Aqaba	04:15:27.2±.1	29.03±.02°N	34.60±.01°W	16.4±1.0
Antarctica	03:13:01.6±.7	-62.74±.03°N	148.01±.06°E	11.3±2.4

Depths are in km, errors are ±2 standard deviations.

To resolve the fault-plane ambiquity for the Jalisco focal mechanism (Figure 4-7) we calculated the characteristic rupture length in the direction normal to each of the candidate fault planes. For the shallowly dipping plane (strike=302°, dip=19°), $x_c(\hat{\mathbf{n}}) = 21 \pm 6$ km and for the steeply dipping plane $x_c(\hat{\mathbf{n}}) = 76 \pm 32$ km. The shallowly dipping plane has a much smaller value of $x_c(\hat{\mathbf{n}})$, and we therefore infer that it is the true rupture plane. This agrees with Melbourne et al's study using local data. The small value of $x_c(\hat{\mathbf{n}})$ is due to the dip of the characteristic source-volume to the northeast. This dip is a robust feature of the inversion. Figure 4-11 shows histograms for each element of the 1st and 2nd moments for the 12 different inversions

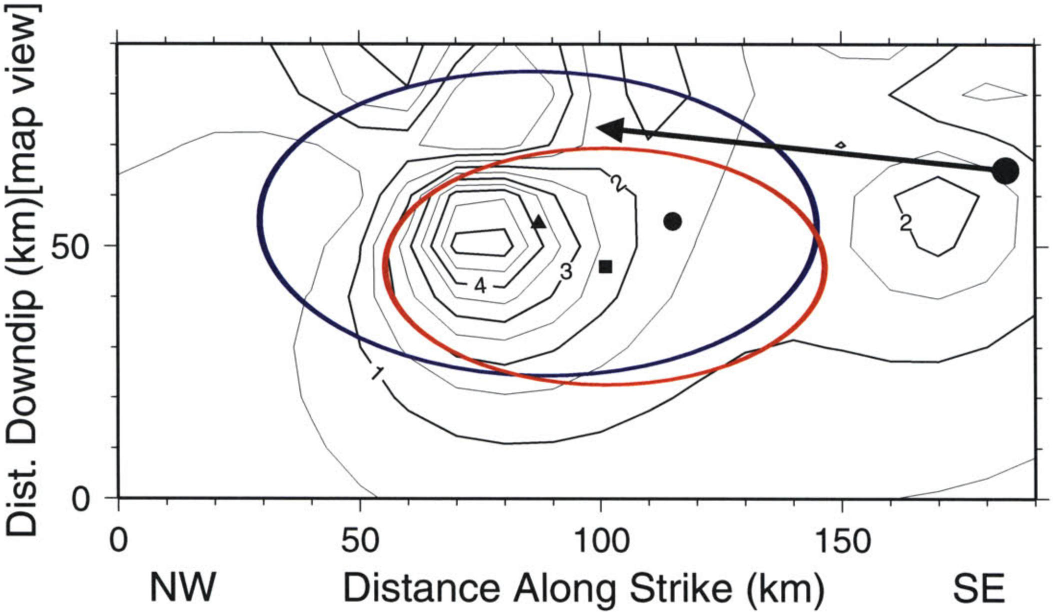

Figure 4-10: Contours of slip (m) for the Jalisco event taken from Melbourne et al. [1997]. Centroid locations are shown for the Harvard CMT (small circle), Melbourne et al (black square), and this study (black triangle). Characteristic source ellipses are shown for this study (blue) and for the Melbourne et al slip distribution (red). The large circle is the PDE epicenter and the arrow represents the direction of the characteristic velocity.

Table 4.2: 2nd moments inversion results

earthquake	$\hat{\mu}^{(0,2)}$		$\underline{\hat{\mu}}^{(1,1)}$	
		r	θ	ϕ
Jalisco	214±217	0±89	-474±195	-621±149
Aqaba	21±17	6±6	-133±27	-15±25
Antarctica	570±173	-150±256	-278±668	-2048±628

All values have been normalized by the moment of the event, the units of $\hat{\mu}^{(0,2)}$ are s^2, $\underline{\hat{\mu}}^{(1,1)}$ are km s. r is the radial direction, θ is co-latitude, and ϕ is longitude. Errors are ±1 standard deviation.

Table 4.3: 2nd moments inversion results

	$\underline{\underline{\hat{\mu}}}^{(2,0)}$					
	rr	rθ	rϕ	$\theta\theta$	$\theta\phi$	$\phi\phi$
Jalisco	24±9	56±158	-138±233	2483±1390	1116±1101	2625±1300
Aqaba	23±32	29±41	-40±65	1040±458	-11±332	74±219
Antarctica	49±10	42±520	568±654	1624±2178	184±230	7834±4176

The units of $\underline{\underline{\hat{\mu}}}^{(2,0)}$ are km^2. Errors are ±1 standard deviation.

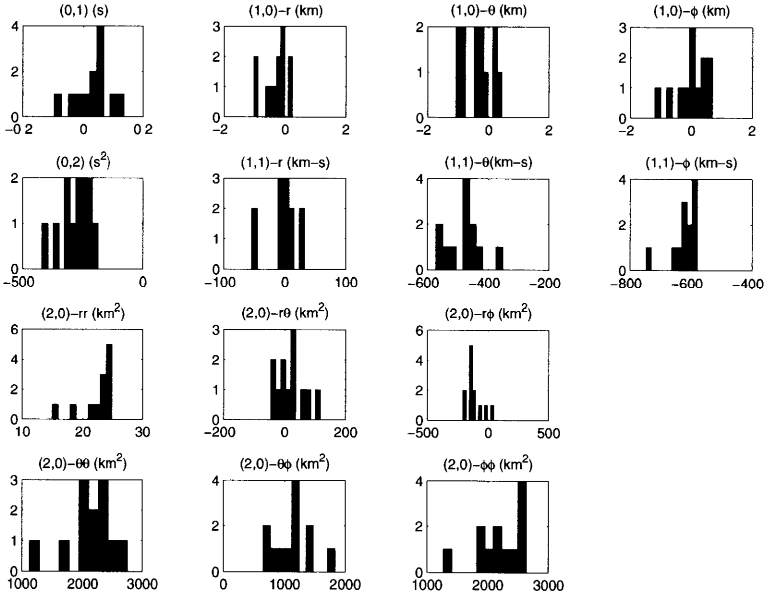

Figure 4-11: Histograms of the values of the Jalisco event's 1st and 2nd moments determined from the Jacknife error test. 68 inversions were run, with each inversion corresponding to a subset of data where all the measurements for one of the 68 stations had been deleted.

done for the jacknife calculation (corresponding to deleting each of the 12 30° azimuth bins from the full dataset). In general, the distributions are peaked near the value for the full dataset with a relatively small range of values. The positive values of $\mu_{r\theta}^{(2,0)}$ (most trials) and the negative values of $\mu_{r\phi}^{(2,0)}$ (11 of 12 trials) both correspond to a source volume that dips to the NE. The characteristic volume has a dip of about 7° to the NE, while the moment-tensor (19°) and the fault plane determined from the local network (17°) have slightly steeper values. Thus, even for this shallow-thrust event, it is possible to recover the approximate dip direction from the second moments.

4.5.3 1995 Gulf of Aqaba Earthquake

The 1995, M_w7.2, Gulf of Aqaba Earthquake ruptured the southern extension of the Dead Sea Transform (Figure 4-12A). First-orbit Rayleigh waves at low frequencies ($\leq$ 10 mHz), measured using synthetics computed for the Harvard CMT, showed no systematic signal in either $\delta\tau_p$ or $\delta\tau_q$. However, higher frequency measurements of teleseismic P waves did display systematically small amplitudes at stations to the south of the event (Figure 4-13). We inverted measurements of $\delta\tau_p$ and $\delta\tau_q$ for the P waves at 25, 30, 35, and 40 mHz for the 1st and 2nd moments and the moment tensor elements. The characteristic dimension in the radial direction was constrained to be less than the CMT centroid depth of 18km. The results of our inversion (Tables 4.1, 4.2, and 4.3) correspond to a characteristic duration, τ_c, of 9±1 s, a centroid velocity, $\mathbf{v}_0$, of 6.4±1.7 km/s in the direction N06°W, a characteristic rupture length, L_c, of 65±14 km in the direction N02°E. The changes in the moment tensor elements have about the same effect on the synthetic seismograms as keeping the same focal mechanism but increasing the total moment of the event from .72 x10^{20} to 1.2 x10^{20} Nm. (This increase in total moment may result from our use of the PREM crustal structure rather than some more appropriate local velocity model.) The large magnitude of $\mathbf{v}_0$ is most likely due to the low value of the 2nd temporal moment.

The characteristic rupture volume corresponding to our values of $\hat{\mu}^{(2,0)}$ is shown in map view in Figure 4-12B. One fault-plane of the moment-tensor strikes NNE-

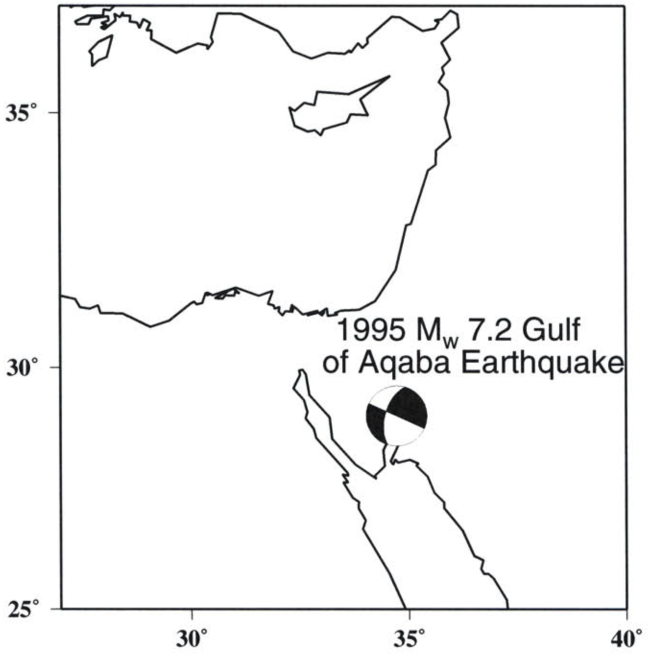

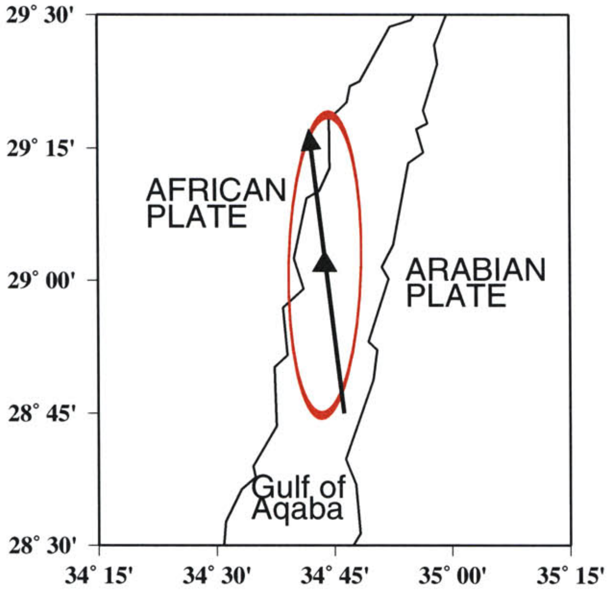

Figure 4-12: (Top) Map of the Eastern Mediterannien region showing the location and mechanism of the 1995 Aqaba earthquake. (Bottom) Map view of the source region of the Aqaba earthquake. The triangle shows the centroid location given in Table 1. The arrow represents the characteristic velocity vector, scaled to a length equal to the product of τ_c and v_c. The red ellipse is the map view projection of the characteristic source volume corresponding to the values of $\hat{\boldsymbol{\mu}}^{(2,0)}$ in Table 1.

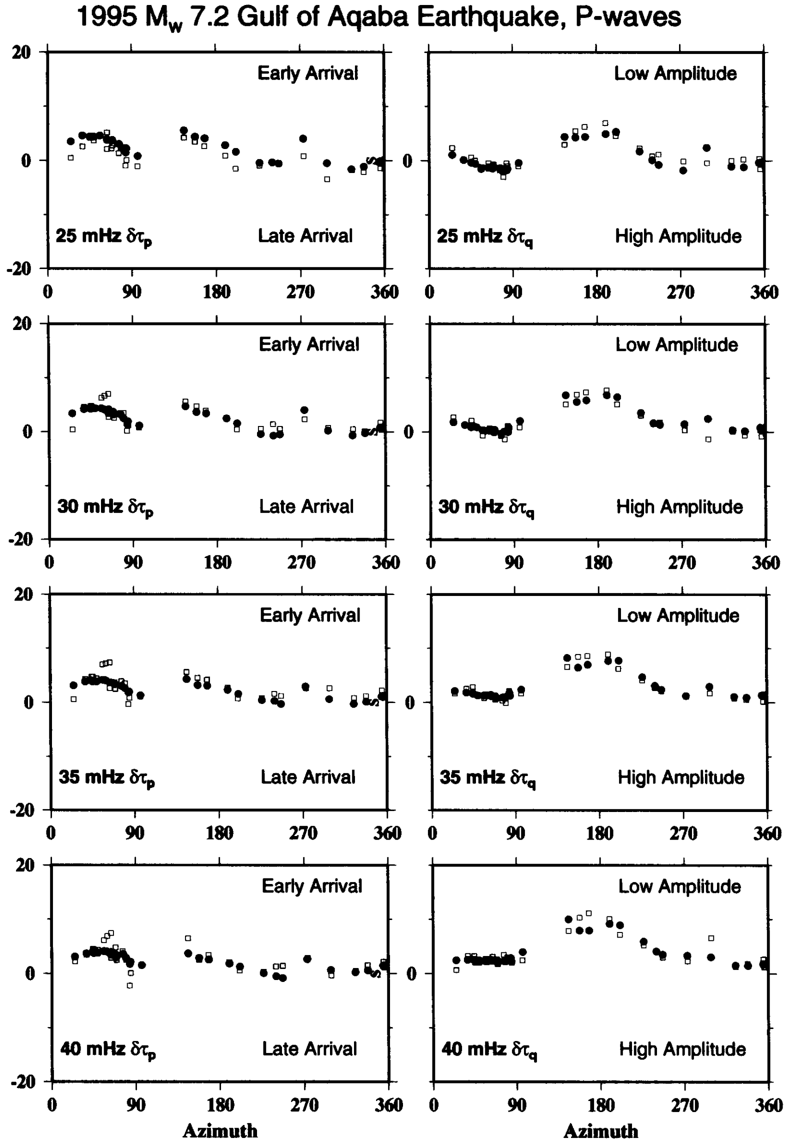

Figure 4-13: GSDF measurements (open squares) of the P-wave at global stations for the Aqaba event. Black circles show the fit to the measurements after inversion.

SSW while the other strikes WNW-ESE. The NNE striking plane has a value of $x_c(\hat{\mathbf{n}}) = 26 \pm 15$ km while the ESE striking plane has a value of $x_c(\hat{\mathbf{n}}) = 59 \pm 16$ km. Thus, we prefer the NNE striking plane as the true rupture plane. This fault-plane is consistent with the orientation of the Dead-Sea Transform in this region. The small difference in the azimuth of the characteristic rupture length, 002°, from the strike of the fault-plane of the moment-tensor, 019°, may be related to this event rupturing more than one fault. Pinar and Turkelli (1990) and Klinger *et al.* (1999) showed that this event's rupture jumped north across a series of faults in the Dead Sea Transform system. This jump would cause a difference between the azimuth of the fault-plane in the focal mechanism and the azimuth of the characteristic rupture volume of the sense we determine, but the difference may also be a result of the limited station coverage in southern azimuths.

4.5.4 1998 Antarctic Earthquake

The March 25, 1998, M_w 8.2, Antarctic event involved faulting over a large region, but the lack of nearby seismic stations makes it difficult to determine the details of this event's space time rupture history. We measured $\delta\tau_p^n$ and $\delta\tau_q^n$ for fundamental mode 1st orbit Rayleigh waves (Figure 4-14) from vertical component recordings at the set of global stations shown in Figure 4-15. The measurements show a strong signal of low Rayleigh wave amplitudes (positive values of $\delta\tau_q^n$) at stations to the east, suggesting that even at these low frequencies a point source representation does not adequately model this event.

Inversion of the GSDF data shown in Figure 4-14 resulted in the centroid and second moment estimates shown in Tables 4.1, 4.2, and 4.3. The values in Table 4.2 correspond to a τ_c of 48±2 s and a $\mathbf{v}_0$ of 3.6±.1 km/s nearly due west. This value of τ_c agrees well with a value of 48 ± 10 s determined from fitting a synchronous source model to the total-moment spectrum of this event determined with the technique of Silver and Jordan (1983) (Figure 4-16). The source ellipsoid (Figure 4-15), derived from $\hat{\boldsymbol{\mu}}^{(2,0)}$, has a L_c of approximately 178±46 km in the east-west direction, and a x_c of approximately 80±53 km in the north-south direction. The fit to the GSDF

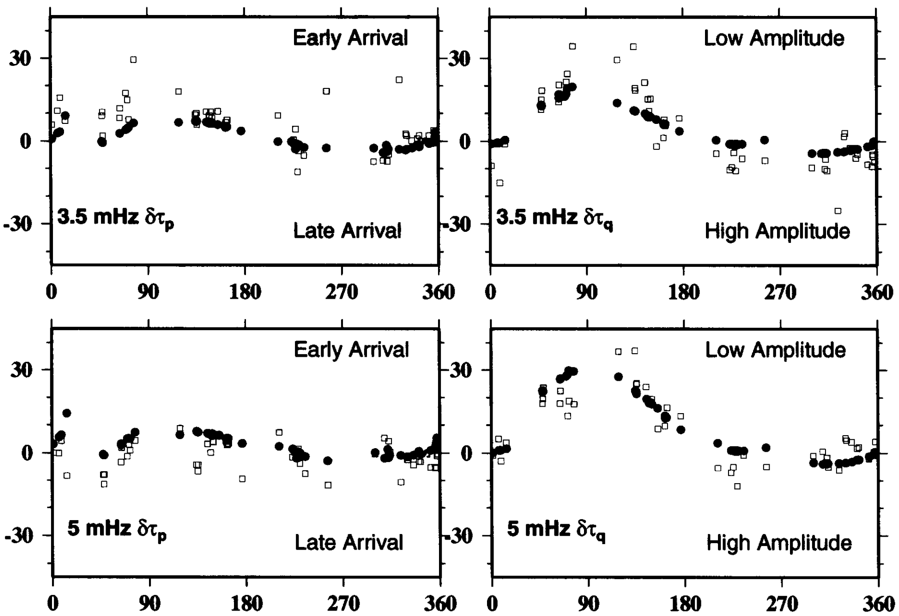

Figure 4-14: GSDF measurements (open squares) for the Antarctic earthquake of the fundamental mode Rayleigh wave at 3 and 5 mHz for the stations shown in Figure 4-15A. Azimuth values are in degrees from North. Solid circles denote the fit to these measurements for the estimates of the 1st and 2nd degree moments produced by our inversion procedure.

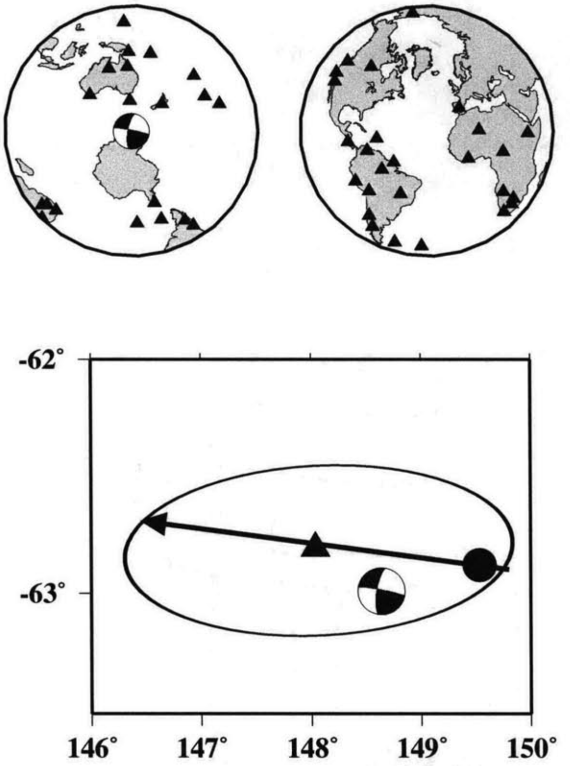

Figure 4-15: (Top) Lambert projections centered on the Harvard centroid location showing that focal mechanism and the 52 seismic stations (triangles) used in this study. (Bottom) Map of the Antarctic event's source region. The Harvard centroid location (focal mechanism), the PDE epicenter (circle) and our estimate of the centroid location (triangle) are shown. The ellipse is the surface projection of the source ellipsoid defined by $\hat{\boldsymbol{\mu}}^{(2,0)}$, and the arrow represents the direction of the instantaneous centroid velocity given by $\hat{\boldsymbol{\mu}}^{(1,1)}$ which has been scaled to a length corresponding to the product of this velocity and the characteristic duration.

data (Figure 4-14) is very good, with most of the residual scatter probably resulting from the effects of unmodeled lateral heterogeneity. The slight shift in centroid is the dominant effect in fitting the $\delta\tau_p$ measurements, while the combination of the westward directivity, $\hat{\boldsymbol{\mu}}^{(1,1)}$, and the large east-west extent of the source volume, $\hat{\boldsymbol{\mu}}^{(2,0)}$, produce the fit to the $\delta\tau_q$ measurements.

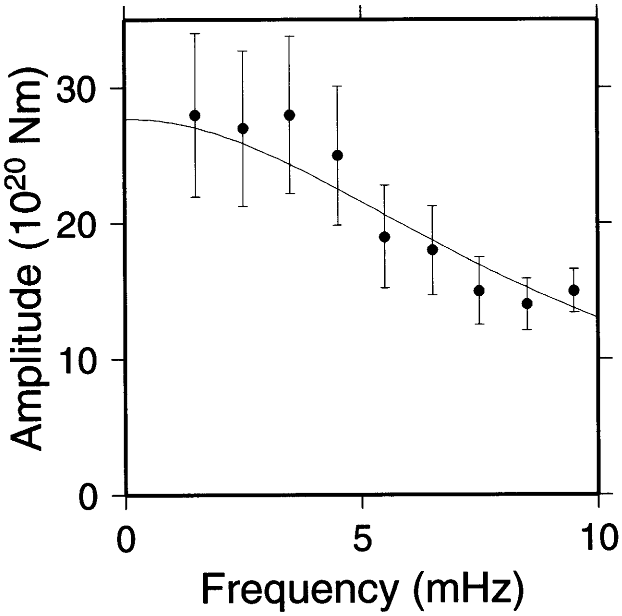

Figure 4-16: Amplitude spectra of the source time function. Points with 1-σ error bars are network averages of free oscillation data. Solid line corresponds to fitting the function $\mathrm{M_T}(\omega) = \mathrm{M_T^0}(1 + \frac{\omega^2\tau_c^2}{8})^{-1}$ to the spectra. The best fitting values for the characteristic duration, τ_c, and total moment, $\mathrm{M_T^0}$, are 48 ± 10 s and 2.8 ±.3 x10^{21} N-m

The most robustly determined properties of the Antarctic event are the strong westward propagation of the instantaneous centroid and the large east-west extent of the rupture. The similarity in magnitude of $\boldsymbol{v}_0$, 3.6±.1 km/s, and v_c, 3.7±.1 km/s, is consistent with a nearly unilateral westward rupture but may allow for small amounts of slip to the east of the epicenter. The orientation of the source ellipsoid and the azimuth of the instantaneous centroid velocity are consistent with each other and favor rupture on the east-west oriented fault plane of the Harvard moment tensor.

4.6 Discussion

We have developed an inversion procedure that can estimate the 1st and 2nd degree moments of earthquake source distributions without any *a priori* constraints on the orientation or extent of the source. The 2nd moments are a desirable quantity to determine because they are independent of the types of parameterizations and smoothing operations typically employed in teleseismic finite-fault inversions, and they can be used as integral constraints in determining the space-time history of rupture. The technique presented in this paper can be applied to any seismic phase for which an isolation filter can be constructed. Future studies will take advantage of the different samplings of the source provided by using measurements from a variety of phases/components. Our estimates of the 1st and 2nd moments agree well with values derived from slip inversions using local data for both the Kobe and Jalisco events. Additionally, the Jalisco, Aqaba, and Antarcitc events demonstrate the ability of the technique to resolve the fault-plane ambiguity.

While regions such as Mexico and Japan have extensive local networks which allow detailed study of their earthquakes, there are many interesting events which do not have sufficient local data-sets. For instance, the 1998, M_w 8.2, Antarctic earthquake occurred over 1000 km from the nearest seismometer. In addition to being able to resolve the fault-plane ambiquity for this event, our estimates of the centroid and rupture length, L_c, were used by Toda and Stein (1999) to calculate the change in Coulomb failure stress at the locations of this events' aftershocks. In the future, we hope to utilize 2nd moments to help constrain the details of slip distributions from teleseismic data. The moments can be used as integral constraints to help regularize teleseismic finite-fault inversions without requiring arbitrary choices of damping parameters. We expect future studies of 2nd moments using the technique developed in this paper to be useful in a wide range of earthquake source, seismotectonic, and plate-motion studies.

4.7 Acknowledgments

We thank Satoshi Ide for providing us with the centroid of his slip distribution for the Kobe event, and Tim Melbourne for providing his slip distribution for the Jalisco event. Figures in this paper were generated using the GMT software freely distributed by Wessel and Smith (1991). This research was sponsored by the National Science Foundation under grant EAR-9805202.

Chapter 5

Resolution of the Fault-Plane Ambiquity Using 2nd degree Moments

Abstract

The point-source representation of an earthquake is commonly used in global seismology to estimate an event's size, location, and faulting type. However, for large earthquakes, there is information on the spatial and temporal distribution of slip during the rupture contained in the low-frequency seismic wavefield. We use the anomalies in the wavefield caused by the finite extent of the source to determine the 2nd degree polynomial moments of the moment-release distribution. These quantities describe the extent, orientation, duration, and directivity of the rupture. The estimates of the 2nd spatial moment were used to resolve the fault-plane ambiguity for a catalog of large earthquakes. In all cases that could be verified with local data, the correct rupture plane was identified. Additionally, the 2nd moments show that all of the events studied were predominantly unilateral ruptures.

5.1 Introduction

Earthquake faults range in size from a few meters for the smallest events to 10s of kilometers for moderate (M 6-7) events to hundreds of kilometers for the largest (M>8) events. Owing to the low density of seismometers on a global scale, it is common to study earthquakes using data recorded thousands of km away from the faulting region. At these distances, the seismic wavefield has its highest signal to noise ratios at periods between about 10 and 500 s. This frequency range corresponds to wavelengths (50-5000 km) that are much longer than the source dimensions of moderate to large events. This has led to the wide-spread use in global seismology of a point-source approximation for an earthquake. Most commonly, an earthquake with some finite extent in space and time that is specified by the stress-glut rate tensor $\dot{\mathbf{\Gamma}}(\mathbf{r}, t)$ (Backus and Mulcahy, 1976a,b) is approximated by a point source specified by a moment tensor, $\hat{\mathbf{M}}$, a centroid location, $\mathbf{r}_0$, centroid time, t_0:

$$\dot{\mathbf{\Gamma}}(\mathbf{r}, t) \approx \mathbf{M}\delta(\mathbf{r} - \mathbf{r}_0)\delta(t - t_0). \tag{5.1}$$

Assuming a constant moment-tensor during the rupture, $\dot{\mathbf{\Gamma}}(\mathbf{r}, t) = \hat{\mathbf{M}}\ \dot{f}(\mathbf{r}, t)$, allows for the definition of the centroid location and centroid time in terms of the 1st degree polynomial moments of the scalar space-time function $\dot{f}(\mathbf{r}, t)$.

$$\mathbf{r}_0 = \boldsymbol{\mu}^{(1,0)}/M_0, \quad \boldsymbol{\mu}^{(1,0)} = \iint \dot{f}(\mathbf{r}, t)\ \mathbf{r}\, dV\, dt \tag{5.2}$$

$$t_0 = \mu^{(0,1)}/M_0, \quad \mu^{(0,1)} = \iint \dot{f}(\mathbf{r}, t)\, t\, dV\, dt\,. \tag{5.3}$$

where M_0 (the seismic moment), $\boldsymbol{\mu}^{(1,0)}$, and $\mu^{(0,1)}$ are the 0th, 1st spatial, and 1st temporal moments of $\dot{f}(\mathbf{r}, t)$, and the integrals are taken over the entire source volume and source duration.

In this point-source representation, all of the information about the orientation of the fault is contained in **M**. Considering the double-couple portion of **M** results in the well-known fault-plane ambiguity, where slip on either of the two orthogonal nodal-planes specified by **M** produce identical seismic-wavefields. While **M** and its corresponding best double-couple focal-mechanism are routinely determined from global recordings of the teleseismic wavefield radiated by earthquakes, resolving the fault-plane ambiguity has generally required additional information such as aftershock locations or near-field seismic and geodetic data. A variety of techniques for determining representations of $\dot{\mathbf{\Gamma}}(\mathbf{r}, t)$ that contain more detail than the point-source representation have been developed (for a review see Beroza (1995)). Many of the existing techniques can determine the temporal history of moment release, $\dot{f}(t)$ (the source-time-function), in some frequency band (see Tanioka and Ruff (1997) or Ihmlé and Jordan (1995)). However, the spatial distribution of moment-release is difficult to obtain for all but the largest earthquakes. The most commonly used technique, developed by Kikuchi and Kanamori (1991), represents the source as a few point source subevents and determines the best location for each point-source. This technique has been widely used to determine an overall sense of the direction of rupture propagation. However, because teleseismic body-waves cannot necessarily differentiate between a widely distributed rupture and one composed of compact subevents (Ihmlé, 1998), the projection of $\dot{\mathbf{\Gamma}}(\mathbf{r}, t)$ onto a basis set comprised of a few point-sources is difficult to interpret physically. In particular, quantities like rupture length, rupture velocity, and stress drop are difficult to determine from this representation. Additionally, when the rupture propagates along the intermediate axis of the event's focal mechanism, there is no way to resolve the fault-plane ambiguity from this representation. In this Chapter, we present an earthquake catalog that includes well defined physical quantities which describe the spatial and temporal extent of a rupture and can be used to systematically resolve the fault-plane ambiguity.

5.1.1 Second degree moments

The zeroth and first degree moments that make up a point-source representation are just the corresponding coefficients in a Taylor series expansion relating the seismogram resulting from a point source, $\tilde{s}(\mathbf{r}_\mathrm{R}, \mathbf{r}_\mathrm{S}, t_\mathrm{S}, \omega)$, to the seismogram resulting from a source with finite extent in space and time, $s(\mathbf{r}_\mathrm{R}, \dot{\mathbf{\Gamma}}(\mathbf{r}, t), \omega)$

$$s(\mathbf{r}_\mathrm{R}, \dot{\mathbf{\Gamma}}(\mathbf{r}, t), \omega) = \frac{1}{M_0}[M_0 + i\omega\mu^{(0,1)} + \boldsymbol{\mu}^{(1,0)} \cdot \boldsymbol{\nabla}_\mathrm{S} - \frac{\omega^2}{2}\mu^{(0,2)} + i\omega\boldsymbol{\mu}^{(1,1)} \cdot \boldsymbol{\nabla}_\mathrm{S} + \frac{1}{2}\boldsymbol{\mu}^{(2,0)} : \boldsymbol{\nabla}_\mathrm{S}\boldsymbol{\nabla}_\mathrm{S} + ...]\tilde{s}(\mathbf{r}_\mathrm{R}, \mathbf{r}_\mathrm{S}, t_\mathrm{S}, \omega)\,. \quad (5.4)$$

Here the point-source location, $\mathbf{r}_\mathrm{S}$, and time, t_S correspond to the origin of the coordinate system in (5.2) and (5.3). The 2nd degree moments, $\hat{\boldsymbol{\mu}}^{(2,0)}$, $\hat{\mu}^{(0,2)}$, and $\hat{\boldsymbol{\mu}}^{(1,1)}$, describe the spatial extent, duration, and average propagation of the rupture.

$$\hat{\boldsymbol{\mu}}^{(2,0)} = \begin{bmatrix} \hat{\mu}_{rr} & \hat{\mu}_{r\theta} & \hat{\mu}_{r\phi} \\ \hat{\mu}_{r\theta} & \hat{\mu}_{\theta\theta} & \hat{\mu}_{\theta\phi} \\ \hat{\mu}_{r\phi} & \hat{\mu}_{\theta\phi} & \hat{\mu}_{\phi\phi} \end{bmatrix} = \iint \dot{f}(\mathbf{r}, t)\,(\mathbf{r} - \mathbf{r}_0)(\mathbf{r} - \mathbf{r}_0)^\mathrm{T}\,dV\,dt\,, \quad (5.5)$$

$$\hat{\mu}^{(0,2)} = \iint \dot{f}(\mathbf{r}, t)\,(t - t_0)^2\,dV\,dt, \qquad \hat{\boldsymbol{\mu}}^{(1,1)} = \iint \dot{f}(\mathbf{r}, t)\,(\mathbf{r} - \mathbf{r}_0)\,(t - t_0)\,dV\,dt\,. \quad (5.6)$$

where the $\hat{\mu}$ notation indicates central moments.

Following Backus (1977a) and Silver and Jordan (1983), we can define the characteristic dimension, $x_c(\hat{\mathbf{n}})$, of the source region in a direction $\hat{\mathbf{n}}$, the characteristic duration τ_c, the characteristic length L_c, the characteristic (or apparent rupture) velocity v_c, and the average velocity of the instantaneous spatial centroid, $\mathbf{v}_0$:

$$x_c(\hat{\mathbf{n}}) = 2\sqrt{\hat{\mathbf{n}}^\mathrm{T}\left[\hat{\boldsymbol{\mu}}^{(2,0)}/M_0\right]\hat{\mathbf{n}}}\,, \quad \tau_c = 2\sqrt{\hat{\mu}^{(0,2)}/M_0}\,, \quad v_c = L_c/\tau_c\,, \quad \mathbf{v}_0 = \hat{\boldsymbol{\mu}}^{(1,1)}/\hat{\mu}^{(0,2)}. \quad (5.7)$$

$x_c(\hat{\mathbf{n}})$ has its maximum value, L_c, when $\hat{\mathbf{n}}$ corresponds to the eigenvector associated with the largest eigenvalue of $\hat{\boldsymbol{\mu}}^{(2,0)}$. The characteristic width, W_c corresponds to the value of x_c along the direction of the eigenvector associated with the 2nd largest eigenvalue of $\hat{\boldsymbol{\mu}}^{(2,0)}$. Owing to the weighted average nature of the 2nd moments, the characteristic dimensions of a rupture are always smaller than its total dimensions. However, they provide an estimate of the region that contributed significantly to the moment-release.

5.2 Resolving the fault-plane ambiguity using Second moments

For a perfectly planar fault, the smallest eigenvalue of $\hat{\boldsymbol{\mu}}^{(2,0)}$ is identically zero because the rupture zone has no extent in the direction normal to the fault plane. Additionally for a perfectly planar fault, the vector that specifies the average direction of rupture propagation, $\hat{\boldsymbol{\mu}}^{(1,1)}$, will lie within the fault-plane. These two geometrical properties allow for the resolution of the fault-plane ambiguity given estimates of $\hat{\boldsymbol{\mu}}^{(2,0)}$ and $\hat{\boldsymbol{\mu}}^{(1,1)}$. While knowledge of $\hat{\boldsymbol{\mu}}^{(2,0)}$ will resolve the fault-plane ambiguity for any source distribution that has finite extent in two perpendicular directions (i.e. not a line or point source), knowledge of $\hat{\boldsymbol{\mu}}^{(1,1)}$ does not ensure this ability for a general planar source. For instance, the instantaneous centroid of a perfectly symetrical bi-lateral rupture has a constant position as a function of time during rupture (the epicenter/centroid). Hence, $\hat{\boldsymbol{\mu}}^{(1,1)}$ is identically the zero vector in this case and contains no information about the orientation of the rupture. A more common geometry for which $\hat{\boldsymbol{\mu}}^{(1,1)}$ fails to discriminate between the two nodal planes is a rupture that propagates along the intermediate (N) axis of the event's focal mechanism. This most commonly occurs for large subduction zone thrust events where the rupture primarily propagates along the strike of the plate interface due to the limited down-dip extent of the seismogenic zone. In this case, the vector $\hat{\boldsymbol{\mu}}^{(1,1)}$ is coincident with the N-axis of the focal mechanism and therefore lies within both candidate fault planes of the focal mechanism. Thus, to develop a method for resolving the fault-plane ambiguity for a general planar source, we will use only the tensor quanitity $\hat{\boldsymbol{\mu}}^{(2,0)}$, but we will check our rupture plane identifications for consistency with $\hat{\boldsymbol{\mu}}^{(1,1)}$ for appropriate events.

Given estimates of $\mathbf{M}$ and $\hat{\boldsymbol{\mu}}^{(2,0)}$ the natural test for resolving the fault-plane ambiguity is to calculate the characteristic rupture extent, $x_c(\hat{\mathbf{n}})$, in the direction normal to each of the candidate fault planes of $\mathbf{M}$ and choose the fault-plane with the smaller value of $x_c(\hat{\mathbf{n}})$ as the true rupture plane. If an earthquake's fault were perfectly planar and our estimate of $\hat{\boldsymbol{\mu}}^{(2,0)}$ had no error, the true rupture plane would have $x_c(\hat{\mathbf{n}})=0$. In practice, neither of these conditions is true and $x_c(\hat{\mathbf{n}})$ has some finite positive value for both candidate fault-planes, thus it is necessary to simply choose the value closer to zero as diagnostic of the rupture plane.

5.3 Method

Our method for estimating $\mathbf{M}$, $\boldsymbol{\mu}^{(1,0)}$, $\boldsymbol{\mu}^{(0,1)}$, $\hat{\boldsymbol{\mu}}^{(2,0)}$, $\hat{\mu}^{(0,2)}$, and $\hat{\boldsymbol{\mu}}^{(1,1)}$ is described in detail in Chapter 4. Here we briefly summarize the method and discuss the data sets and constraints specific to this study. To isolate the effects of an earthquake's finite extent in space and time, we compare synthetic seismograms calculated for a point-source (usually the Harvard CMT solution) with data seismograms from a large earthquake. The synthetic seismograms are calculated by normal-mode summation for the PREM earth model (Dziewonski and Anderson, 1981), corrected for three dimensional elastic structure using the degree-12 aspherical model of Su *et al.* (1994) and the asymptotic approximations of Woodhouse and Dziewonski (1984). We also corrected fundamental modes above 7 mHz for smaller scale heterogeneity using the degree-40 phase-velocity maps of Ekström *et al.* (1997). The small differences between the data and synthetic seismograms resulting from the extent of the source are quantified in terms of differences in phase-delay $\delta\tau_p(\omega)$ and amplitude reduction time $\delta\tau_q(\omega)$ using the Generalized Seismological Data Functional technique of Gee and Jordan (1992). The differential phase delays, $\delta\tau_p(\omega)$, primarily result from the small difference between the point source used to calculate the synthetic seismograms and the true centroid location and moment-tensor. The differential amplitude measurements, $\delta\tau_q(\omega)$, primarily result from the finite spatial and temporal extent of the source that is unaccounted for in the point-source synthetics (Chapter 4).

The GSDF measurements, $\delta\tau_p(\omega)$ and $\delta\tau_q(\omega)$, were inverted for the moment-tensor, and the 1st and 2nd moments using an optimization technique called semidefinite programming (Vandenberghe and Boyd, 1996) that allows for the enforcement of various types of linear and non-linear constraints on the moments. The most important constraint we enforce is that the source region have non-negative volume, which is equivalent to requiring the following 4x4 matrix to be non-negative definite,

$$\text{and} \quad \begin{bmatrix} \hat{\boldsymbol{\mu}}^{(2,0)} & \hat{\boldsymbol{\mu}}^{(1,1)^{\mathrm{T}}} \\ \hat{\boldsymbol{\mu}}^{(1,1)} & \hat{\mu}^{(0,2)} \end{bmatrix} \geq 0\,. \tag{5.8}$$

This constraint ensures that all the eigenvalues of $\hat{\boldsymbol{\mu}}^{(2,0)}$, and hence the characteristic source extent in any direction, will be non-negative. To ensure that the source volume did not extend above the free-surface, we constrained the characteristic rupture dimension in the radial direction to be less than the centroid depth. The moment-tensor perturbations were constrained to have no isotropic component.

5.4 Results

We determined estimates (Tables 5.1, 5.2, and 5.3) of the 0th, 1st, and 2nd degree moments of 14 large shallow earthquakes using the technique described above and in Chapter 4. The event set consisted of 6 subduction related thrust events (Honshu, Chile, Jalisco, Alaska, Ecuador, and Taiwan), 2 oceanic transform fault events (Romanche and Rivera), and 6 intraplate or continental transform fault earthquakes (Burma, Aqaba, Tibet, Antarctica, Hector Mine, and Izmit). The earthquakes range in seismic moment from 2x10^{19} Nm (M_w 6.8) to 2.7x10^{21} Nm (M_w 8.2). For the largest events, Antarctica and Chile, the $\delta\tau_q$ measurements made on fundamental-mode Rayleigh waves showed anomalies resulting from directivity at frequencies as low as 3 mHz, while the smaller events required measurements on P-waves at fre-

Table 5.1: moment-tensor inversion results

date	region	rr	rθ	rϕ	$\theta\theta$	$\theta\phi$	$\phi\phi$
12/28/1994	Sanriku-Oki, Japan	1.8	0.14	-2.0	1.9	5.2	-.44
05/18/1995	Romanche Transform	-.004	.045	-.061	.0024	-.091	-.19
07/11/1995	Burma	-.008	-.196	.203	-.003	.003	.118
07/30/1995	Chile**	10.6	-.8	-11.7	2.2	-24.7	-.3
10/09/1995	Jalisco, Mexico	4.6	-3.2	-1.3	5.0	-3.0	1.9
11/22/1995	Aqaba, Egypt	-.18	-.65	.82	.48	-.05	-.81
06/10/1996	Alaska	4.2	-4.1	-.06	3.6	1.9	-1.9
05/01/1997	Rivera Transform	-.025	-.19	.21	-.01	-.034	-.272
11/08/1997	Tibet	-.11	-.63	.73	.02	1.01	1.73
03/25/1998	Antarctica*	-6.6	9.2	-2.6	-6.9	-4.0	15.0
08/04/1998	Ecuador	.36	.009	-.38	.064	-.55	-.032
08/17/1999	Izmit Turkey*	.03	-.10	.089	.03	-.51	-1.9
09/20/1999	Taiwan	1.8	-.42	-1.3	-3.0	-2.3	-.91
10/16/1999	Hector Mine	-.04	-.42	.42	-.01	.05	.34

values are in units of x 10^{20} Nm
* indicates events for which the moment tensor was not a free parameter
** indicates events for which the $M_{r\theta}$ and $M_{r\phi}$ components were not well resolved.

quencies as high as 45 mHz to resolve the 2nd moments. The fits to the GSDF measurements for each event are shown in Appendix C. For most events it was necessary to include both P-wave and fundamental mode Rayleigh wave data to stabilize the moment-tensor inversion, and for a few events the moment-tensor was not a free parameter in the inversion (Table 5.1).

5.4.1 Rupture plane identification

For each event, we determined the fault planes associated with the best double couple portion of the moment tensor (Table 5.4) and the characteristic rupture dimension in the direction normal to each candidate fault-plane, $x_c(\hat{\mathbf{n}})$, using (5.7) and the estimates of $\hat{\boldsymbol{\mu}}^{(2,0)}$ in Table 5.3. For 11 of the 14 events $x_c(\hat{\mathbf{n}})$ was more than a factor of two larger for one fault plane than the other, clearly identifying the rupture plane. For all 9 of the events that have a determination of the rupture plane using either local seismic or geodetic data (Japan, Chile, Jalisco, Aqaba, Alaska, Tibet, Turkey, Taiwan, and Hector Mine) the correct fault plane was chosen. Additionally

Table 5.2: 1st moments inversion results

earthquake	$\mu^{(0,1)}$		$\underline{\mu}^{(1,0)}$	
	time	lat.	lon.	dep.
Japan	12:20:00.0±.1	40.42±.01	143.05±.03	28.9±1.6
Romanche	00:06:37.4±.2	-0.65±.02	-21.88±.01	21.0±3.2
Chile	05:11:57.0±.1	-24.130±.002	-70.87±.01	27.8±0.7
Burma	21:46:48.2±.1	21.85±0.01	99.19±.01	15.0*
Jalisco	15:36:30.5±.4	19.48±.03	105.02±03	14.4±2.6
Aqaba	04:15:27.2±.1	29.03±.02	34.60±.01	16.4±1.0
Alaska	04:04:03.6±.1	51.21±.02	-177.42±.02	26.1±1.8
Rivera	11:37:39.8±.1	18.94±.01	-107.18±.01	21.8±1.0
Tibet	10:03:04.3±.1	35.13±.01	87.36±.03	11.3±2.4
Antarctica	03:13:01.6±.7	-62.74±.03	148.01±.06	11.3±2.4
Ecuador	18:59:30.1±.1	-0.64±.02	-80.61±.03	29.7±1.8
Turkey	00:01:51.5±.1	40.88±.01	29.98±.01	15.0*
Taiwan	17:47:36.6±.1	24.05±.02	120.85±.02	08.1±1.6
Hector Mine	09:46:56.7±.1	34.60±.1	116.43±.01	6.5±1.4

Latitude and Longitude are in degrees, depth in km, and the errors are ±2 standard deviations. * indicates the depth was fixed in the inversion.

Table 5.3: 2nd moments inversion results

earthquake	$\hat{\mu}^{(0,2)}$		$\underline{\hat{\mu}}^{(1,1)}$	
		r	θ	ϕ
Japan	61±8	0±13	-232±51	-318±60
Romanche	16±12	3±14	-35±86	113±58
Burma	1±1	0±2	-11±16	-16±26
Chile	125±24	-30±20	480±150	-269±100
Jalisco	214±217	0±89	-474±195	-621±149
Aqaba	21±17	6±6	-133±27	-15±25
Alaska	57±28	-90±16	247±44	299±79
Rivera	1±1	-4±3	1±12	39±28
Tibet	61±15	15±20	-12±19	-126±51
Antarctica	570±173	-150±256	-278±668	-2048±628
Ecuador	3±6	-10±13	-31±42	27±30
Turkey	9±5	8±21	-8±22	82±34
Taiwan	15±7	26±6	-90±45	-22±65
Hector Mine	1±3	0±3	17±19	21±13

All values have been normalized by the moment of the event, the units of $\hat{\mu}^{(0,2)}$ are s^2, $\underline{\hat{\mu}}^{(1,1)}$ are km s. r is the radial direction, θ is co-latitude, and ϕ is longitude. Errors are ±1 standard deviation.

Table 5.4: 2nd moments inversion results

			$\underline{\underline{\hat{\mu}}}^{(2,0)}$			
	rr	rθ	rϕ	$\theta\theta$	$\theta\phi$	$\phi\phi$
Japan	78±110	-2±3	147±158	911±319	1165±406	2051±769
Romanche	16±28	71±103	27±82	482±839	-228±511	816±381
Burma	0±5	0±1	0±15	177±412	245±434	348±624
Chile	142±15	0±1	37±331	2532±1086	246±444	3492±2037
Jalisco	24±9	56±158	-138±233	2483±1390	1116±1101	2625±1300
Aqaba	23±32	29±41	-40±65	1040±458	-11±332	74±219
Alaska	183±104	-539±304	-280±220	2620±647	863±1114	2711±549
Rivera	16±11	0±58	-153±82	78±534	37±384	1519±800
Tibet	64±15	1±14	-1±2	3±11	27±53	280±301
Antarctica	49±10	42±520	568±654	1624±2178	184±230	7834±4176
Ecuador	49±53	-153±65	-50 ±111	593±378	195±460	586±969
Turkey	24±44	4±17	146±156	21±56	-21±201	1067±614
Taiwan	45±5	-153±65	-50±111	539±378	195±460	586±969
Hector Mine	0±4	0±3	5±25	326±356	306±378	365±370

The units of $\underline{\underline{\hat{\mu}}}^{(2,0)}$ are km^2. Errors are ±1 standard deviation.

the 1998 Antarctic plate event has been studied teleseismically by various authors (Nettles *et al.*, 1999; Kuge *et al.*, 1999; Henry *et al.*, 2000), who found rupture on one or more faults corresponding to our chosen rupture plane. Based on plate-boundary kinematics, the fault-planes of the Romanche, Rivera, and Ecuador events also appear to be correctly determined.

The fault planes of the strike-slip events are generally the most clearly resolved. The eigenvector associated with the largest eigenvalue of $\hat{\boldsymbol{\mu}}^{(2,0)}$ for these events is oriented approximately along the strike of the rupture plane and hence normal to the auxiliary plane. The orientation of $\hat{\boldsymbol{\mu}}^{(1,1)}$ for these events confirmed the choice of fault plane. It is more difficult to resolve the fault-plane ambiguity for subduction zone thrust events for two reasons. First, for the thrust events, $\boldsymbol{\mu}^{(1,1)}$ is generally oriented along strike and therefore unable to differentiate between the two rupture planes. Secondly, the strikes of the shallowly dipping rupture plane and the near-vertical auxiliary plane are nearly identical in most cases. Thus when a rupture's

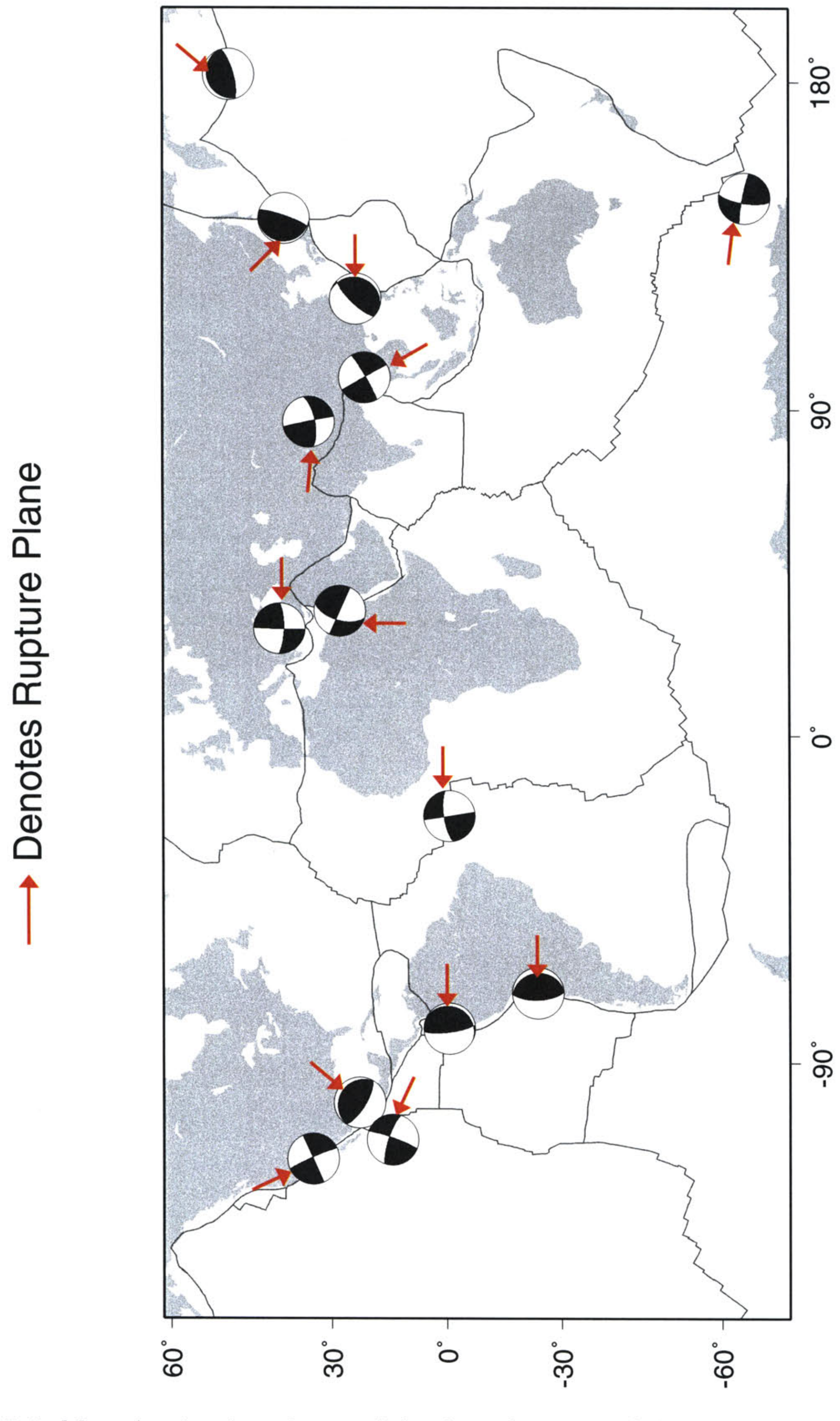

Figure 5-1: Map showing locations and focal mechanisms of the events in Table 5.4. Arrows point to the fault-plane with the smaller value of $x_c(\hat{n})$.

Table 5.5: Rupture plane test

earthquake	$x_c(\hat{\underline{n}}_1)$	Rupture strike	Plane dip	slip	$x_c(\hat{\underline{n}}_2)$	Auxiliary strike	Plane dip	slip
Japan	19±11	180	10	71	102±12	20	80	93
Romanche Transform	42±35	88	64	174	56±13	181	85	26
Burma	19±31	150	90	-179	42±37	60	89	0
Chile	35±12	89	12	103	115±31	175	78	87
Jalisco, Mexico	21±6	302	19	91	76±32	121	71	89
Aqaba, Egypt	26±15	199	66	-9	59±16	293	81	-156
Alaska	66±11	255	24	100	97±18	64	66	85
Rivera Transform	28±20	108	85	177	75±22	198	87	5
Tibet	11±5	80	62	2	32±18	349	88	152
Antarctica	83±52	281	84	17	164±42	189	73	174
Ecuador	10±19	14	18	108	60±10	175	73	84
Turkey	10±12	91	75	178	65±19	230	77	98
Taiwan	13±10	16	15	56	57±14	231	78	99
Hector Mine	22±19	334	89	175	48±25	65	85	1

Values of $x_c(\hat{\underline{n}})$ are in units of km. References confirming the correct choice of rupture plane are Sato *et al.* (1996)(Japan), Ruegg *et al.* (1996)(Chile), Melbourne *et al.* (1997)(Mexico), Klinger *et al.* (1999)(Egypt), Tanioka and Gonzalez (1998)(Alaska) Peltzer *et al.* (1999)(Tibet), Nettles *et al.* (1999) (Antarctica), and Barka (1999)(Turkey). Errors are 1 standard deviation.

largest dimension is along strike, the largest eigenvalue of $\boldsymbol{\mu}^{(2,0)}$ has an eigenvector that is consistent with both candidate fault-planes. To resolve the ambiguity for this geometry it is necessary to resolve the 2nd largest eigenvalue and its eigenvector which describe the downdip extent (or width) of the rupture. The $\mu_{r\theta}$ and $\mu_{r\phi}$ components of $\hat{\boldsymbol{\mu}}^{(2,0)}$, which determine the dip of the characteristic rupture volume, are difficult to determine for shallow thrust events for reasons similar to the well-documented difficulty in estimating the $M_{r\theta}$ and $M_{r\phi}$ components of the moment-tensor. For the Jalsico and Ecuador events, the dip was determined correctly allowing for a clear determination of the rupture plane. However, even in cases where the sign of the $\hat{\mu}_{r\theta}$ and $\hat{\mu}_{r\phi}$ components of $\boldsymbol{\mu}^{(2,0)}$ was incorrectly determined, such as the Alaska event, the correct rupture plane is chosen due to the large, near-horizontal extent of the rupture in the downdip direction.

5.4.2 Characteristic Rupture Properties

The second moment estimates can be interpreted in terms of characteristic rupture dimensions using equation (5.7). The characteristic rupture length, L_c, the characteristic rupture width, W_c, the characteristic rupture duration, τ_c, the characteristic rupture velocity, v_c, and the magnitude of the average velocity of the instantaneous centroid, v_0, for the 14 events are given in Table 5.5. Characteristic dimensions such as the length L_c are always smaller than the total dimension (length) of the rupture because of the weighted average nature of the 2nd moments. The exact relationship between L_c and the total rupture length, L, is different for every slip distribution. Since the slip distribution is not known for most earthquakes, it is often interesting to consider the equivalent dimensions of a rectangular (Haskell) rupture with spatially uniform slip that would produce the observed 2nd moments. Following Doornbos (1982a), the Haskell unilateral rupture model is described by the fault length (L), width (W), rupture velocity (v), total duration (T=L/v), and duration of slip at any one point (θ). Making the (slip-pulse) approximation $\theta^2 \ll T^2$ leads to:

$$\tau_c = \frac{1}{\sqrt{3}}T, \quad L_c = \frac{1}{\sqrt{3}}L, \quad W_c = \frac{1}{\sqrt{3}}W \tag{5.9}$$

For a unilateral Haskell rupture, $v_c = v_0 =$v, but for a symmetric bilateral rupture $v_c =$v and $v_0 = 0$ because the instantaneous centroid doesn't move during the rupture.

Earthquake scaling relations describe the relationships between various earthquake properties such as size, slip, duration or length. The average slip in an earthquake is approximately linearly related to the rupture length (Scholz *et al.*, 1986). This scaling is the constant stress-drop assumption (Hanks, 1977; Kanamori and Anderson, 1975). This relationship, $\Delta\overline{u} = \alpha L$ where $\Delta\overline{u}$ is the average slip, is parameterized by the slip to length ratio, α which is related to the average stress-drop in an earthquake. Assuming a constant value of α, usually between 10^{-4} (strike-slip events) to 10^{-5} (thrust events) (Scholz *et al.*, 1986), gives the following relationships between M_0 and

Table 5.6: Characteristic Rupture dimensions

earthquake	M_0 (10^{20} Nm)	L_c (km)	W_c (km)	τ_c (s)	v_c (km/s)	$\boldsymbol{v}_0$ (km/s)
Japan	5.9	106±12	30±23	16±1	6.7±.2	6.4±.1
Romanche Transform	.22	61±19	39±42	7.9±6.4	7.7±14.9	7.5±17.7
Burma	.23	46±38	4±44	2±2	27±107	26±56
Chile	27.2	119±34	99±19	22±1	5.3±.1	4.4±.1
Jalisco, Mexico	7.4	121±32	76±36	29±5	4.1±.4	3.7±.5
Aqaba, Egypt	1.2	65±14	19±21	9±1	7.0±2.0	6.4±1.7
Alaska	6.1	120±20	85±29	15±2	8.0±.5	7.0±.4
Rivera Transform	.34	78±20	18±60	2±2	40±61	39±62
Tibet	2.1	34±19	16±2	16±1	2.1±.6	2.1±.4
Antarctica	18.9	178±46	80±53	48±2	3.7±.1	3.6±.1
Ecuador	0.66	62±15	31±39	4±4	17±22	12±20
Turkey	2.0	66±18	8±12	6±1	11±3	9.7±2.2
Taiwan	4.2	±15	40±45	8±1	7.1±.7	6.3±.5
Hector Mine	.54	51±26	12±33	2±2	23±45	22±56

Errors are ±1 standard deviation.

the characteristic rupture dimensions for a unilateral rupture with uniform slip:

$$M_0 = 3\sqrt{3} G W_c \alpha L_c^2, \tag{5.10}$$

where G is the shear modulus. Because our catalog is small and contains errors, as well as the fact that a uniform slip distribution is likely a poor approximation for real earthquakes, directly interpreting our results in terms of equation (5.10) would be over interpretation. However, it is reassuring to see the expected linear increase in $\log(W_c L_c^2)$ with $\log(M_0)$ (Figure 5.2).

While the characteristic durations increase in size with moment as expected, the τ_c values for some of the smaller events appear to be underestimated. This systematic underestimation of τ_c for small events is obvious when examining the values of v_c and v_0. Both velocities are unphysically large for the smaller events, presumably due to the small values of $\mu^{(0,2)}$ which are incorporated in both quantities (see equation 5.7). Thus to compare v_0 and v_c it is necessary to remove the bias introduced by the

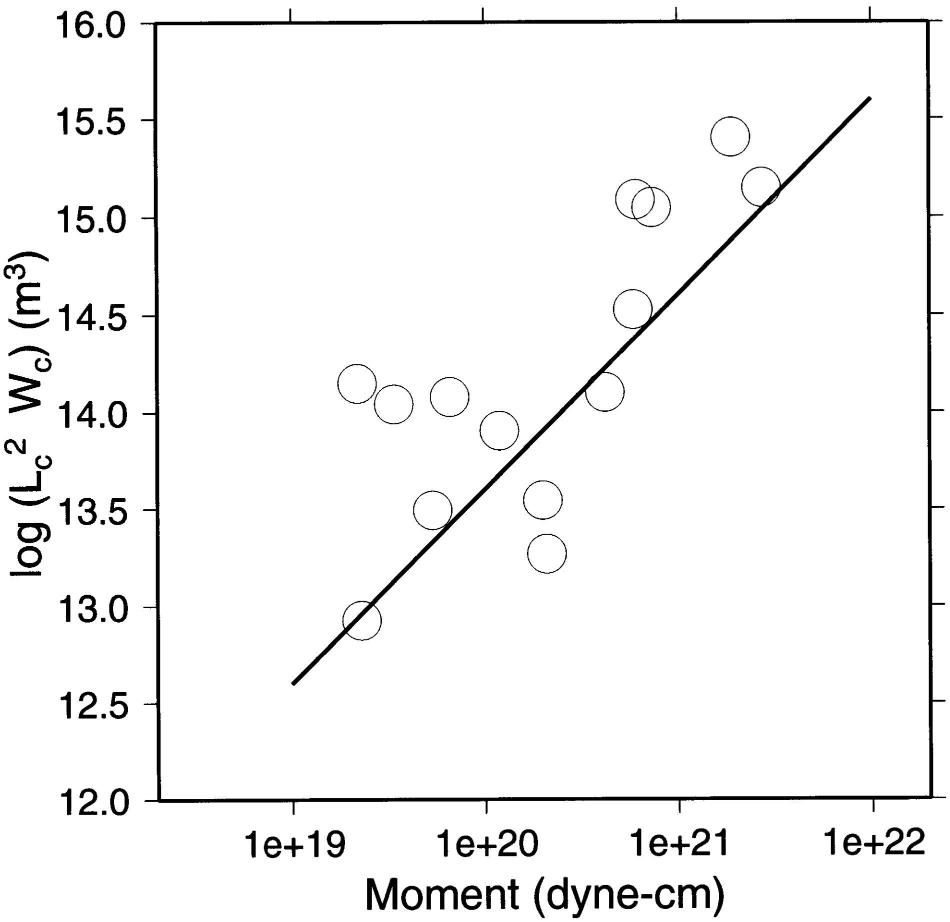

Figure 5-2: Plots of scaling relations for the events in Table 5.5. The line denotes a constant stress drop model (3.6 MPa) of a rectangular fault (L-model) with parameters corresponding to 15 km depth in PREM.

incorrect estimates of τ_c. Thus it is natural to compare L_c ($v_c \mathrm{x} \tau_c$) with the characteristic propagation distance of the centroid, L_0 ($v_0 \mathrm{x} \tau_c$). For a unilateral, uniform-slip rupture these two quantities will be equal, but for a symmetric bilateral rupture, L_0=0. Comparing these two quantities for the events in Table 5.6 shows that all of the ruptures were dominately unilateral (Figure 5-3). The events that deviate from the $L_0 = L_c$ line appear to accurately indicate the presence of a small bilateral component to the ruptures. For instance, the 1999 Hector Mine earthquake ($L_c = 51$ km, $L_0 = 44$ km) had a small component of rupture to the NNW despite being a primarily unilateral rupture to the SSE (M. Kikuchi, web page, and Table 5.3). This will be

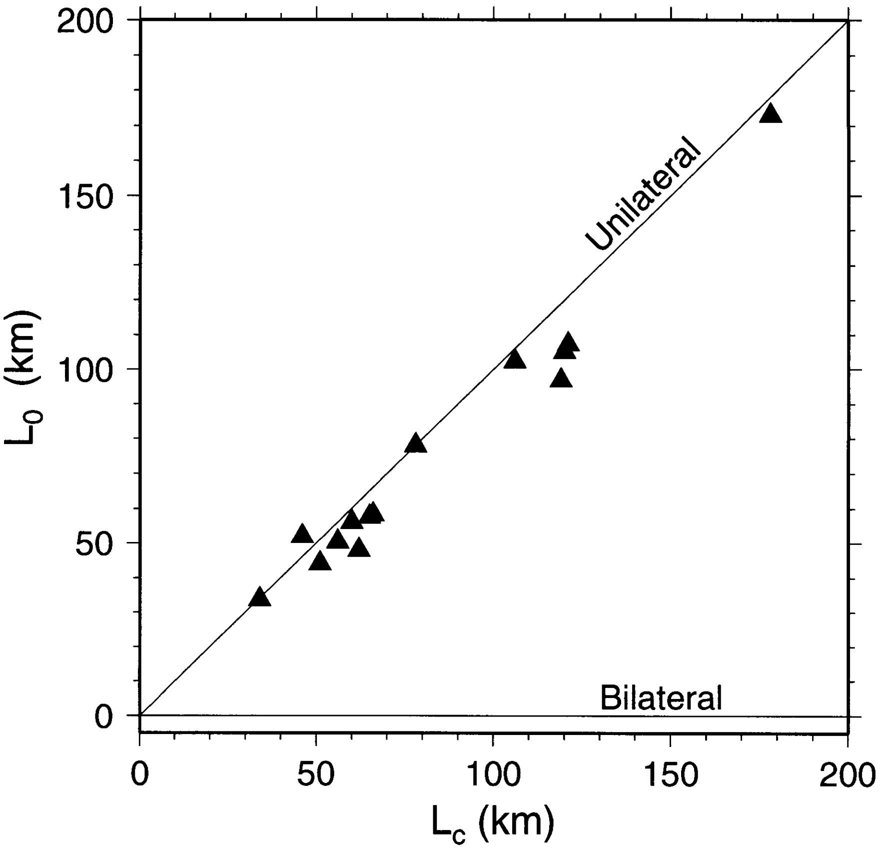

Figure 5-3: Plot of L_c vs L_0 for the events in Table 5.6.

an interesting property to evaluate with a larger, more accurate, and more complete catalog.

5.5 Discussion

The technique developed in Chapter 4 for determining the 2nd moments of earthquake ruptures was applied to a global dataset of large earthquakes ranging from M_w 6.8 to M_w 8.2. The estimates of $\boldsymbol{\mu}^{(2,0)}$ were used to calculate the characteristic rupture dimension in the direction normal to each of the two candidate fault-planes of the event's moment-tensor. Choosing the fault-plane with the smaller value of $x_c(\hat{\boldsymbol{n}})$ as the rupture plane correctly identified the rupture plane in all cases where it could be verified from local data or plate-boundary geometry. To determine the

2nd moments of the smaller events (M$\leq$7) it was necessary to include measurements of P-wave amplitude and phase-delay anomalies. For these events the $\mu^{(0,2)}$ appears to be underestimated, possibly resulting from not sampling a high-enough frequency band. The estimates of L_c and L_0 indicate that all of the ruptures studied were dominately unilateral. This will be an important observation to investigate with a more complete catalog that extends to smaller magnitude events.

Chapter 6

Complexities of Transform Fault Plate Boundaries in the Oceans

Abstract

Deformation of oceanic plates is primarily confined to the narrow axial and transform zones at their edges, but some oceanic transform boundaries show geologic evidence for migration of the boundary across a wider zone. We test the extent to which the current deformation is localized into a signal narrow fault valley for two such boundaries, the Romanche and Discovery II transforms. Earthquake relocation reveals that some large earthquakes involve subevents, or even entire ruptures, that break sub-parallel faults offset from the primary plate boundary. This observation is confirmed through the estimation of the space-time rupture properties of the 1994 Romanche and 1997 Prince Edward Island earthquakes. Both events show strong directivity signals that are oriented at a high angle to both the fault planes of their moment-tensor and the strike of the respective main transform faults. These events begin with episodes of smooth moment-release that radiate little to no high-frequency energy. The geometry of these events is consistent with the off-fault subevents being triggered by either the dynamic or static stress changes resulting from the slow components. Thus, these two plate boundaries show evidence for the interaction of multiple sub-parallel faults, suggesting that deformation beyond a single transform

valley occurs on both geologic and coseismic time-scales.

6.1 Introduction

Transform boundaries between oceanic plates are generally very sharp features where all of the relative motion occurs across a narrow zone. This localization of deformation contrasts with transform boundaries occurring in continental regions, such as the western United States, where deformation can be accommodated by multiple geologic structures distributed over a wide region. The region of oceanic crust affected by a transform fault, the transform domain (Fox and Gallo, 1984), can be several tens of kilometers wide and is usually centered on the transform valley. Within the transform domain, traces of active faulting are confined to a narrow region less than a few km wide termed the principal transform displacement zone (PTDZ) (Fox and Gallo, 1984). The remainder of the transform valley, including the walls, generally lacks signs of recent activity (Fox and Gallo, 1984). The PTDZ is considered to be the location of the current plate boundary within which all relative motion occurs. This localization of plate-motion within a belt $<\sim 2$ km wide appears to be enhanced for large offset transforms due to the thick lithosphere on the older side of the boundary (Fox and Gallo, 1984).

While present-day plate-motion is thought to be contained within the PTDZ, it is clear that on geologic time-scales deformation occurs over the broader region of the transform domain. This broader deformation is the result of migration of the principle transform fault within the fault valley as a response to changes in plate motion as well as non-transform deformation, such as the creation of transverse ridges. Occasionly the stresses resulting from changes in plate-motion are sufficiently large to cause the location of the boundary to jump to a new location outside the original transform valley (Tucholke and Schouten, 1988). In such cases, the deformation appears to occur over a wide-region on geologic time-scales despite being localized at any one time. Even in steady-state geometries, plate motion can be partially accommodated by distributed deformation up to 20 km beyond the edge of the fault-valley resulting in measurable curvature of abbysal hill structures (Fox and Gallo, 1984; Sonder and Pockalny, 1999).

There have been suggestions of active seismicity outside the PTDZ. An ocean bottom seismometer (OBS) study of microseismicity at the Kane transform recorded a significant number of events located outside the main transform valley (Wilcock *et al.*, 1990). The subevent locations of large earthquakes determined in Chapters 2 and 3 from high-frequency travel-time picks suggest that present-day coseismic deformation may occur across a wide region at both the Romanche and Discovery II transforms. In this chapter we explore the possibility that present-day deformation can be distributed over a wider region than the PTDZ through seismic rupture of multiple sub-parallel transform faults.

6.2 Geologic Observations of the Romanche Transform

The Romanche transform in the equatorial Atlantic is one of the most well documented examples of distributed deformation occurring in oceanic lithosphere on geologic time scales. At least four sub-parallel fault-valleys spanning a region 100-150 km wide are visible in gravity (Figure 6.1) and bathymetric (Searle *et al.*, 1994) maps of the western portion of the transform. The valley labeled C in Figure 6.1 has little to no sediment cover and contains the active transform fault that stretches for about 840 km between spreading segments. Valley D contains a paleotransform fault covered by 400-700m of sediment that can be traced from about 20° 20'W to 24° 20'W (Searle *et al.*, 1994). The eastern limit of this valley indicates that it ceased being the primary transform fault at about 27 Ma (Searle *et al.*, 1994). Valley B cuts through the northern transverse ridge to merge into the active transform valley near the eastern ridge-transform-intersection (RTI). It is covered in a few hundred meters of sediment and may have been the active trace of the Romanche transform before a change in plate motion occurred around 8-10 Ma (Bonatti *et al.*, 1994). Valley A located just north of the northern transverse ridge is visible in the bathymetric map of Searle *et al.* (1994) and may also be a paleotransform valley. This suite of fault-valleys combined with evidence for a ridge-jump event about 5 Ma near the eastern RTI (Bonatti *et al.*, 1994) provides clear evidence that the exact location of this plate boundary changes regularly over geologic time.

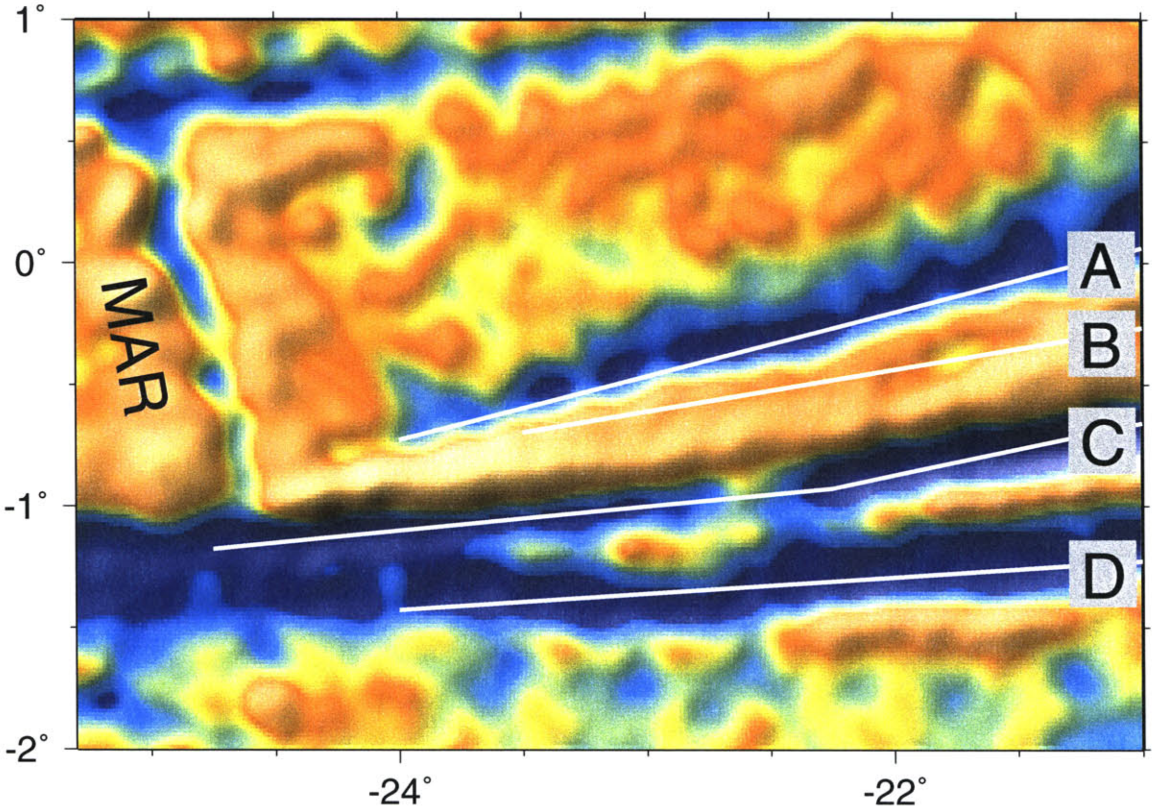

Figure 6-1: Map showing the western portion of the Romanche transform. Colors are the satellite altimetric free-air gravity field (Sandwell and Smith, 1997) . The gravity anomalies range from -15 mGal (blue) to +15 mGal (red), and the relief is illuminated from the northwest. The four fault-valleys labeled A,B,C, and D are described in the text. "MAR" denotes the Mid-Atlantic Ridge.

Perhaps the most spectacular evidence for the complex evolution of the Romanche transform boundary comes from the presence of a 140 Myr old limestone unit in the transverse ridge only about 100 km from the eastern RTI (Bonatti *et al.*, 1996). To explain the presence of this unit and other continental material (Bonatti, 1990) near the spreading axis of the MAR, *Bonatti* (1994,1996) has proposed the oscillatory spreading hypothesis. In this model, the pieces of continental material have been repeatedly transfered back and forth between the African and South American plates owing to changes in the location of the transform and accretionary plate-boundaries. The most-recent episode of transform-fault migration appears to have transfered the material between valleys B and C in Figure 6.1 from the South American Plate to the African Plate about 8-10 Ma (Bonatti *et al.*, 1994). Thus the location of the plate boundary may have shifted between the various faults shown in Figure 6.1 over geologic time in such a way that the Cretaceous limestone unit remained near the MAR for more than 100 Ma.

6.3 Seismicity of the Romanche Transform

We began studying the current-day deformation of the Romanche transform by relocating all the earthquakes in the ISC catalog from 1964 to 1996 using the clustered event algorithm of Jordan and Sverdrup (1981). This technique produces estimates of the relative locations of the events that are independent of common path anomalies as well as an estimate of the absolute position of the seismicity cluster. We divided the Romanche transform into four overlapping regions (-25.5°E to -21°, -22.5° to -19° , -20° to -17.5°, and -18° to -15.5°) and simultaneously relocated all the events within a region. All event depths were constrained to 10 km, and only events with 30 or more P and PKP arrival times were used. The results show that the vast majority of seismicity is concentrated into a series of seismicity clusters within the main transform valley (valley C). There are two notable gaps in the seismicity centered at -23° and -21° which stretch for about 100-150 km along the strike of the fault. Another interesting feature of the seismicity is that it appears to extend 50-100 km beyond the eastern RTI (Figure 6-2D). This cluster of events, which is centered around (-26.5°E, 0.5°N), is dominated by a series of events in September 1993 including a m_b 5.2 (Sept. 18th, 1993) and an m_b 5.4 (Sept. 21 1993) event. The extent of seismicity past the RTI agrees well with models of the geoid anomalies over fracture zones which suggest that they may take up to 4 Ma after passing the RTI to completely lock (Wessel and Haxby, 1990). The presence of these moderately sized events past the end of the

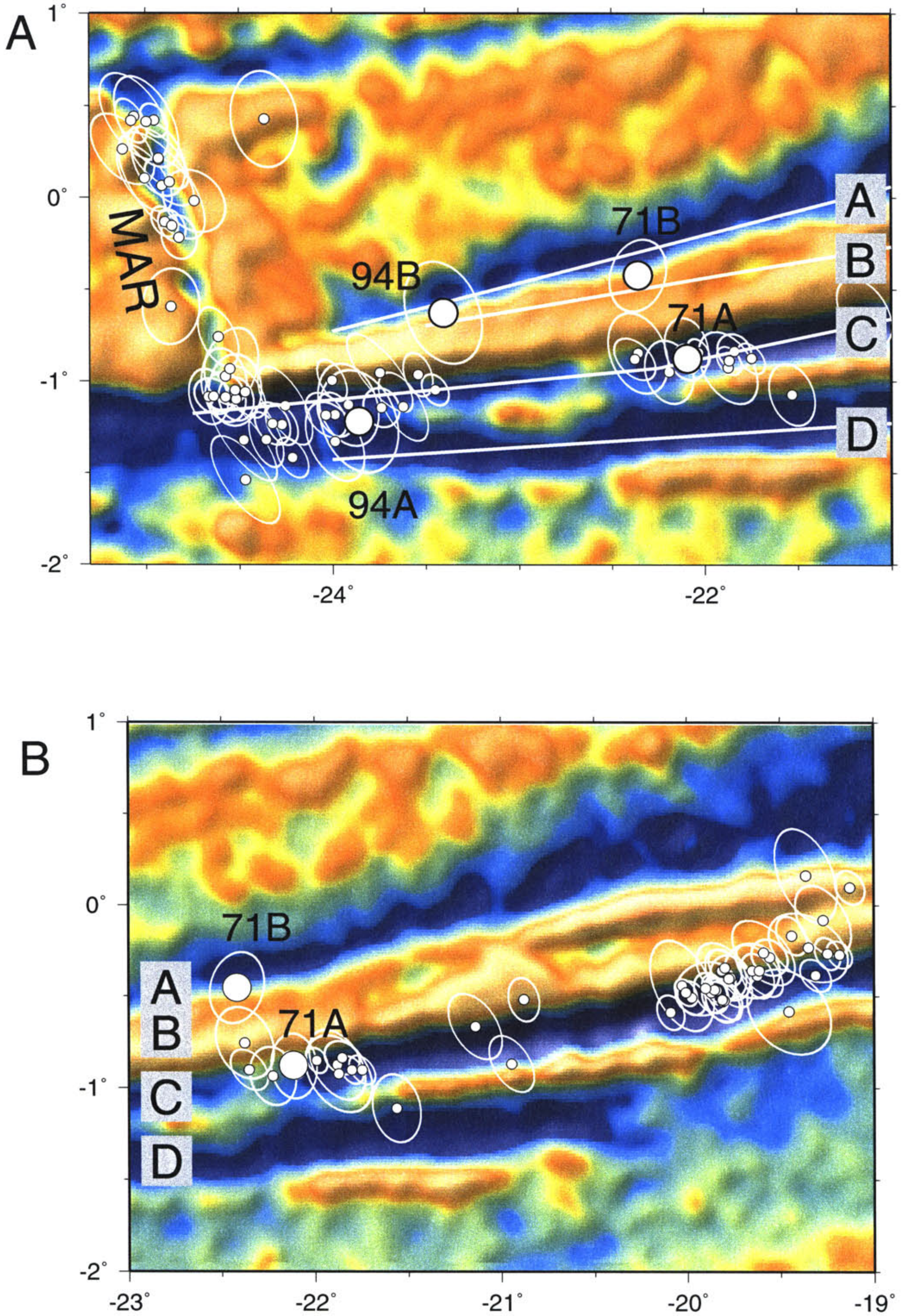

Figure 6-2: Maps showing the western portion of the Romanche transform. Colors are the satellite altimetric free-air gravity field (Sandwell and Smith, 1997) . The gravity anomalies range from -15 mGal (blue) to +15 mGal (red), and the relief is illuminated from the northwest. The four fault-valleys labeled A,B,C, and D are described in the text. "MAR" denotes the Mid-Atlantic Ridge. Small circles give locations and 95% confidence ellipses of the relocated background seismicity. Large circles denote locations and 95% confidence ellipses of the subevents of the 1971 and 1994 M_w 7.0 earthquakes.

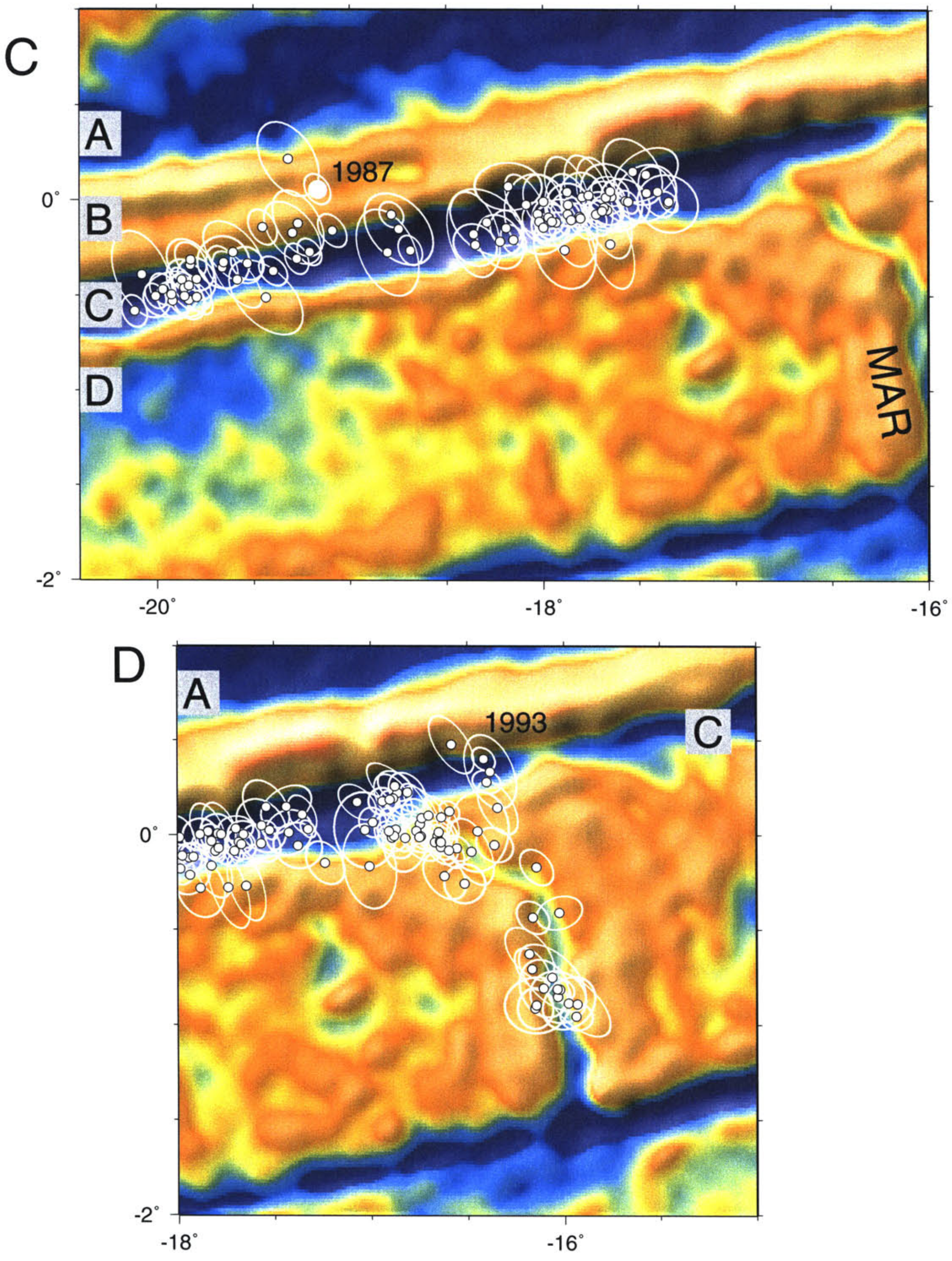

Figure 6-2: Maps showing the eastern portion of the Romanche transform. Colors are the satellite altimetric free-air gravity field (Sandwell and Smith, 1997) . The gravity anomalies range from -15 mGal (blue) to +15 mGal (red), and the relief is illuminated from the northwest. The four fault-valleys labeled A,B,C, and D are described in the text. "MAR" denotes the Mid-Atlantic Ridge. Small circles give locations and 95% confidence ellipses of the relocated background seismicity.

active plate boundary may also result from the unusual oblique nature of the eastern RTI.

Table 6.1: 1971 Mainshock Delay Times

Station	Azimuth	Delta	B-A Time, s
BUL	115	53	13.6
GRM	131	56	12.6
SDB	113	38	11.0
PRE	121	54	15.0
NAI	91	59	10.6
SHI	59	77	10.6
AAE	79	62	11.6
COP	21	63	9.6
EIL	56	62	10.1
ESK	13	58	11.3
HLW	54	59	10.2
JER	53	63	10.0
KON	17	65	10.6
KBL	56	91	9.6
NUR	22	71	9.6
KTG	00	71	7.8
QUI	270	56	6.0
SJG	296	47	7.1
LPA	221	48	12.1
GOL	310	85	6.9
ATU	43	57	9.9
KEV	16	77	10.2
BEC	315	51	6.0
DAL	304	77	6.6
JCT	301	78	6.5
LUB	304	82	7.2
WIN	121	45	15.0

While the vast majority of seismicity locates within the transform valley, there are several events located outside this zone. Most of these events are small (M_b 4.5) events whose 95% confidence ellipsoids nearly overlap the main fault valley. Hence they do not appear to represent a significant amount of distributed deformation. However, there are several large earthquakes that locate near the 'paleo-transform' faults labeled A and B in Figure 6.1. The May 5th, 1987, (M_w 6.0) event location is shown in Figure 6.2C. This large event has over 150 P-wave arrival time picks and good azimuthal coverage resulting in location uncertainties of $\leq$10 km. Its location is within the fault-valley (B) suspended in the northern transverse ridge. This fault, identified by Bonatti *et al.* (1994) as probably having been the primary trace of the Romanche transform until about 8-10 Ma, appears to still be capable of producing a magnitude 6.0 strike-slip earthquake.

We also included arrival time picks of the largest subevents in the M_w 7.0 Romanche transform earthquakes of 1971 and 1994. Both of these events began with a small preshock that was followed by a much larger mainshock. Picking the P-wave arrivals from later arriving subevents is generally not possible for shallow earthquakes due to the interference from depth phases. However, the 2nd subevents of these events were approximately 10 times larger than the preshocks making their first arrivals distinguishable from the preshock coda (see Figure 2.4). Forsyth *et al.* (1986) found that the mainshock of the 1971 event occurred 10 s later than and was located 60 km to the NNW of the preshock. Using arrival time picks made of WWSSN records (Table 6.1) our relative location produced almost identical results to those of Forsyth *et al.* (1986). The 1971 preshock (labeled 71A in Figure 6.2A) is located in the main transform valley while the mainshock (labeled 71B) is located 58 km to the NNW. The location of the mainshock is inconsistent with it rupturing the main transform and suggests that this subevent ruptured either paleotransform A or B. Using our travel-time picks for the preshock and mainshock of the 1994 event (Chapter 2) we also find that the location of its mainshock is consistent with paleotransforms A and B but not with the Romanche PTDZ. Thus, while the vast majority of small seismicity and several large (M_w ~7) events occur along the main transform, it appears from P-wave travel-time based locations that at least one of the paleotransforms is still seismically active.

6.4 Second Moments of Slow-Earthquakes

The subevent locations of large earthquakes discussed in the previous section and in Chapters 2 and 3 suffer from a potentially large source of bias owing to the difficulty in distinguishing later arriving P-waves from depth phases. Thus a more robust method for determining the rupture extent of large oceanic transform fault events is the 2nd moment estimation technique developed in Chapter 4. This method requires only teleseismic surface and body-wave data and can utilize the frequency bands that are sensitive to directivity for a given size earthquake. We have estimated the 2nd moments of three large earthquakes on the Romanche and Discovery II transforms to investigate the possibility that some of these events ruptured multiple sub-parallel faults.

6.4.1 The 1994 and 1995 Romanche earthquakes

The western portion of the Romanche transform recently ruptured in two large events, the March 14, 1994, M_w 7.0, and the May 18, 1995, M_w 6.8, earthquakes. We measured the phase-delay and amplitude-reduction times relative to synthetic seismograms for the 1st and 2nd orbit Rayleigh waves, and P-waves at global teleseismic stations using the Generalized Seismological Data Functional (GSDF) technique of Gee and Jordan (1992). The synthetic seismograms were calculated by mode-summation for the PREM earth model (Dziewonski and Anderson, 1981), corrected for 3 dimensional elastic structure using the degree-12 aspherical model of Su *et al.* (1994) and the asymptotic approximations of Woodhouse and Dziewonski (1984). We also corrected fundamental modes above 7 mHz for smaller scale heterogeneity using the degree-40 phase-velocity maps of Ekström *et al.* (1997). The source is specified by an initial centroid location, centroid time, and moment tensor corresponding to the Harvard CMT solution for each event (Dziewonski *et al.*, 1999). Measurements of 2nd orbit Rayleigh waves, which have greater contamination from unmodeled propagation effects, was necessary to achieve sufficient azimuthal coverage. The measurements (Figures 6-3 and 6-4) for both events show phase-delay times, $\delta\tau_p(\omega)$, that are roughly independent

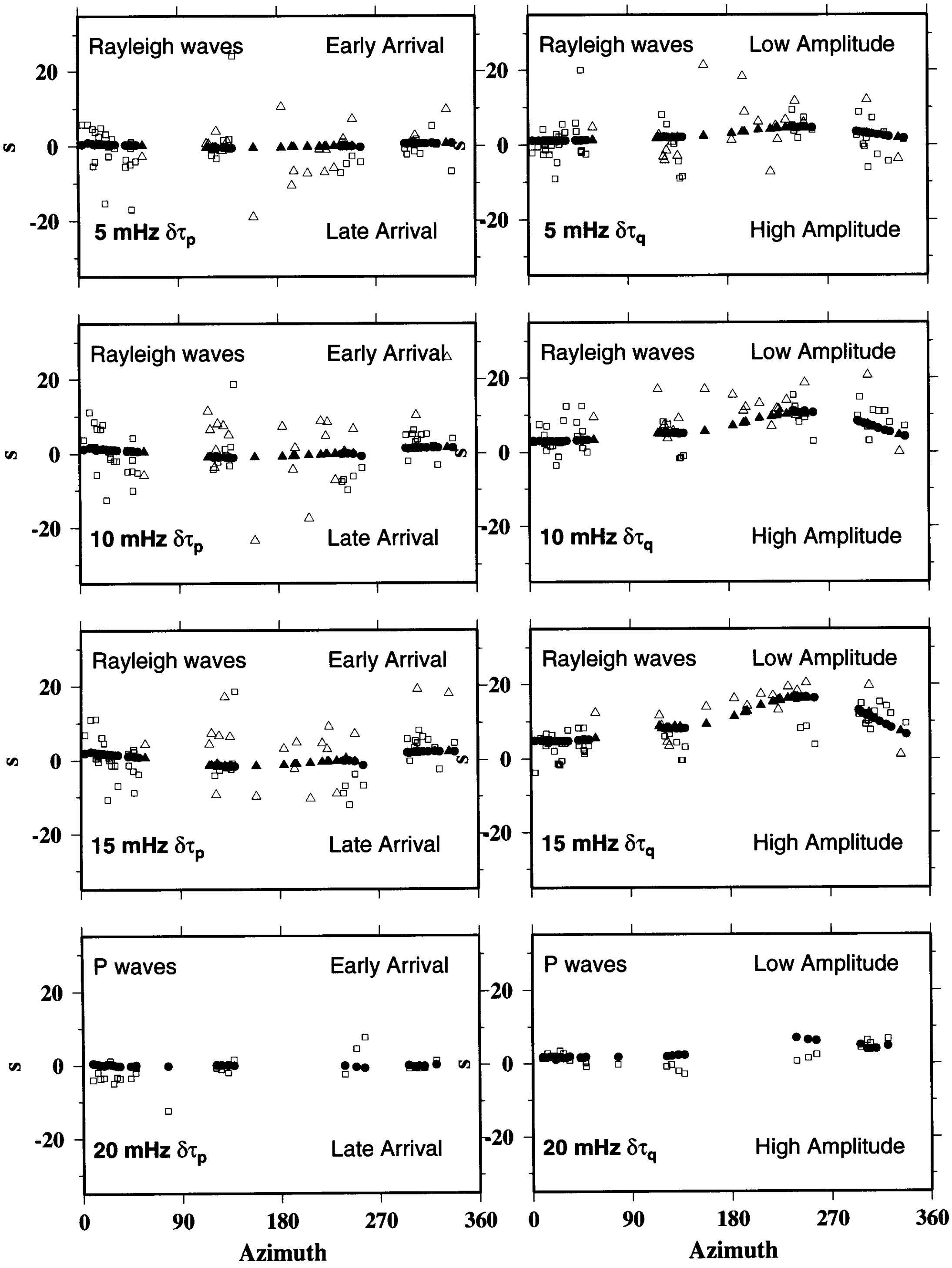

Figure 6-3: GSDF measurements of the 1994 Romanche transform earthquake at 5, 10, 15, and 20 mHz. Open squares denote R1 and P-wave measurements and open triangles denote R2 measurements. Filled symbols indicated the fit to the data produced by the estimates of the 0th, 1st, and 2nd moments in Tables 6.2, 6.3, and 6.4.

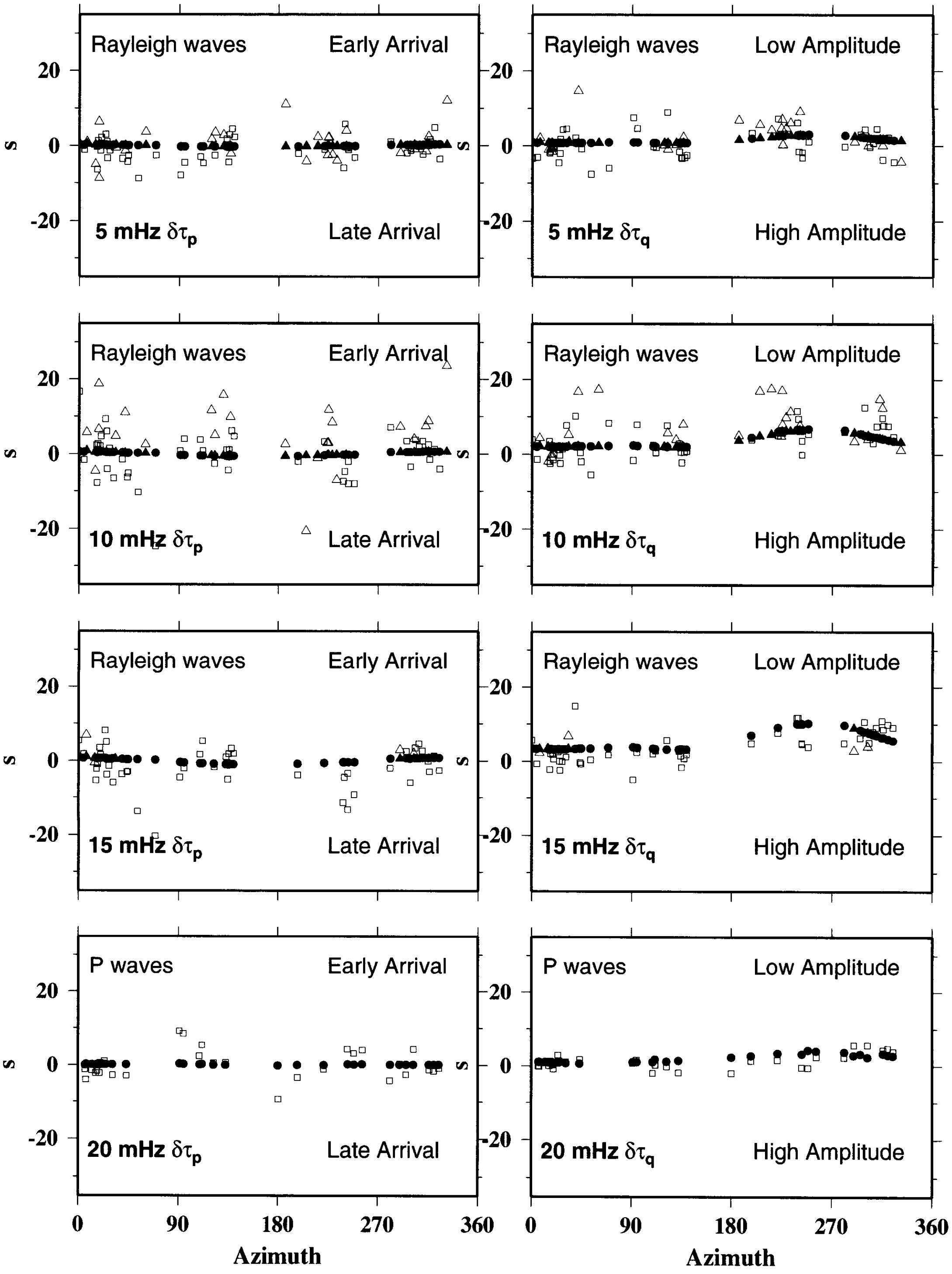

Figure 6-4: GSDF measurements of the 1995 Romanche transform earthquake at 5, 10, 15, and 20 mHz. Open squares denote R1 and P-wave measurements and open triangles denote R2 measurements. Filled symbols indicated the fit to the data produced by the estimates of the 0th, 1st, and 2nd moments in Tables 6.2, 6.3, and 6.4.

of azimuth indicating that the CMT centroid locations were approximately correct for both events. The amplitude reduction times, $\delta\tau_q(\omega)$, show a systematic increase with frequency for Rayleigh waves that leave to the west or southwest of the source. These positive values, corresponding to a reduction in data amplitude relative to point-source synthetics, indicate that rupture propagated primarily to the E or NE.

Inverting the measurements in Figures 1.3 and 1.4 for the 0th, 1st, and 2nd moments of the rupture distribution yielded the estimates in Tables 6.2, 6.3, 6.4 and 6.5. For the 1995 event, the 2nd moments correspond to a characteristic duration, τ_c, of 7.9±6.4 s, a characteristic rupture length, L_c, of 61±19 km at an azimuth of 64°, an average centroid velocity, v_0 of 7.5 km/s at an azimuth of 73°. For the 1994 Romanche event, the 2nd moments correspond to a τ_c of 13±7 s, a L_c of 99±13 km at 64°, and a $\mathbf{v_0}$ of 7.6±11.8 km/s at 57°. The centroid locations, characteristic source volumes, and directivity vectors for the two earthquakes are shown in Figure 6-5. The characteristic source volume and direcitivty vectors for the 1995 event are nearly aligned with the strike of the main transform in this region. The strike of the main transform undergoes a series of discrete changes along strike (Bonatti *et al.*, 1994). One of these changes occurs at about 22°W such that in the region of the 1994 event the fault strikes almost E-W while near the centroid of the 1995 event its strike has rotated towards ENE [*Bonatti et al.* 1994; Figure 6-5]. Thus the estimate of $\mathbf{v_0}$ for the 1994 event has an orientation, N57°E, that is at a high angle to the strike of the main-transform valley (Figure 6-5). The mixed-moment between space and time that defines $\mathbf{v_0}$ is the most well resolved of the 2nd moments due to the large effect it has on the amplitudes of surface and body waves. The NE-SW orientation of $\mathbf{v_0}$ (the second-order moment) is inconsistent with rupture on one of the two nodal planes of the events moment tensor (the zeroth order moment) which strike roughly E-W and N-S. Additionally, the 1994 event's centroid location (the 1st moment) lies in between fault valleys B and C, although both faults are within its uncertainty. The only type of source model that can satisfy the observed 0th, 1st, and 2nd moments is one that involves failure of two nearly parallel faults that correspond to one of the moment-tensor's nodal planes but are offset in such away as to produce the observed

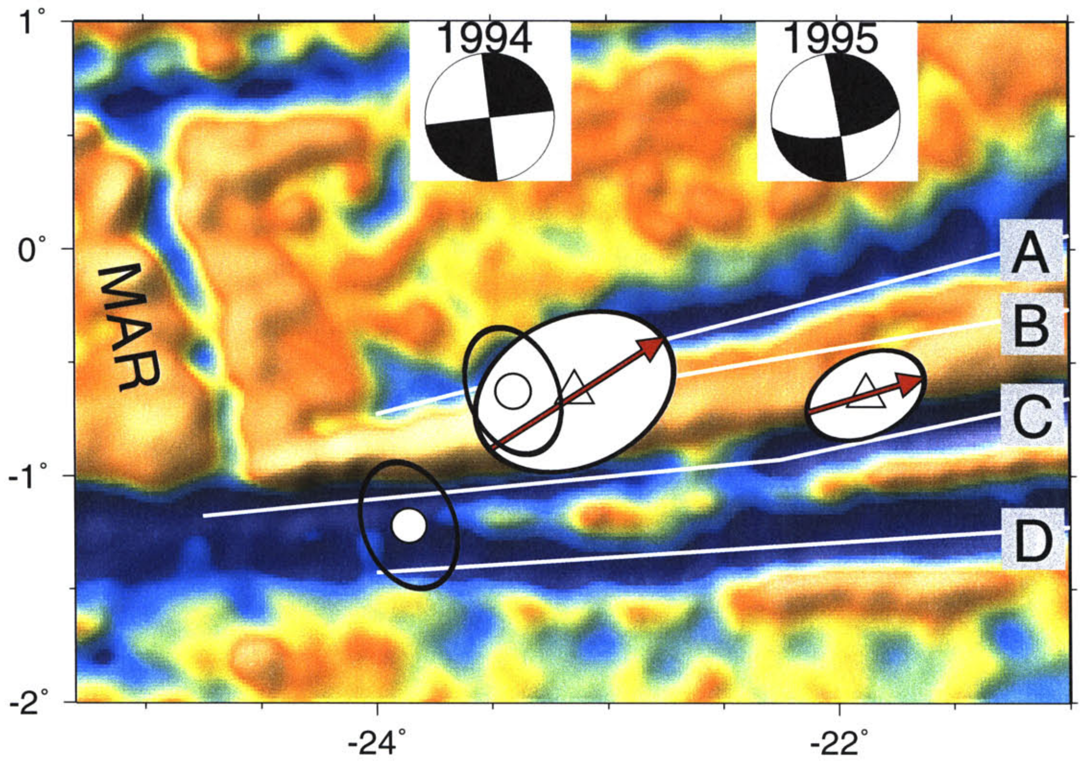

Figure 6-5: Map showing the western portion of the Romanche transform. Colors and white lines denote the gravity field and fault locations as in Figure 6.1. Focal mechanism inserts show the Harvard CMT solutions for the 1994 and 1995 events. The white circles surrounded by black ellipses denote the locations and 95% confidence regions for the initial and main high-frequency subevents of the 1994 event determined in section 6.2. The triangles show the centroid locations of the 1994 (23.14±.01°W, 0.63±.04°S) and 1995 (21.88±.01°W, 0.65±.02°S) events. The white ellipses with black borders that are centered on the centroid locations denote the map-view projection of the characteristic rupture volume defined by our estimates of the 2nd spatial moment for each earthquake. The red vectors denote the average directivity vector specified by the mixed space-time moment. The length of these vectors has been scaled to be equal to $\tau_c \mathrm{x} v_0$.

2nd moments. The subevent locations for the 1994 event indicate rupture of either fault A or B as well as rupture of fault C, with the rupture of fault A/B occurring to the northeast of the rupture of fault C. This type of source-model can satisfy the observed moment-tensor because the B and C faults are sub-parallel. It can also satisfy the centroid location which is intermediate between the two faults and the NE directivity associated with the estimates of the second moments.

Table 6.2: moment-tensor inversion results

earthquake	rr	rθ	rϕ	$\theta\theta$	$\theta\phi$	$\phi\phi$
1994 Romanche	-.028	.089	-.061	-.079	-.027	-.36
1995 Romanche	-.004	.045	-.061	.0024	-.091	-.19

values are in units of 10^{20} Nm

6.4.2 The 1997 and 1998 Discovery II earthquakes

The April 28, 1997, M_w 6.8, Prince Edward Island earthquake that ruptured the Discovery II transform showed evidence from subevent locations that suggested directivity at a high-angle to either fault-plane of the events moment-tensor, similar to the 1994 Romanche quake (Chapter 3). To investigate this directivity, we made measurements of the phase-delay, $\delta\tau_p$, and amplitude-reduction, $\delta\tau_q$, times of 1st orbit Rayleigh and P- waves (Figure 6-6) using the GSDF technique (Gee and Jordan, 1992). The synthetic seismograms used in the measurement process were calculated for the Harvard CMT by mode-summation as in the previous section. The low-

Table 6.3: 1st moments inversion results

earthquake	$\mu^{(0,1)}$		$\mu^{(1,0)}$	
	time	lat.	lon.	dep.
1994 Romanche	04:30:34.8±.3	0.63±.04°S	23.14±.01°W	6.3±3.4
1995 Romanche	00:06:37.4±.2	0.65±.02°S	21.88±.01°W	21.0±3.2
1997 Prince Edward	12:07:48.2±.2	42.047±.003°S	42.64±.02°E	5.2±1

Errors are ±2 standard deviations.

Table 6.4: 2nd moments inversion results

earthquake	$\hat{\mu}^{(0,2)}$		$\underline{\hat{\mu}}^{(1,1)}$	
		r	θ	ϕ
1994 Romanche	40±28	-11±42	-168±183	255±173
1995 Romanche	16±12	3±14	-35±86	113±58
1997 Prince Edwards	22±3	-25±8	71±28	54±40

All values have been normalized by the moment of the event, the units of $\hat{\mu}^{(0,2)}$ are s^2, $\underline{\hat{\mu}}^{(1,1)}$ are km s. r is the radial direction, θ is co-latitude, and ϕ is longitude. Errors are ±1 standard deviation.

Table 6.5: 2nd moments inversion results

			$\underline{\underline{\hat{\mu}}}^{(2,0)}$			
	rr	rθ	rϕ	$\theta\theta$	$\theta\phi$	$\phi\phi$
1994 Romanche	73±10	242±208	136±349	1456±1333	-482±941	2241±779
1995 Romanche	16±28	71±103	27±82	482±839	-228±511	816±381
1997 Prince Edwards	49±8	-9±21	-11±155	561±482	272±405	439±667

The units of $\underline{\underline{\hat{\mu}}}^{(2,0)}$ are km^2. Errors are ±1 standard deviation.

frequency R1 $\delta\tau_p$ measurements show late arrivals at stations to the SW indicating that the true centroid location is shifted in this direction. The low-frequency measurements of $\delta\tau_q$ for R1 show no systematic signal as a function of azimuth indicating the starting moment-tensor was approximately correct. The higher frequency P-wave measurements show systematic signals in both $\delta\tau_p$ and $\delta\tau_q$. The anomalies in $\delta\tau_q$, indicating large P-wave amplitudes at stations to the SE and small amplitudes at stations to the N and NW, increase in magnitude with frequency as would be expected for the effects of directivity. The $\delta\tau_p$ anomalies show no such increase, as would be expected for a shift in the true centroid location from the assumed location. To determine if the $\delta\tau_q$ anomalies were indeed a result of directivity, we compared the measurements for the 1997 event to measurements for a M_w 6.1 event in 1998 that also ruptured the Discovery II transform. The measurements of the 1998 event should show almost no directivity effects at these frequencies owing to its smaller seismic moment. The $\delta\tau_p$ measurements show a very similar azimuthal pattern to those for the 1997 event, indicating that these travel-time anomalies likely result from unmodeled 3-D heterogeneity rather than properties of the seismic source. The $\delta\tau_q$ measurements for the 1998 event show a nearly constant value as a function of azimuth and do not increase in amplitude with frequency. They have a mean of about -1±1.7 s. The small scatter (±1.7 s) indicates that P-wave measurements for sources in this region show relatively small anomalies in their amplitudes due to unmodeled propagation effects. Thus, the clear signal in the 1997 event's P-wave amplitude measurements, that indicates NW-SE directivity, appears to be a true source effect.

To quantify the 1997 event's directivity, we inverted the $\delta\tau_p$ and $\delta\tau_q$ measurements in Figure 6-6 for the 1st and 2nd moments of its rupture. The moment tensor was fixed to the CMT value. The inversion results (Tables 6.3 and 6.4) correspond to a L_c of 56±15 km at and azimuth of 142°, a τ_c of 9±2 s, and a $\mathbf{v_0}$ of 4.2±9.9 km/s at an azimuth of 143°. This strong NW-SE directivity is at a high angle to the strike of the Discovery II transform (Figure 6-8), and the fault planes of the event's focal mechanism. Rupture propagation on a fault with a strike of 143° can be ruled out by the event's moment-tensor. However, the orientation of the 2nd moments can be

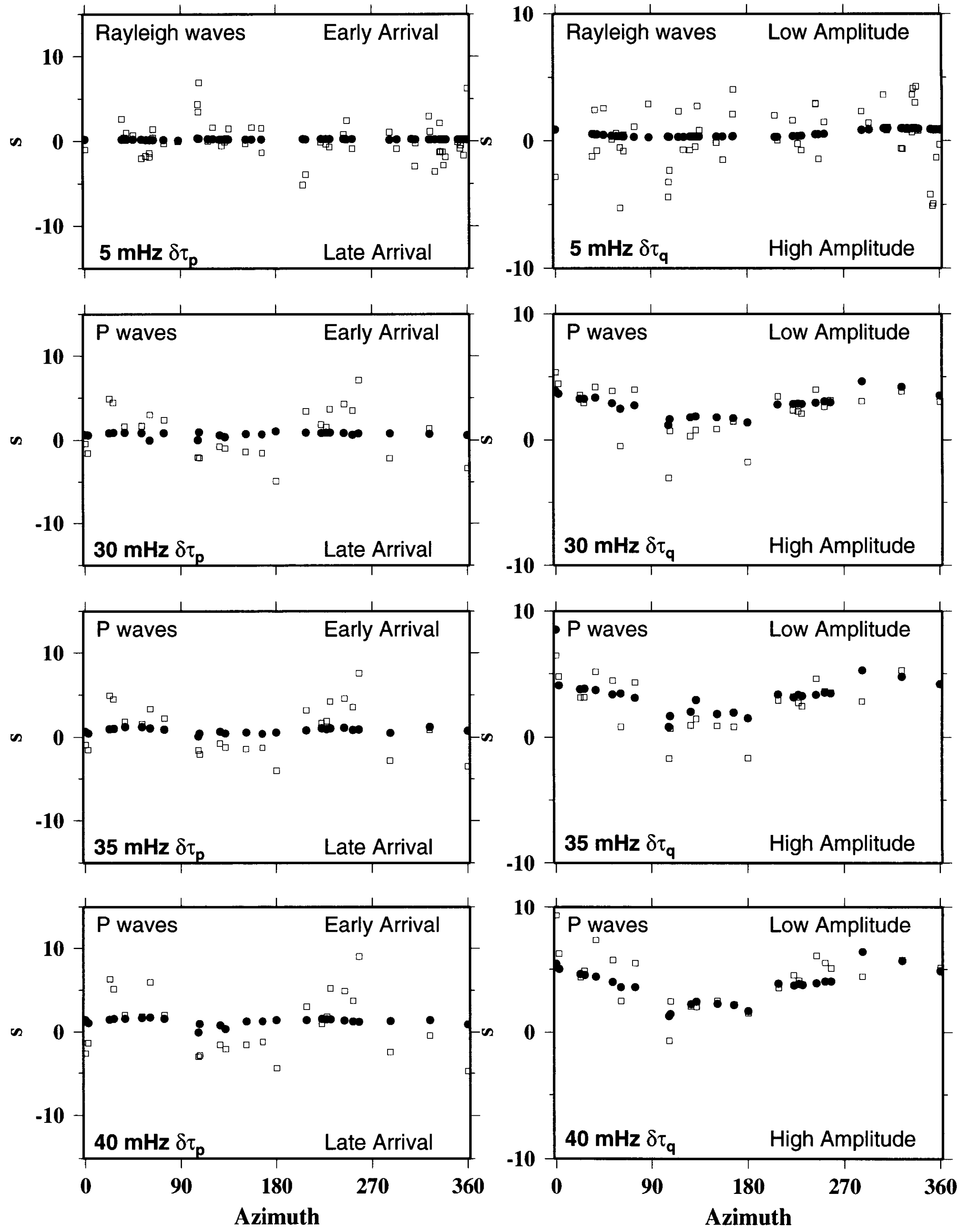

Figure 6-6: GSDF measurements of the 1997 Prince Edward Island earthquake at 5 mHz for R1 and 30, 35, and 40 mHz for P-waves. Open squares denote measurements, and filled squares indicated the fit to the data produced by the estimates of the 0th, 1st, and 2nd moments in Tables 6.3 and 6.4.

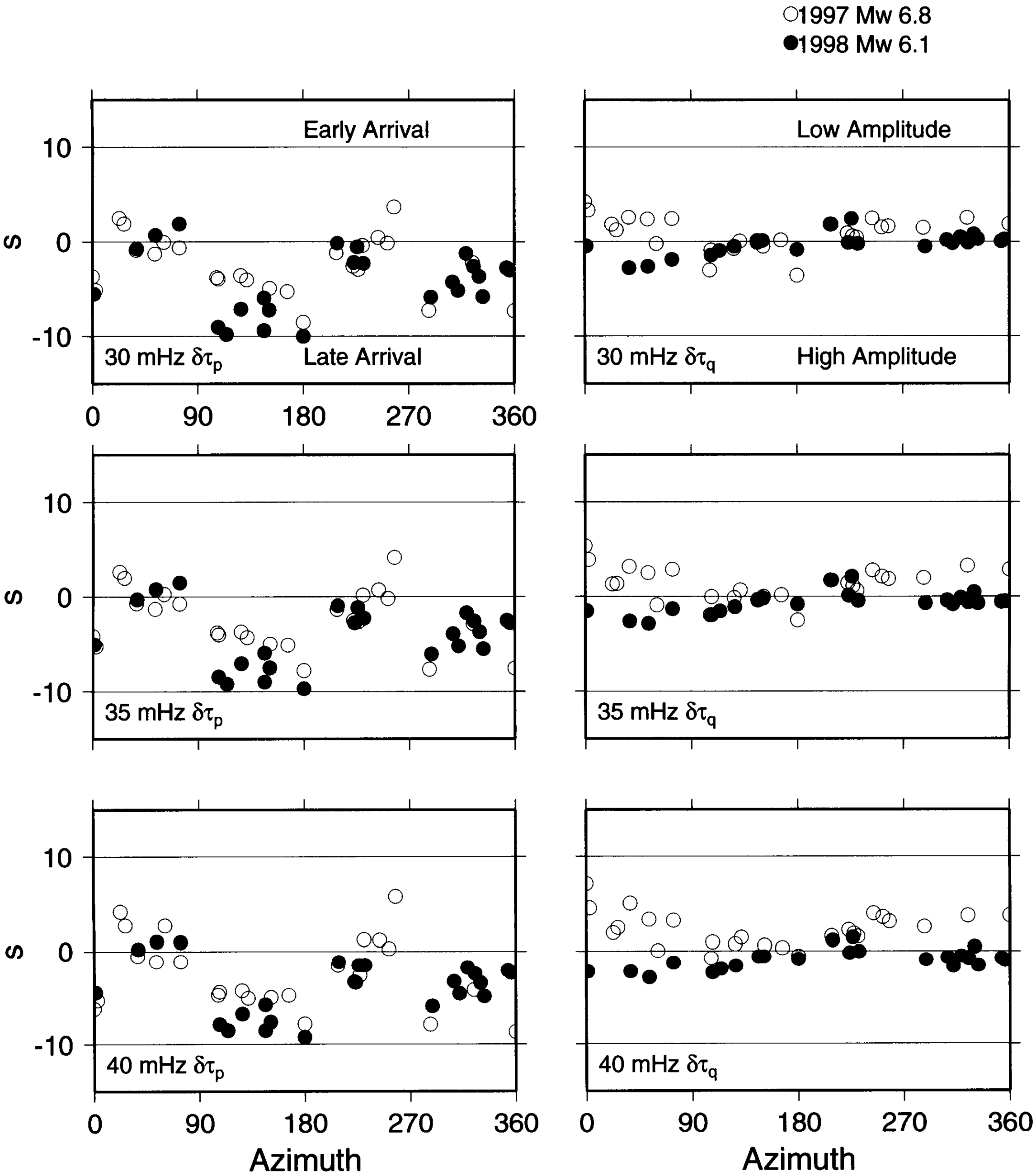

Figure 6-7: GSDF measurements of the P-waves for the 1997 and 1998 Prince earthquakes on the Discovery II transform. The solid circles are for the M_w 6.1, May, 21, 1998 event and the open circles for the M_w 6.8, April, 28, 1997 event.

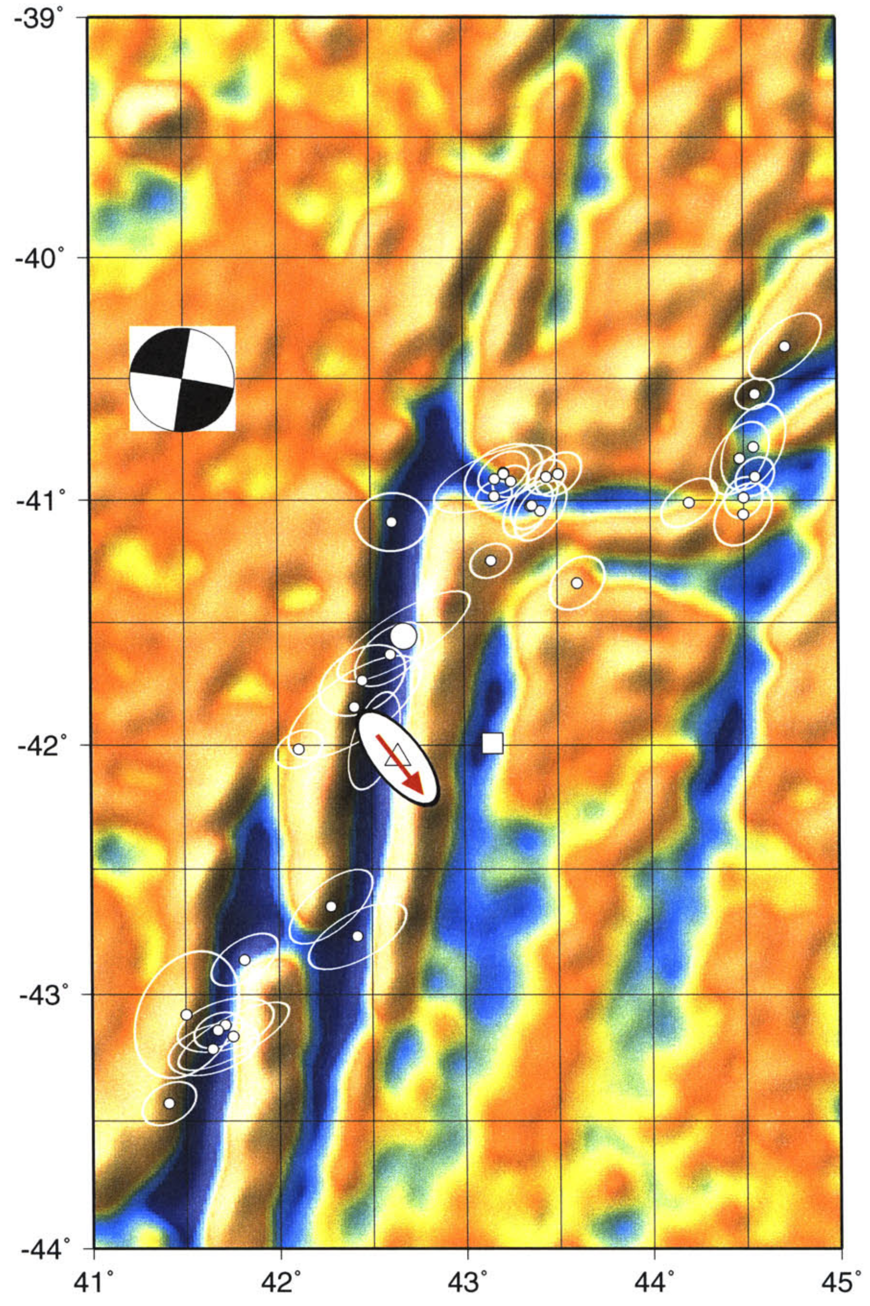

Figure 6-8: Map of the N-S trending Discovery II transform in the Southwest Indian Ocean. Colors are the satellite altimetric free-air gravity field (Sandwell and Smith, 1997) as in Figure 6-1. Relocated seismicity from the 1964-1996 ISC catalog is shown as small circles with 95% confidence ellipsoids. The large circle and square are the locations of the epicenter and mainshock of the 1997 event determined in Chapter 2. The triangle shows the event's centroid location. The white ellipse with black border denotes the map-view projection of the characteristic rupture volume defined by our estimate of this event's 2nd spatial moment. The red vector denotes its average directivity as specified by the mixed space-time moment. The vector's length has been scaled to equal τ_c x v_0.

consistent with both the moment-tensor and the directivity determined in Chapter 3 if two sub-parallel N-S striking faults ruptured coseismically.

The Discovery II transform is a double transform connected by a small spreading segment at about 42.75°S. It also has an adjacent fault-valley that can be traced for ~200 km on both-sides of the ridge (Figure 6.8). This pair of valleys most-likely represents the fracture zone associated with a paleo-transform fault since the SWIR shows no current offset at its projected intersection with these valleys. The 1997 earthquake began with a slow, smooth episode of moment release on the main transform that was followed ~12 s later by an ordinary mainshock (Chapter 3). The location of the mainshock determined in Chapter 3 falls within the adjacent fault-valley indicating that this fault ruptured in the 1997 earthquake (Chapter 3; Figure 6-8). Thus both the NW-SE orientation of the 2nd moments and the directivity study in Chapter 3 suggest that the 1997 Prince Edward Island earthquake was a complex faulting event that ruptured both the main trace of the Discovery II transform and the adjacent paleotransform fault.

6.5 Possible Causes of the Off-Fault subevents

The 1994 Romanche and 1997 Prince Edward Island earthquakes share many similarities. They consist of a sequence of right-lateral, strike-slip subevents that rupture not only the respective main transform faults but also a sub-parallel fault about 40 km from each main transform. The events are also compound earthquakes consisting of not only one or more ordinary rupture events, but also a smooth transient of longer duration that preferentially radiates energy at low-frequencies (Chapters 2 and 3). Both event sequences began with a slow rupture that was followed by the main high-frequency subevent on the adjacent 'paleo-transform.' In the case of the Romanche event, precursory ramps in low-frequency P-wave forms indicate that the slow component began rupturing at least 100 seconds before the high-frequency subevents while for the Prince Edwards event, P-waveforms show that the slow component began approximately 10-15 seconds before the ordinary rupture. The observation that both events began with a slow component suggests the possibility that the slow component may have triggered the unusual failure of the paleotransform.

Coseismic rupturing of multiple widely separated faults in a single earthquake has been documented, most notably for the 1980, M_s 6.9, Irpinia, Italy, normal-fault earthquake. This event sequence propagated over at least three faults with each fault bringing the subsequent one closer to failure (Nostro *et al.*, 1997; Belardinelli *et al.*, 1999). The last fault to rupture in this event was ~20-25 km from the preceding fault that triggered its failure. The likelihood of failure of a potentially triggered fault is usually evaluated in terms of the change in Coulomb failure stress, Δ_f:

$$\Delta_f = \Delta\tau - \mu'\Delta\sigma \tag{6.1}$$

where μ' is the apparent coefficient of friction, $\Delta\tau$ and $\Delta\sigma$ are the change in shear and normal stress on the triggered fault resulting from slip on the source fault, respectively. Positive values of Δ_f promote failure; negative values inhibit failure. Δ_f can be considered as either a dynamic quantity associated with the affects of seismic-waves radiated by the source fault (Belardinelli *et al.*, 1999) or as the static level that remains after the transient seismic waves have disapated (Okada, 1992; King *et al.*, 1994). Fault slip as a response to static-stress changes has been well documented for geometries similar to the Romanche and Prince Edwards events. For instance, the 1989 Loma Prieta earthquake on the San Andreas fault triggered slip on the subparallel Calaveras fault at points ~15-25 km from the Loma Prieta rupture zone (McClellan, 1990). More recently, the 1998, M_w 8.2, strike-slip Antarctic event triggered off-fault aftershocks with similar focal mechanisms to the mainshock at distances over 80 km from the rupture zone (Toda and Stein, 1999). It is not clear whether static or dynamic stresses are more relevant in triggering secondary ruptures that begin very soon after the passage of the S-wave such as the Irpinia, Romanche, and Prince Edward Island events. However the peak dynamic and static stress changes usually have the same sign and similar geometric patterns (Belardinelli *et al.*, 1999). This should be particurly true for slow earthquakes where directivity effects are less likely to perturb the spatial pattern of the peak dynamic stresses. Therefore, we investigate wether the geometry of the Romanche and Prince Edward sequences, particuraly the subevents located on the paleo-transforms, can be explained by the static stress changes produced by the initial slow components.

6.5.1 Stress Triggering Calculations for the 1994 Romanche Event

To calculate Δ_f on one fault as a result of slip on another it is necessary to know the locations and focal mechanisms of both faults, the slip distribution on the source fault, and the effective friction coefficient on the receiver fault. For the 1994 Romanche event, the moment tensors of the slow component and the A and B subevents must be similar due to a lack of an observable frequency dependence in the event's moment tensor (McGuire *et al.*, 1996). The effective friction coefficient of the paleo-transform fault is unknown. We set $\mu = 0.8$, a value that provided a good fit to the aftershock distribution of the 1998 Antarctic earthquake which occurred in oceanic lithosphere Toda and Stein (1999). The locations of the A and B subevents are constrained by high-frequency travel-time picks (Figure 6-2A, Chapter 2), but the location of the slow-precursor could not be determined owing to the poor signal to noise ratio at low-frequencies (see Figure 2-4). One likely location for the slow-precursor is the seismic-gap on the main transform between about -22.25° and -23.5° longitude. No events in the ISC catalog between 1964 and 1996 locate in this region (Figure 6-2A) indicating that the fault may have unusual rupture properties in this area. This location also shows unusual morphology in the transform valley with the active fault trace changing strike by $\sim 18°$ near the location of a 1.5 km high ridge which interrupts the transform valley (Searle *et al.*, 1994). Owing to the unusual nature of this region, we choose to test whether a slow precursor occurring in this area would have increased the likelihood of failure of parallel strike-slip faults at the locations of the 94A and 94B subevents.

To calculate Δ_f at the 94A and 94B subevent locations, we used a variety of uniform slip source-models that represent the uncertainty in the seismic-moment, fault-width, and stress-drop for the slow-precursor. The stress drop uncertainty was parameterized in terms of α, the fault slip to length ratio, which ranges from about 10^{-4} to 10^{-5} (Scholz *et al.*, 1986). Δ_f was calculated for each of the source models using a vertical, right-lateral source fault, and assuming vertical, right-lateral receiver faults. The calculations were done assuming a finite dislocation in an elastic half-space (Okada, 1992; King *et al.*, 1994; Toda *et al.*, 1998). The position of the source fault was then shifted to find the location that maximized the sum of Δ_f at the 94A and 94B subevent locations, subject to the constraint that Δ_f be positive at both locations. The results (Table 6.5) indicate that a location for the slow precursor within the seismic gap can produce an increase in Δ_f at both subevent locations for each parameter combination. Figure 6-9 shows the results for parameter set 5 (Table 6.5). The spatial pattern of the predicted Δ_f values was similar for all cases tested. In particular, the lobe of positive Δ_f resulting primarily from an increase in shear stress along the strike of the fault overlapped the 94A location while the lobe of positive Δ_f resulting primarily from a decrease in normal-stress overlapped the 94B location. The values of Δ_f at the 94A location are generally smaller than those at the 94B location, but that difference would be lessened by a lower value of μ'.

The predicted values of Δ_f at the 94B location range from about .15 to .4 bars. This is in the range of Coulomb stress changes (.2 - 1.0 bars) which produced significant correlations with the seismicity rate changes following several earthquakes including the 1992 Landers, California, quake (Stein *et al.*, 1992) and the 1995 Kobe earthquake Toda *et al.* (1998). The magnitude of the Δ_f values is less important to this study than the spatial pattern. The uncertainties in subevent location, fault-zone rigidity, stress-drop, and slip distribution correspond to significant ($>$ a factor of 2) uncertainties in the Δ_f values. The calculation shown in Figure 6-9 is intended to show that the geometry of the static (and dynamic) stress changes is consistent with a slow-precursor in the seismic gap triggering the subevent on the offset paleo-transform. It is also interesting to note that a slow-precursor of similar size at the opposite, eastern end of the seismic gap would have increased Δ_f at the locations of

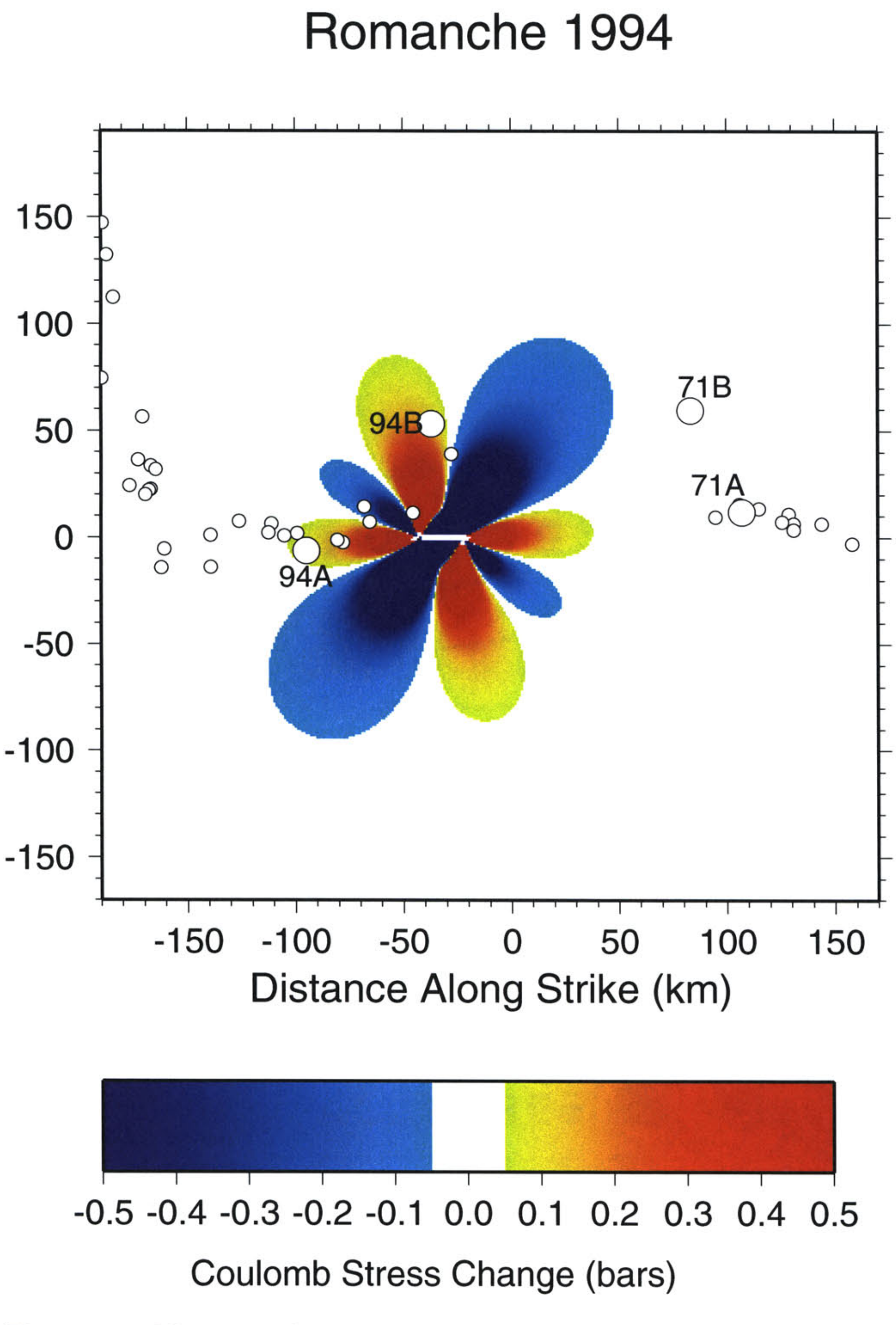

Figure 6-9: Map view showing the changes in Δ_f for run #5 of Table 6.5. The small circles denote the seismicity locations from Figure 6-2A. The large circles denote the subevent locations for the 1994 and 1971 events shown in Figure 6-2A. The horizontal axis denotes distance along the direction of strike of the main transform. The source and receiver faults were assumed to be vertical faults with this strike. The origin of the co-ordinate system is at 23.0°W and 1.0°S.

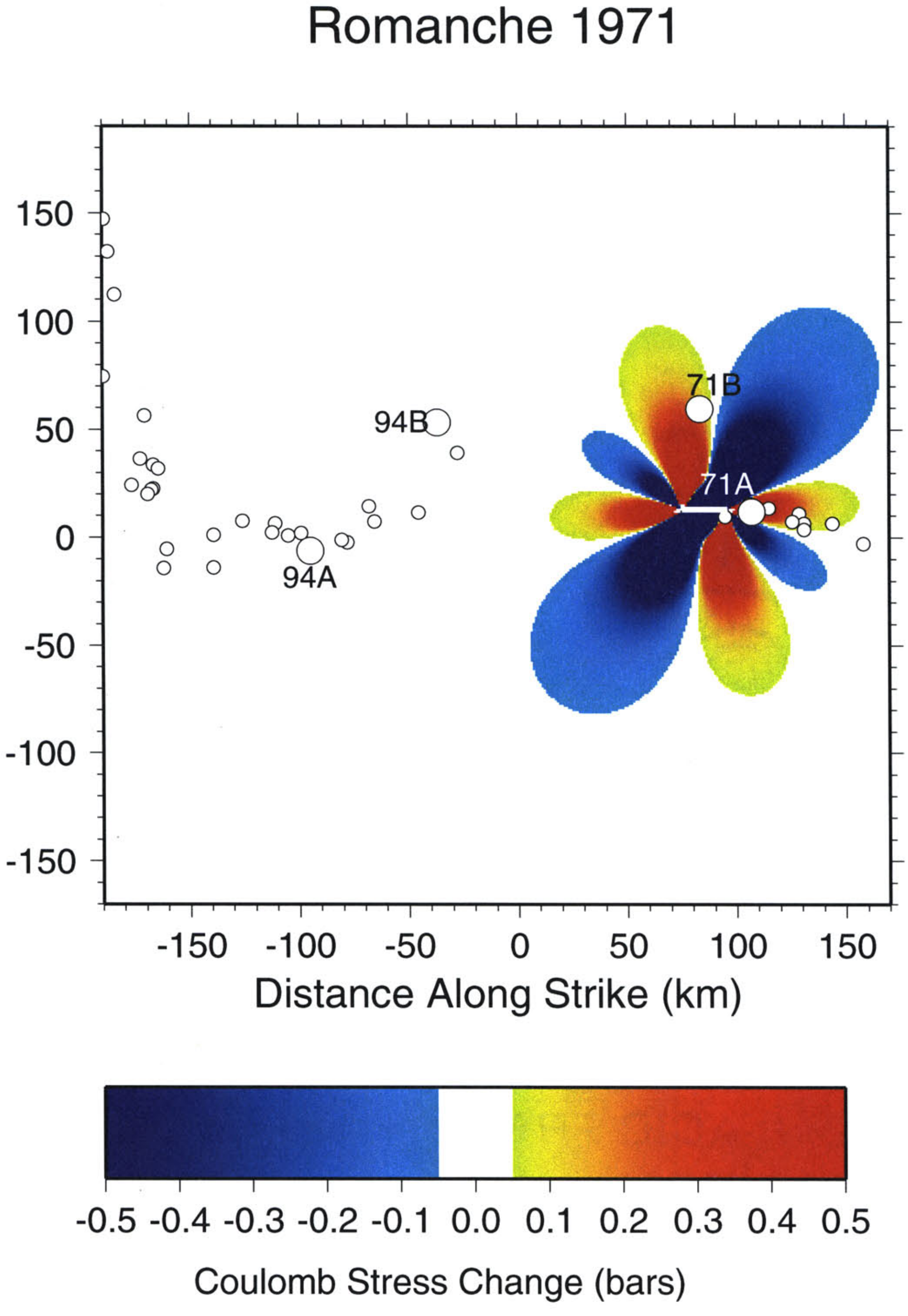

Figure 6-10: Map view showing the changes in Δ_f for run #5 of Table 6.5, but shifted to be aligned with the 1971 event's subevents. The small circles denote the seismicity locations from Figure 6-2A. The large circles denote the subevent locations for the 1994 and 1971 events shown in Figure 6-2A. The horizontal axis denotes distance along the direction of strike of the main transform. The source and receiver faults were assumed to be vertical faults with this strike. The origin of the co-ordinate system is at 23.0°W and 1.0°S.

Coulomb Stress Changes Resulting from the 1994 Romanche Slow Precursor

Run	M_0	Depth (km)	α	L (km)	slip (m)	Shift (km)	Δ_f at A	Δ_f at B
1	0.7	0-5	.00001	65.13	.6513	-12	.027	.096
2	0.7	0-5	.00005	29.13	1.456	-22	.031	.179
3	0.7	0-5	.0001	20.60	2.059	-22	.030	.200
4	0.7	0-10	.00001	46.04	0.460	-17	.031	.140
5	0.7	0-10	.00005	20.60	1.030	-22	.033	.204
6	0.7	0-10	.0001	14.56	1.456	-22	0.33	.216
7	0.7	10-15	.00001	46.04	0.460	-32	.016	.086
8	0.7	10-15	.00005	20.60	1.030	-22	.033	.177
9	0.7	10-15	.0001	14.56	1.456	-22	.033	.186
10	1.4	0-5	.00001	92.11	.921	2	.039	.132
11	1.4	0-5	.00005	41.29	2.06	-17	.055	.302
12	1.4	0-5	.0001	29.13	2.912	-22	.062	.358
13	1.4	0-10	.00001	65.13	.6513	-12	.058	.193
14	1.4	0-10	.00005	29.13	1.45	-22	.068	.367
15	1.4	0-10	.0001	20.60	2.06	-22	.066	.409
16	1.4	10-15	.00001	65.13	.651	-12	.057	.166
17	1.4	10-15	.00005	29.13	1.45	-22	.067	.319
18	1.4	10-15	.0001	20.6	2.06	-22	.066	.354

where the M_0 values are x10^{19}Nm, the Δ_f values are in bars, and the values of L and slip were calculated assuming a rigidity of 3.3x10^{10} Pa. The "Shift" denotes the distance it was necessary to shift the center point of the source fault in the x direction of Figure 6-9 to obtain the optimum alignment.

both subevents of the 1971 (Figure 6-10). However, no low-frequency study has been done to evaluate whether such a precursor may have occurred in that earthquake.

6.5.2 Stress Triggering Calculations for the 1997 Prince Edwards Event

The 1997 Prince Edward Island event began with a ~30 s long smooth episode of moment release that was nearly devoid of high-frequency energy (m_b 4.2) despite having a moment-magnitude of 6.2 (Chapter 3). This unusual event preceded an ordinary mainshock that ruptured a sub-parallel paleotransform offset from the main transform by about 40 km. Using the small amount of high-frequency energy radiated by the slow component and a temporary seismic network in southern Africa, we were able to locate the epicenter of the slow component (Figure 6.8). From the centroid location (Figure 6.8), we infer that the ruptures propagated to the south. Thus, the fault orientation of the slow event is well constrained. However there is an uncertainty in the fault width and stress drop of the event. For large widths (10 km) and high-stress drops the mainshock is in a region of negative Δ_f (Figure 6-11). However, for crustal scale widths (5 km) and low stress drops, the location of the mainshock is near the boundary between positive and negative values of Δ_f (Figure 6-11). Owing to the uncertainties in event location and fault zone rigidity, the 97B subevent location could be in either a region of positive or negative Δ_f for the low-stress drop case.

6.6 Discussion

While the primary traces of the Romanche and Discovery II transforms clearly are the plate-boundaries accommodating the majority of plate motion, it appears that the adjacent sub-parallel paleotransform faults may be accommodating a portion of the plate motion. We lack sufficient information about the slow-components of the 1994 Romanche and 1997 Prince Edwards events to perform a more detailed calculation of the static and dynamic stress fields resulting from these events. However, it appears that in both cases, the faulting geometry was most likely consistent with a triggering explanation. Triggering due to static stress changes has several unresolved issues with regard to these events. First the complete lack of teleseismically recorded aftershocks for the 1994 Romanche event (McGuire *et al.*, 1996) indicates that triggering of seismicity by static stress changes may not be a commonly occurring phenomenon on these faults. Secondly, static stress changes do not predict the close association in time of the slow and fast components of the Romanche and Prince Edwards sequences. Thus, the peak dynamic stresses, which shows a similar spatial pattern to the static stress, may be more important in explaining the triggering of the off-fault subevents.

The apparent activity of the "paleotransform" faults has several interesting implications for both fault mechanics and tectonics problems. The paleotransforms

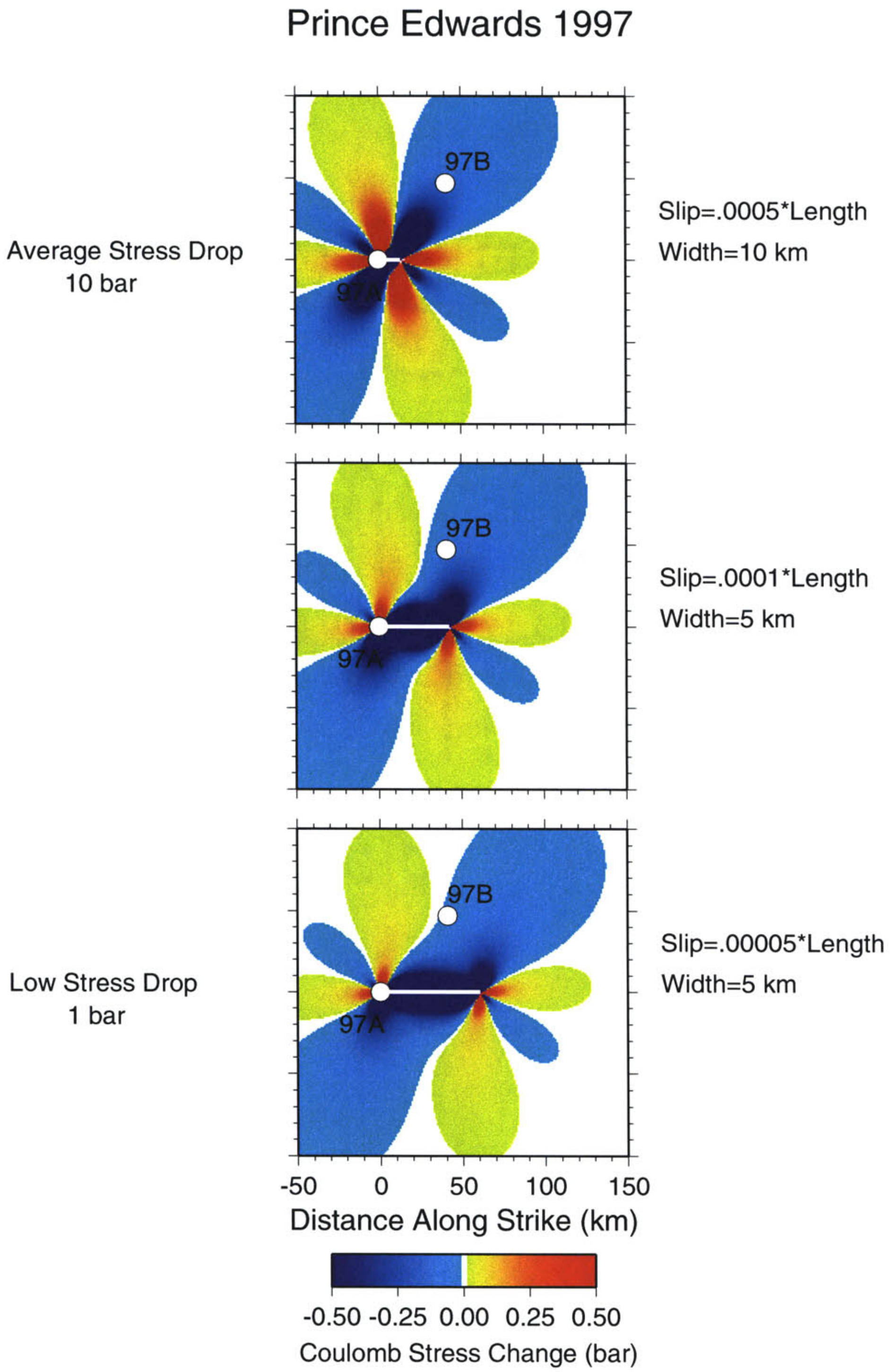

Figure 6-11: Map view showing the changes in Δ_f for run #5 resulting from the 1st 15 s of the 1997 Prince Edward Island slow earthquake. The large circles denote the subevent locations for the slow component (97A) and mainshock (97B). The horizontal axis denotes distance along the direction of strike of the main transform. The source and receiver faults were assumed to be vertical faults with this strike. The origin of the co-ordinate system is at the epicenter of the slow component.

adjacent to the Romanche and Discovery II transform faults appear to have been the primary plate-boundaries until ~5-10 Ma and possibly even more recently. Thus the rate at which they strengthen and heal is related to the occurrence of the off-fault seismicity. After a transform fault passes a RTI, it appears to take approximately 2-4 Ma to completely heal as evidenced by seismicity (Figure 6.2D) and gravity studies Wessel and Haxby (1990). Thus it's not unreasonable that a fault could continue slipping for a few Ma after it ceases to be the primary plate boundary. In fact, the stress perturbations resulting from large earthquakes on the main transform will systematically bring regions of the paleo-transform closer to failure. Thus, once a system of multiple sub-parallel faults is formed, the secondary fault(s) may be forced to remain active for a period of time until it completely heals, thus causing a distribution of plate-motion over a wider region than simply the primary transform valley. While the proposed activity of multiple faults is somewhat speculative, it clearly warrants further study using marine geologic, geodetic, and ocean bottom seismometer based methods.

Acknowledgments. We thank Ross Stein and Shinjie Toda for making their coulomb stress change code available. All figures were generated using the GMT software freely distributed by Wessel and Smith (1991).

Chapter 7

Summary and Future Directions

The studies of the 1994 Romanche and 1997 Prince Edward's Island events presented in Chapters 2, 3, and 6 demonstrate the unusual properties of slow earthquakes. In particular, the high-quality recordings of the Prince Edward's Island earthquake by seismometers in southern Africa provide extremely clear evidence for the existence of episodes of fault-slip that occur in such a way as to allow significant moment release while generating almost no high-frequency radiation. The existence of these episodes of smooth moment release presents several questions about the mechanical processes that cause this unusual form of moment-release. First, why is there an apparently causative relationship between the slow and ordinary components of the Romanche and Prince Edward's Island events? The close association in space and time of the two types of rupture suggests some sort of remote triggering of the ordinary subevent by either the dynamic or static stress-field generated by the slow rupture. While the calculations in Chapter 6 suggest that the geometry may be correct for this type of explanation, more detailed calculations will require an accurate knowledge of the space-time slip distributions of the slow and fast components of transform fault earthquakes. Secondly, what frictional process allows for propagating slip instabilities but limits the moment acceleration, $\ddot{M} \approx \mu W v_r \Delta \dot{u}$, to be orders of magnitude smaller during the slow components than in the ordinary subevents?

Both of the above questions are unanswered because the slow earthquake problem remains data limited. The observation made by Okal and Stewart (1982) 20 years ago that some oceanic transform fault events are deficient in high-frequency radiation and that these events have complex, long-duration source-time-functions has remained difficult to convert into insight about the mechanical processes responsible for slow rupture. This is primarily due to the lack of high-quality recordings of the high-frequency energy radiated by these events. The Prince Edward's Island event demonstrates the advances in determining of quantities like $\dot{M}(t)$ that can be made when the high-frequency radiation of the slow component can be constrained by regional data. Clearly the next step in investigating these events is to acquire high-quality broadband data from ocean bottom seismometers (OBS) located near a slow-rupture. This type of data should allow for accurate determinations of the quantities, such as the rupture velocity, the rigidity of the fault zone material, and the slip history (rise time) at a particular point, that will constrain the mechanical processes that occur during a "slow" rupture. The recent improvements in OBS technology and the new instrument pool should allow for the type of long term deployments necessary for seafloor based studies of earthquake dynamics and mechanics.

The method developed in Chapters 4 and 5 for determining the 2nd moments of earthquake space-time distributions provides a systematic way to catalog the extent, duration, and directivity of earthquake ruptures on a global scale. Currently, the method has two primary limiting factors that lead to a lack of resolution in the inverse problem, the global station distribution and the affects of unmodeled lateral heterogeneity. The global station distribution is continually improving, and the progress made between the early nineties and the mid-nineties was sufficient to begin determining 2nd moments. Further additions of stations in the southern hemisphere will continue to improve our resolution of the 2nd moments. Improvement in our ability to remove the affects of lateral heterogeneity by more accurate forward modeling is also possible. While the phase-delays of the fundamental-mode Rayleigh waves in our synthetics are well predicted by using degree 40 maps of the variation in elastic structure Ekström *et al.* (1997), the synthetics used in this thesis have made no attempt to correct for 3-D variations in attenuation structure. Global surface-wave attenuation models have recently been developed and are currently being improved. Because the

2nd moments are primarily determined from amplitude anomalies, correcting for the spatial variation of attenuation should greatly improve our ability to measure signals resulting from the extended source properties of large earthquakes.

While the effects of lateral heterogeneity on low-frequency fundamental-mode surface waves can be modeled using asymptotic expressions, these corrections are only valid up to frequencies of about 20-30 mHz for the types of heterogeneity found in the crust and upper-mantle (Kennett and Nolet, 1990; Kennett, 1995). This will limit the resolution of 2nd moments using this type of data to earthquakes larger than about M_w 7.0. As computer speeds continue to increase, shifting the synthetic seismogram calculation to a mode-coupling or numerical wave-propagation formalism should allow the extension to higher frequencies and hence smaller earthquakes. Currently, the use of phases that are less affected by lateral heterogeneity, such as P-waves, should allow determination of the 2nd moments for M_w 6 and larger events. The 2nd moments of intermediate and deep earthquakes with $M_w \geq 6$ should also be resolvable using higher mode surface waves which are less affected by 3-D variations in crustal structure than fundamental mode waves.

In addition to systematically resolving the fault-plane ambiguity on a global scale (Chapter 5), the ability to determine the 2nd moments of an earthquake's rupture will be useful for a wide range of problems. One area that 2nd moments are clearly important for is identifying and constraining complex faulting events. As seen from the Aqaba, Romanche, and Prince Edward's Island events (Chapters 4 and 6), the 2nd moments of complex faulting events are not necessarily oriented along one of the fault-planes of the event's moment tensor. Rupture jumping is one of the fundamental processes governing earthquakes and directly impacts fundamental questions such as what controls the ultimate size of a rupture? It is difficult to constrain the details of ruptures that jump from one fault to another when only teleseismic data is available. This partially results from the uncertainty associated with the smoothing of the slip distribution applied to regularize teleseismic finite-fault inversions. We plan to use *a priori* knowledge of the 2nd moments of complex events as integral constraints to constrain inversions for the detailed properties of these ruptures without requiring any arbitrary choice of smoothing parameter.

Appendix A

Traveling Wave Representation of Normal Mode Summation Synthetics

Here we present an outline of the derivation of equation (13), the travelling wave representation of our synthetic seismograms. The expression for a synthetic seismogram due to a point source computed by the summation of normal-modes can be written:

$$\tilde{s}(\omega) = \sum_{n,l} \frac{-i}{{}_n\omega_l^2(\omega - {}_n\omega_l)} \, {}_nI_l^{\mathrm{R}} \, {}_nE_l^{\mathrm{S}} \, \frac{2l+1}{4\pi} P_{l0}(\cos\Delta) \, , \tag{A.1}$$

where n is the overtone number, l is the angular order number, P_{lm} is the associated Legendre polynomial, and ${}_nI_l^{\mathrm{R}}$ and ${}_nE_l^{\mathrm{S}}$ are differential operators related to the excitation of the kth mode (k=(n,l)) at the reciever and by the source respectively [*Zhao and Jordan*, 1998, Appendix A]. Using the Poisson sum formula [*Dahlen and Tromp*, 1998, Chapter 11] the sum over angular degree l can be transformed into an integral over continuous wave number λ:

$$\tilde{s}(\omega) = \sum_n \int \frac{-1}{\omega_n^2(\lambda)[\omega - \omega_n(\lambda)]} \frac{\lambda}{2\pi} e^{i\lambda\pi} \sum_{j=0}^{\infty} (-1)^j e^{2ij\lambda\pi} I_n^{\mathrm{R}}(\lambda) E_n^{\mathrm{S}}(\lambda) P_{\lambda-\frac{1}{2}}(-cos\Delta)\, d\lambda\,. \tag{A.2}$$

Substituting in the asymptotic expression for $P_{\lambda-\frac{1}{2}}(-cos\Delta)$:

$$P_{\lambda-\frac{1}{2}}(-cos\Delta) \sim \frac{1}{\sqrt{2\lambda\pi sin\Delta}}\left(e^{i\lambda\Delta - i\lambda\pi + i\frac{\pi}{4}} + e^{-i\lambda\Delta + i\lambda\pi - i\frac{\pi}{4}}\right), \tag{A.3}$$

and preforming the contour integral in the upper half-plane gives:

$$\tilde{s}(\omega) = \sum_{j=0}^{\infty} \frac{i(-1)^j}{\omega^2\sqrt{2\pi \mathrm{sin}\Delta}} \sum_n \frac{\sqrt{\lambda_n}}{v_n(\lambda_n)} e^{i\lambda_n\pi + 2ij\lambda_n} I_n^{\mathrm{R}}(\lambda_n)\, E_n^{\mathrm{S}}(\lambda_n)\left(e^{i\lambda_n\Delta - i\lambda_n\pi + i\frac{\pi}{4}} + e^{-i\lambda_n\Delta + i\lambda_n\pi - i\frac{\pi}{4}}\right), \tag{A.4}$$

where λ_n is the wavenumber at which $\omega_n(\lambda) = \omega$, $v_n(\lambda_n)$ is the group velocity at λ_n, and the index j relates to the orbit number. The corrections made to our synthetics for lateral heterogeneity lead to a slight shift in the eigenfrequencies of the modes such that $\lambda_n \rightarrow \lambda_n + \delta\lambda_n$.

For first orbit waves j=0 and only the 1st exponential term (corresponding to waves travelling in the direction from the source to the reciever) is retained, leading to (13)

$$\tilde{s}(\omega) = \sum_n [A_n(\omega) + iB_n(\omega)] e^{i(\lambda_n + \delta\lambda_n)\Delta - i\pi/4}, \tag{A.5}$$

where the expressions for A_n and B_n are:

$$
\begin{aligned}
A_n = \frac{-\sqrt{\lambda_n}}{\omega^2 v_n(\lambda_n)\,\sqrt{2\pi \sin\Delta}} \{ & I_k^r E_k^r - \lambda_n^2 [I_k^r E_k^{\theta\theta}(\partial_{\theta_S}\Delta)^2 + I_k^r E_k^{\phi\phi}(\partial_{\phi_S}\Delta)^2 \\
& + I_k^r E_k^{\theta\phi}(\partial_{\theta_S}\Delta)(\partial_{\phi_S}\Delta) + 2I_k^\theta E_k^{\theta\theta}(\partial_{\theta_S}\Delta)(\partial_{\theta_R}\partial_{\theta_S}\Delta) \\
& + 2I_k^\theta E_k^{\phi\phi}(\partial_{\phi_S}\Delta)(\partial_{\theta_R}\partial_{\phi_S}\Delta) + I_k^\theta E_k^{\theta\phi}(\partial_{\theta_s}\Delta)(\partial_{\theta_R}\partial_{\theta_S}\Delta) + I_k^\theta E_k^\theta(\partial_{\theta_R}\Delta)(\partial_{\theta_S}\Delta) \\
& + I_k^\theta E_k^\phi(\partial_{\theta_R}\Delta)(\partial_{\phi_S}\Delta) + I_k^\theta E_k^{\theta\theta}(\partial_{\theta_R}\Delta)(\partial_{\theta_S}\partial_{\theta_S}\Delta) + I_k^\theta E_k^{\phi\phi}(\partial_{\theta_R}\Delta)(\partial_{\phi_S}\partial_{\phi_S}\Delta) \\
& + I_k^\theta E_k^{\theta\phi}(\partial_{\theta_R}\Delta)(\partial_{\theta_S}\partial_{\phi_S}\Delta) + 2I_k^\phi E_k^{\theta\theta}(\partial_{\theta_S}\Delta)(\partial_{\phi_R}\partial_{\theta_S}\Delta) + 2I_k^\phi E_k^{\phi\phi}(\partial_{\phi_R}\Delta)(\partial_{\phi_R}\partial_{\phi_S}\Delta) \\
& + I_k^\phi E_k^{\theta\phi}(\partial_{\phi_S}\Delta)(\partial_{\phi_R}\partial_{\theta_S}\Delta) + I_k^\phi E_k^{\theta\phi}(\partial_{\theta_S}\Delta)(\partial_{\phi_R}\partial_{\phi_S}\Delta) + I_k^\phi E_k^\theta(\partial_{\phi_R}\Delta)(\partial_{\phi_S}\Delta) \\
& + I_k^\phi E_k^\phi(\partial_{\phi_R}\Delta)(\partial_{\phi_S}\Delta) + I_k^\phi E_k^{\theta\theta}(\partial_{\phi_R}\Delta)(\partial_{\theta_S}\partial_{\theta_S}\Delta) + I_k^\phi E_k^{\phi\phi}(\partial_{\phi_R}\Delta)(\partial_{\phi_S}\partial_{\phi_S}\Delta) \\
& + I_k^\phi E_k^{\theta\phi}(\partial_{\phi_R}\Delta)(\partial_{\theta_S}\partial_{\phi_S}\Delta)]\},
\end{aligned}
\tag{A.6}
$$

$$
\begin{aligned}
B_n = \frac{-\sqrt{\lambda_n}}{\omega^2 v_n(\lambda_n)\,\sqrt{2\pi \sin\Delta}} [& \lambda_n [I_k^r E_k^\theta \partial_{\theta_S}\Delta + I_k^r E_k^\phi \partial_{\phi_S}\Delta + I_k^r E_k^{\theta\theta}\partial_{\theta_S}\partial_{\theta_S}\Delta \\
& + I_k^r E_k^{\phi\phi}\partial_{\phi_S}\partial_{\phi_S}\Delta + I_k^r E_k^{\theta\phi}\partial_{\theta_S}\partial_{\phi_S}\Delta \\
& + I_k^\theta E_k^\theta \partial_{\theta_R}\partial_{\theta_S}\Delta + I_k^\theta E_k^\phi \partial_{\theta_R}\partial_{\phi_S}\Delta + I_k^\theta E_k^\phi \partial_{\theta_R}\partial_{\phi_S}\Delta + I_k^\theta E_k^{\theta\theta}\partial_{\theta_R}\partial_{\theta_S}\partial_{\theta_S}\Delta \\
& + I_k^\theta E_k^{\phi\phi}\partial_{\theta_R}\partial_{\phi_S}\partial_{\phi_S}\Delta + I_k^\theta E_k^{\theta\phi}\partial_{\phi_R}\partial_{\theta_S}\partial_{\phi_S}\Delta + I_k^\theta E_k^r \partial_{\theta_R}\Delta + I_k^\phi E_k^\theta \partial_{\phi_R}\partial_{\theta_S}\Delta \\
& + I_k^\phi E_k^\phi \partial_{\phi_R}\partial_{\phi_S}\Delta + I_k^\phi E_k^{\theta\theta}\partial_{\phi_R}\partial_{\theta_S}\partial_{\theta_S}\Delta + I_k^\phi E_k^{\phi\phi}\partial_{\phi_R}\partial_{\phi_S}\partial_{\phi_S}\Delta + I_k^\phi E_k^{\theta\phi}\partial_{\phi_R}\partial_{\theta_S}\partial_{\phi_S}\Delta \\
& + I_k^\phi E_k^r \partial_{\phi_R}\Delta] - \lambda_n^3 [I_k^\theta E_k^{\theta\theta}(\partial_{\theta_R}\Delta)(\partial_{\theta_S}\Delta)^2 + I_k^\theta E_k^{\phi\phi}(\partial_{\theta_R})(\partial_{\phi_S}\Delta)^2 + I_k^\theta E_k^{\theta\phi}(\partial_{\theta_R}\Delta)(\partial_{\theta_S}\Delta)(\partial_{\phi_S}\Delta) \\
& + I_k^\phi E_k^{\theta\theta}(\partial\phi_R\Delta)(\partial_{\theta_S}\Delta)^2 + I_k^\phi E_k^{\phi\phi}(\partial_{\phi_R}\Delta)(\partial_{\phi_S}\Delta)^2 + I_k^\phi E_k^{\theta\phi}(\partial_{\phi_R}\Delta)(\partial_{\theta_S}\Delta)(\partial_{\phi_S}\Delta)]\},
\end{aligned}
\tag{A.7}
$$

where the source scalars are:

$$
E_k^r = M_{rr}\dot{U}_{n,\lambda_n-\frac{1}{2}}(r_S) + (M_{\theta\theta} + M_{\phi\phi})r_S^{-1}U_{n,\lambda_n-\frac{1}{2}}(r_S)\,, \tag{A.8}
$$

$$E_k^{\theta} = \frac{1}{r_S}\{M_{r\theta}Y_{n,\lambda_n-\frac{1}{2}}(r_S) - M_{r\phi}Z_{n,\lambda_n-\frac{1}{2}}(r_S) - \frac{\cos\theta_S}{\sin\theta_S}[M_{\phi\phi}V_{n,\lambda_n-\frac{1}{2}}(r_S) + M_{\theta\phi}W_{n,\lambda_n-\frac{1}{2}}(r_S)]\}, \tag{A.9}$$

$$E_k^{\phi} = \frac{1}{r_S\sin\theta_s}\{M_{r\phi}Y_{n,\lambda_n-\frac{1}{2}}(r_S) + M_{r\theta}Z_{n,\lambda_n-\frac{1}{2}}(r_S) - \frac{\cos\theta_S}{\sin\theta_S}[M_{\theta\phi}V_{n,\lambda_n-\frac{1}{2}}(r_S) - M_{\phi\phi}W_{n,\lambda_n-\frac{1}{2}}(r_S)]\}, \tag{A.10}$$

$$E_k^{\theta\theta} = \frac{1}{r_S}[M_{\theta\theta}V_{n,\lambda_n-\frac{1}{2}}(r_S) - M_{\theta\phi}W_{n,\lambda_n-\frac{1}{2}}(r_S)], \tag{A.11}$$

$$E_k^{\phi\phi} = \frac{1}{r_S\sin^2\theta_S}[M_{\phi\phi}V_{n,\lambda_n-\frac{1}{2}}(r_S) + M_{\theta\phi}W_{n,\lambda_n-\frac{1}{2}}(r_S)], \tag{A.12}$$

$$E_k^{\theta\phi} = \frac{1}{r_S\sin\theta_S}[2M_{\theta\phi}V_{n,\lambda_n-\frac{1}{2}}(r_S) + (M_{\theta\theta} - M_{\phi\phi})W_{n,\lambda_n-\frac{1}{2}}(r_S)], \tag{A.13}$$

with

$$Y_{n,\lambda_n-\frac{1}{2}}(r_S) = r_S\dot{V}_{n,\lambda_n-\frac{1}{2}}(r_S) - V_{n,\lambda_n-\frac{1}{2}}(r_S) + U_{n,\lambda_n-\frac{1}{2}}(r_S)\,, \tag{A.14}$$

$$Z_{n,\lambda_n-\frac{1}{2}}(r_S) = r_S\dot{W}_{n,\lambda_n-\frac{1}{2}}(r_S) - W_{n,\lambda_n-\frac{1}{2}}(r_S)\,, \tag{A.15}$$

and the reciever scalars are given by:

$$I_k^r = v_r U_{n,\lambda_n-\frac{1}{2}}(r_R) \quad , \quad I_k^{\theta} = v_{\theta}V_{n,\lambda_n-\frac{1}{2}}(r_R) - v_{\phi}W_{n,\lambda_n-\frac{1}{2}}(r_R)\,, \tag{A.16}$$

$$\mathrm{I}_{\mathrm{k}}^{\phi} = \frac{1}{\sin\theta_{\mathrm{R}}}[\mathrm{v}_{\phi}\mathrm{V}_{\mathrm{n},\lambda_{\mathrm{n}}-\frac{1}{2}}(\mathrm{r}_{\mathrm{R}}) + \mathrm{v}_{\theta}\mathrm{W}_{\mathrm{n},\lambda_{\mathrm{n}}-\frac{1}{2}}(\mathrm{r}_{\mathrm{R}})], \tag{A.17}$$

where $\boldsymbol{v} = (v_r, v_\theta, v_\phi)$ is the unit-directional vector of the instrument and a dot over an eigenfunction (U, V, W) represents a radial derivative. The source and reciever locations are $\boldsymbol{r}_S = (r_S,\ \theta_R,\ \phi_R)$ and $\boldsymbol{r}_R = (r_R,\ \theta_R,\ \phi_R)$. The expressions for even orbit waves, such as R2, are found from (A4) by taking the second exponential term with the appropriate values of j and the exponential term corresponding to waves travelling along the major arc in (A4).

Appendix B

Non-linear Constraints on the Moments

Here we show that the matrix inequality constraint we incorporate in our inversion (4-21) encompanses the constraint derived from Bessel inequalities by Bukchin (1995). For the planar fault case treated by Bukchin, equation 21 is equivalent to:

$$\begin{bmatrix} \hat{\boldsymbol{\mu}}^{(2,0)} & \hat{\boldsymbol{\mu}}^{(1,1)^{\mathrm{T}}} \\ \hat{\boldsymbol{\mu}}^{(1,1)} & \hat{\mu}^{(0,2)} \end{bmatrix} = \begin{bmatrix} \mu_{xx} & \mu_{xy} & \mu_{xt} \\ \mu_{xy} & \mu_{yy} & \mu_{yt} \\ \mu_{xt} & \mu_{yt} & \mu_{tt} \end{bmatrix} \geq 0\,, \tag{B.1}$$

where x and y are the cartesian spatial co-ordinates and t is the time co-ordinate. One property of a positive semi-definite matrix is that its upper left determinates are non-negative, ie:

$$\begin{vmatrix} \mu_{xx} & \mu_{xy} & \mu_{xt} \\ \mu_{xy} & \mu_{yy} & \mu_{yt} \\ \mu_{xt} & \mu_{yt} & \mu_{tt} \end{vmatrix} \geq 0\,, \tag{B.2}$$

and

$$\left|\hat{\boldsymbol{\mu}}^{(2,0)}\right| \geq 0\,. \tag{B.3}$$

The determinant in A2 is:

$$\mu_{xx}\mu_{yy}\mu_{tt} - \mu_{xx}\mu_{yt}^2 - \mu_{yt}^2\mu_{tt} + 2\mu_{xy}\mu_{xt}\mu_{yt} - \mu_{xt}^2\mu_{yy} \geq 0\,. \tag{B.4}$$

Solving for the second temporal moment assuming A3 holds gives:

$$\mu_{tt} \geq \frac{1}{\mu_{xx}\mu_{yy} - \mu_{xy}^2} \begin{bmatrix} \mu_{xt} & \mu_{yt} \end{bmatrix} \begin{bmatrix} \mu_{yy} & -\mu_{xy} \\ -\mu_{xy} & \mu_{xx} \end{bmatrix} \begin{bmatrix} \mu_{xt} \\ \mu_{yt} \end{bmatrix}, \tag{B.5}$$

which can be written in terms of the 2nd moments as:

$$\hat{\mu}^{(0,2)} \geq \hat{\boldsymbol{\mu}}^{(1,1)^T} \frac{1}{\left|\hat{\boldsymbol{\mu}}^{(2,0)}\right|} Adj(\hat{\boldsymbol{\mu}}^{(2,0)})\hat{\boldsymbol{\mu}}^{(1,1)} = \hat{\boldsymbol{\mu}}^{(1,1)^T} \hat{\boldsymbol{\mu}}^{(2,0)^{-1}} \hat{\boldsymbol{\mu}}^{(1,1)}\,, \tag{B.6}$$

where Adj denotes the adjoint of A. Equation B.6 is equivalent to the bessel inequality, eq. (4-24), of Bukchin (1995).

Appendix C

GSDF measurements and inversion fits

This appendix presents the measurements and inversion fits of the earthquakes studied in Chapter 5. Each page shows the $\delta\tau_p(\omega)$ (left-hand column) and $\delta\tau_q(\omega)$ (right-hand column) measurements. Each sub-plot is labeled with the seismic phase being measured (P or R1) and the nominal center frequency of the narrow band GSDF measurement. The 1995 Jalsico, 1997 Egypt, 1998 Antarctic, and 1995 Romanche events are not shown because their figures can be found in Chapters 4 and 6.

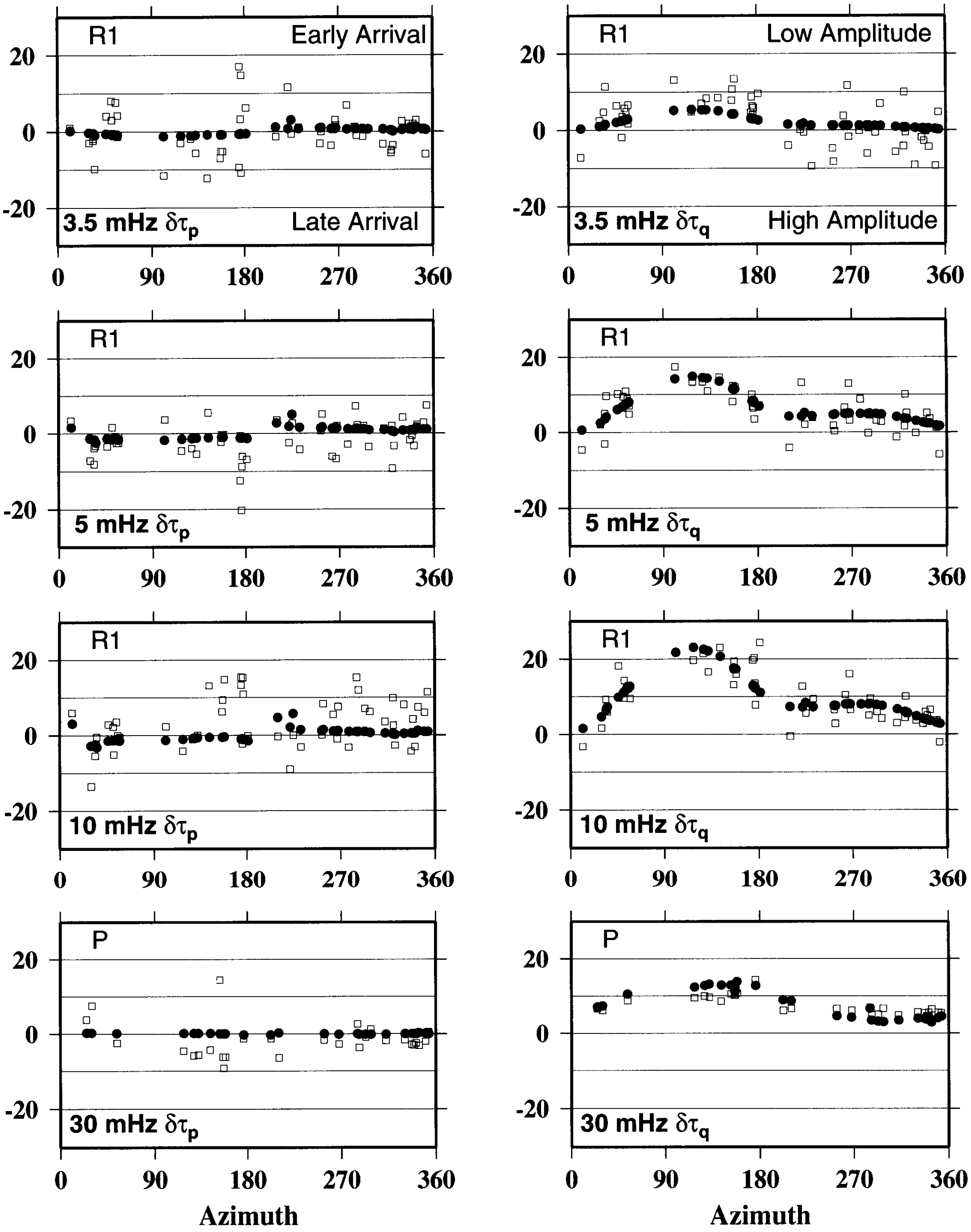

Figure C-1: GSDF measurements (open squares) and fits (solid circles) for the estimates of the 0th, 1st, and 2nd moments (Tables 5.1, 5.2, and 5.3) for the 1995 Japan earthquake.

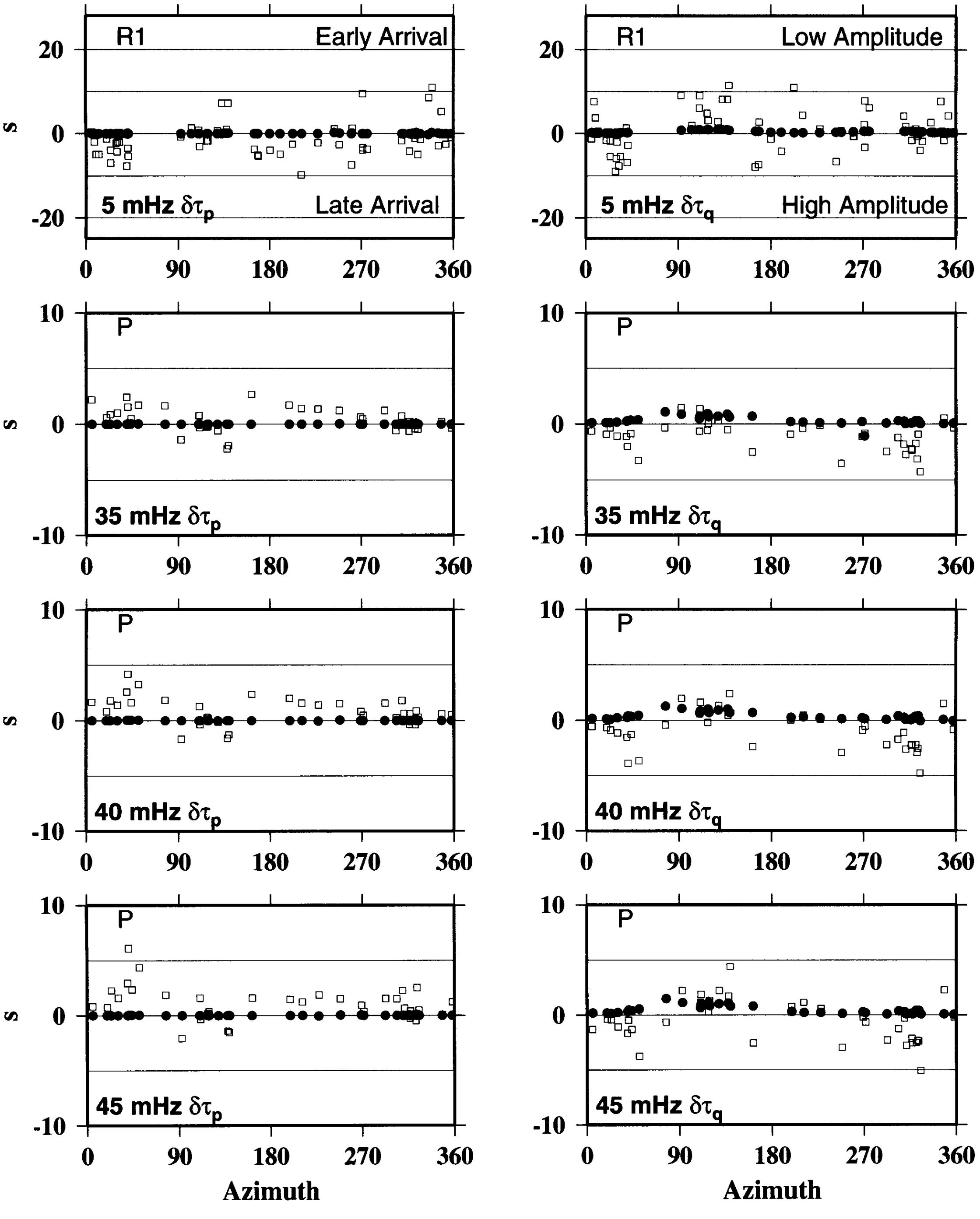

Figure C-2: GSDF measurements (open squares) and fits (solid circles) for the estimates of the 0th, 1st, and 2nd moments (Tables 5.1, 5.2, and 5.3) for the 1995 Burma earthquake.

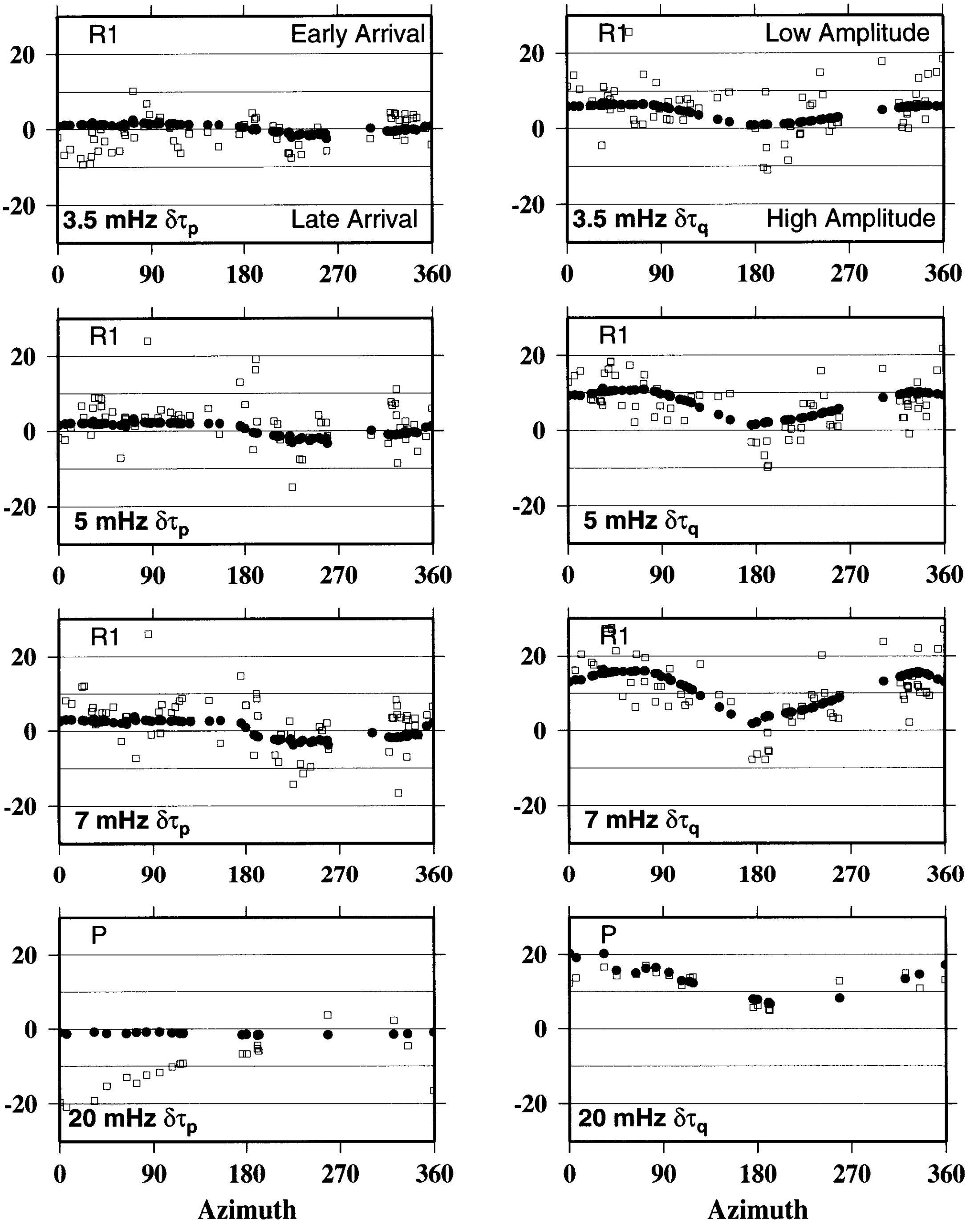

Figure C-3: GSDF measurements (open squares) and fits (solid circles) for the estimates of the 0th, 1st, and 2nd moments (Tables 5.1, 5.2, and 5.3) for the 1995 Chile earthquake.

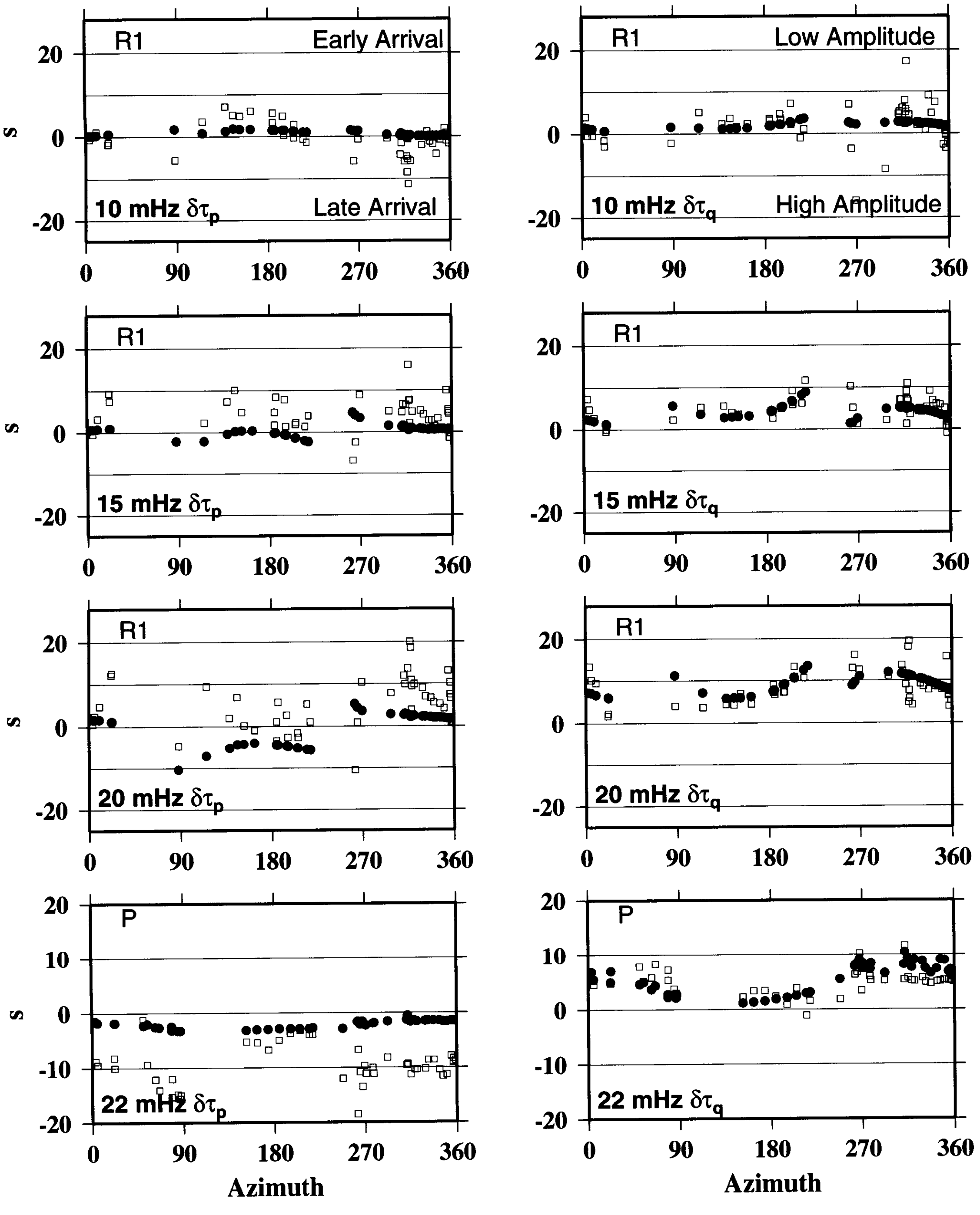

Figure C-4: GSDF measurements (open squares) and fits (solid circles) for the estimates of the 0th, 1st, and 2nd moments (Tables 5.1, 5.2, and 5.3) for the 1996 Alaska earthquake.

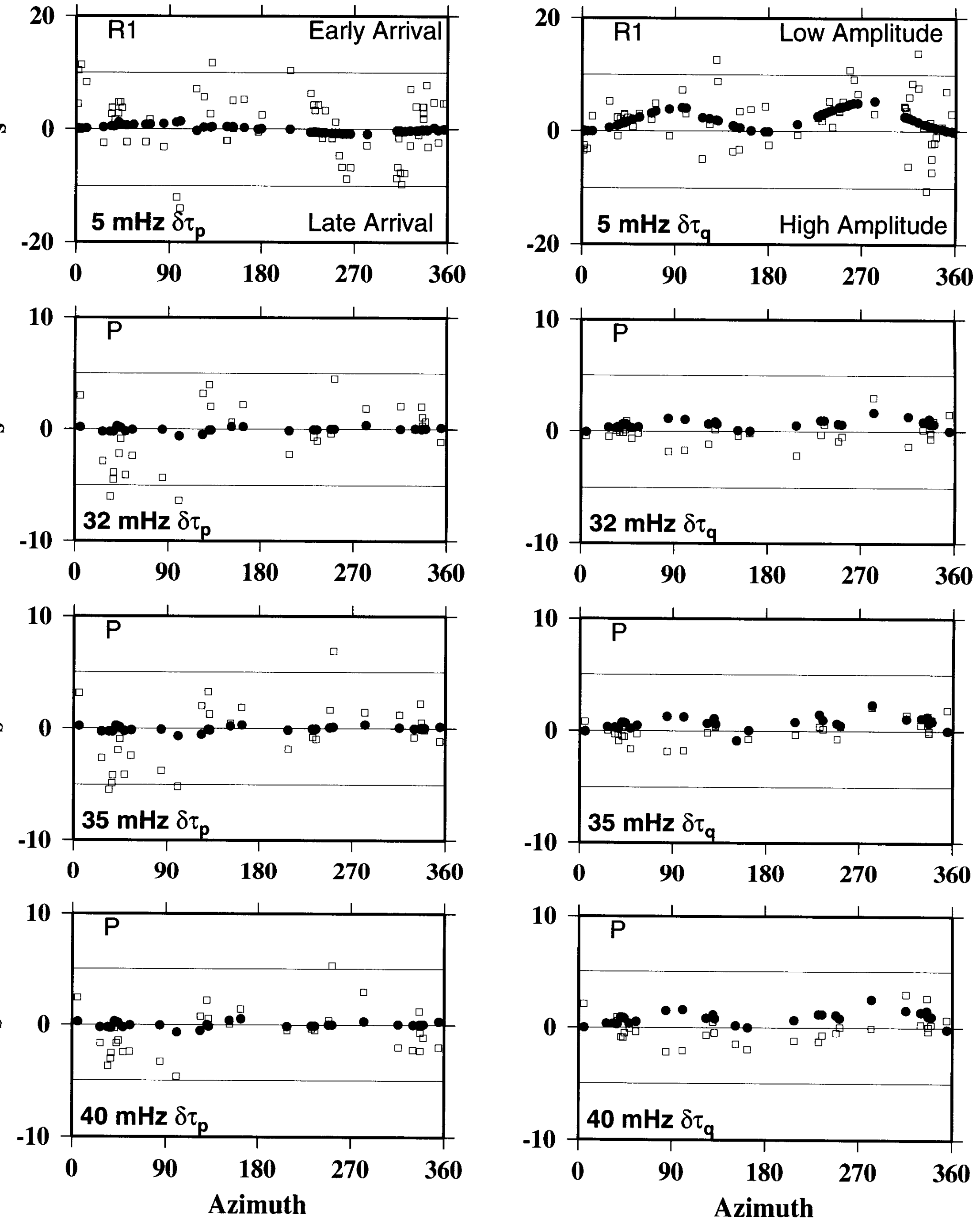

Figure C-5: GSDF measurements (open squares) and fits (solid circles) for the estimates of the 0th, 1st, and 2nd moments (Tables 5.1, 5.2, and 5.3) for the 1995 Rivera Transform earthquake.

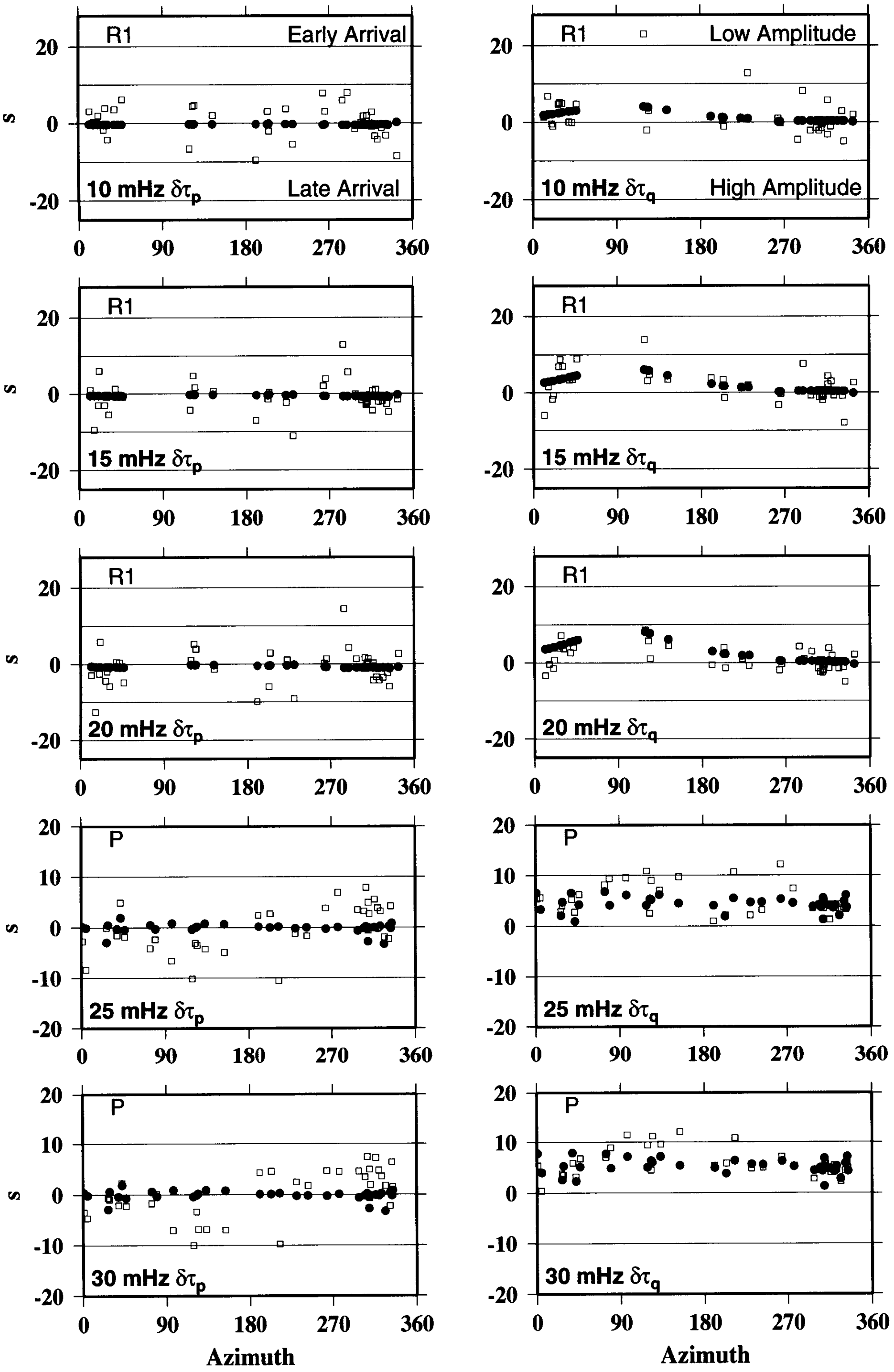

Figure C-6: GSDF measurements (open squares) and fits (solid circles) for the estimates of the 0th, 1st, and 2nd moments (Tables 5.1, 5.2, and 5.3) for the 1997 Tibet earthquake.

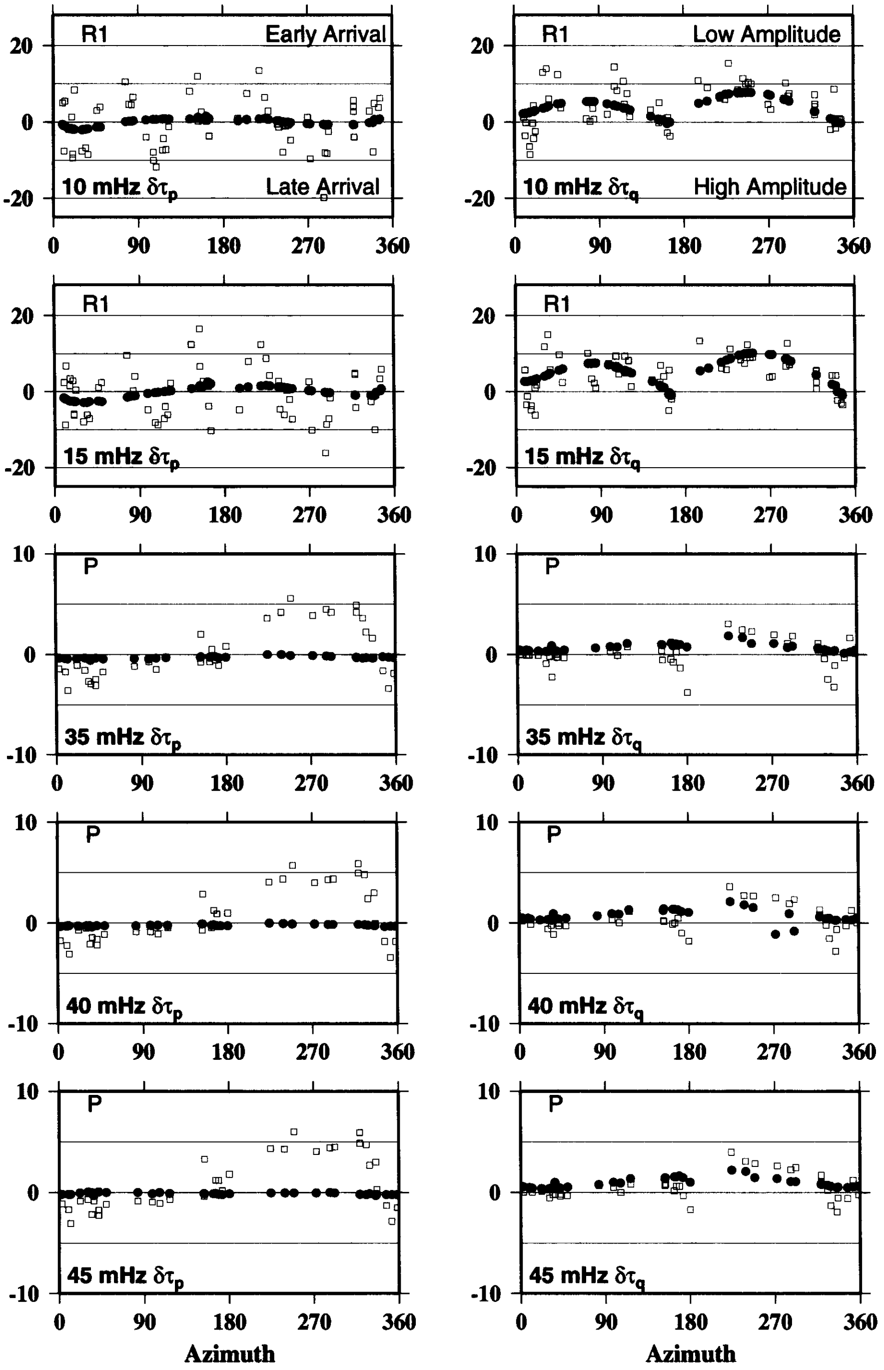

Figure C-7: GSDF measurements (open squares) and fits (solid circles) for the estimates of the 0th, 1st, and 2nd moments (Tables 5.1, 5.2, and 5.3) for the 1998 Equador earthquake.

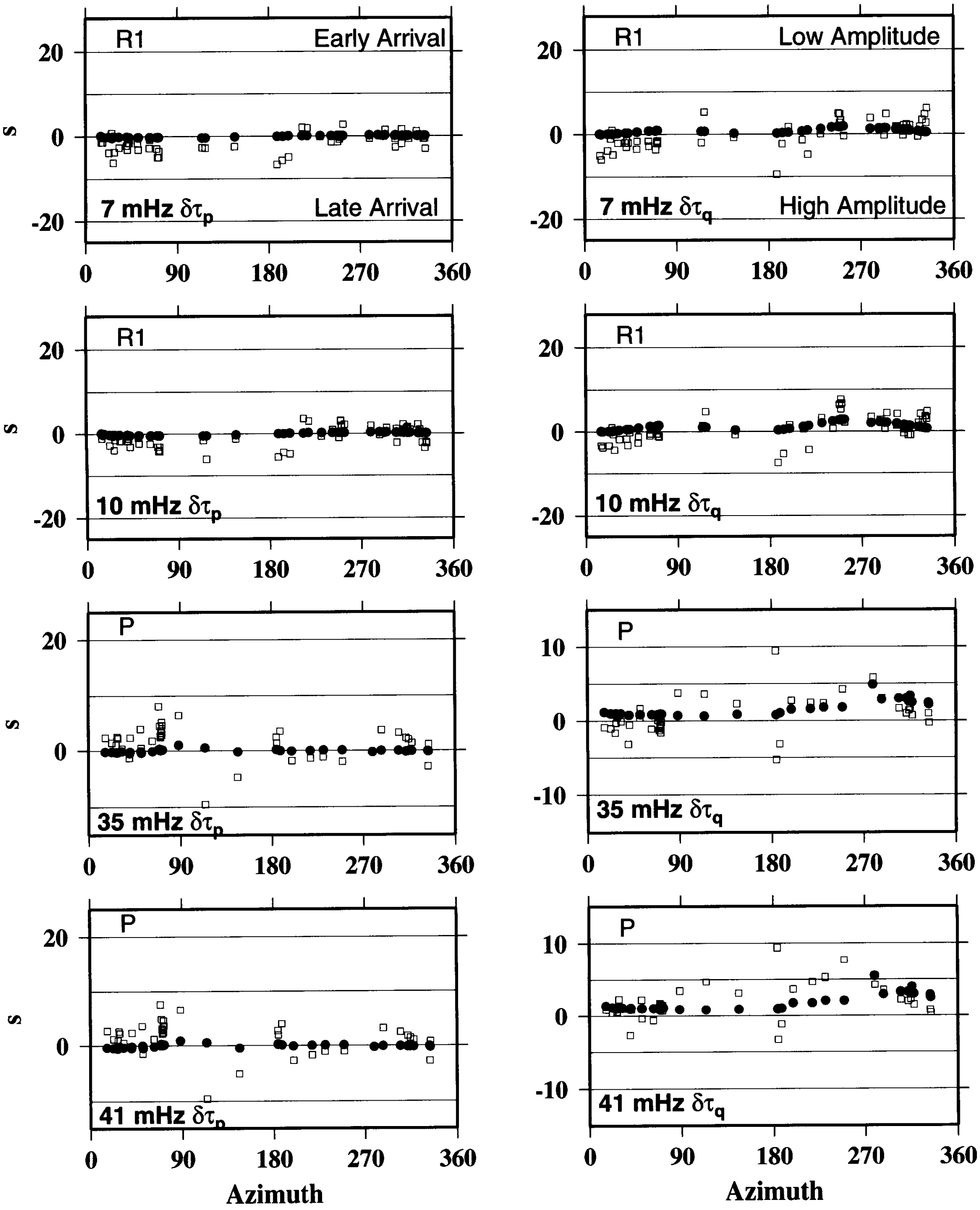

Figure C-8: GSDF measurements (open squares) and fits (solid circles) for the estimates of the 0th, 1st, and 2nd moments (Tables 5.1, 5.2, and 5.3) for the 1999 Izmit, Turkey earthquake.

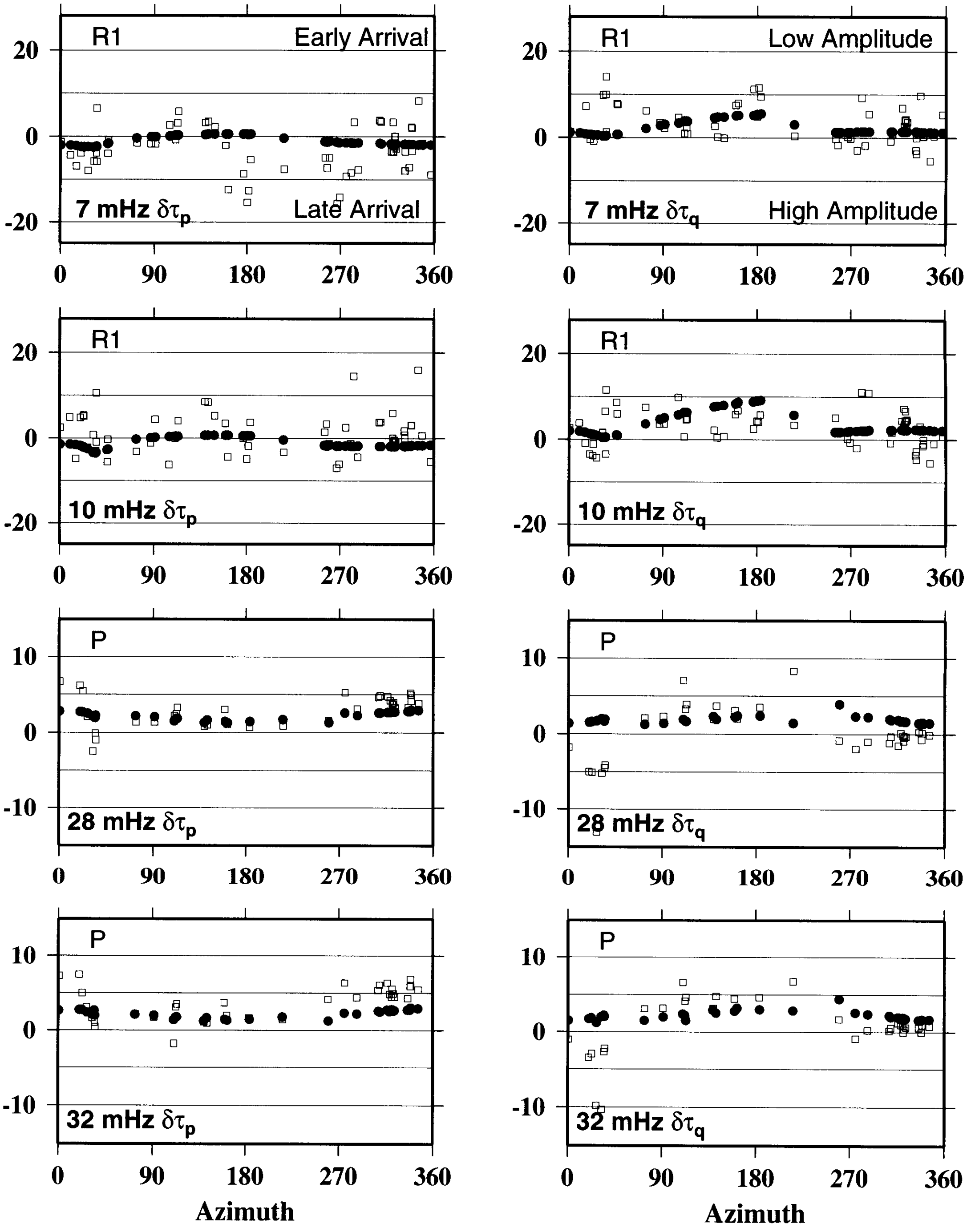

Figure C-9: GSDF measurements (open squares) and fits (solid circles) for the estimates of the 0th, 1st, and 2nd moments (Tables 5.1, 5.2, and 5.3) for the 1999 Taiwan earthquake.

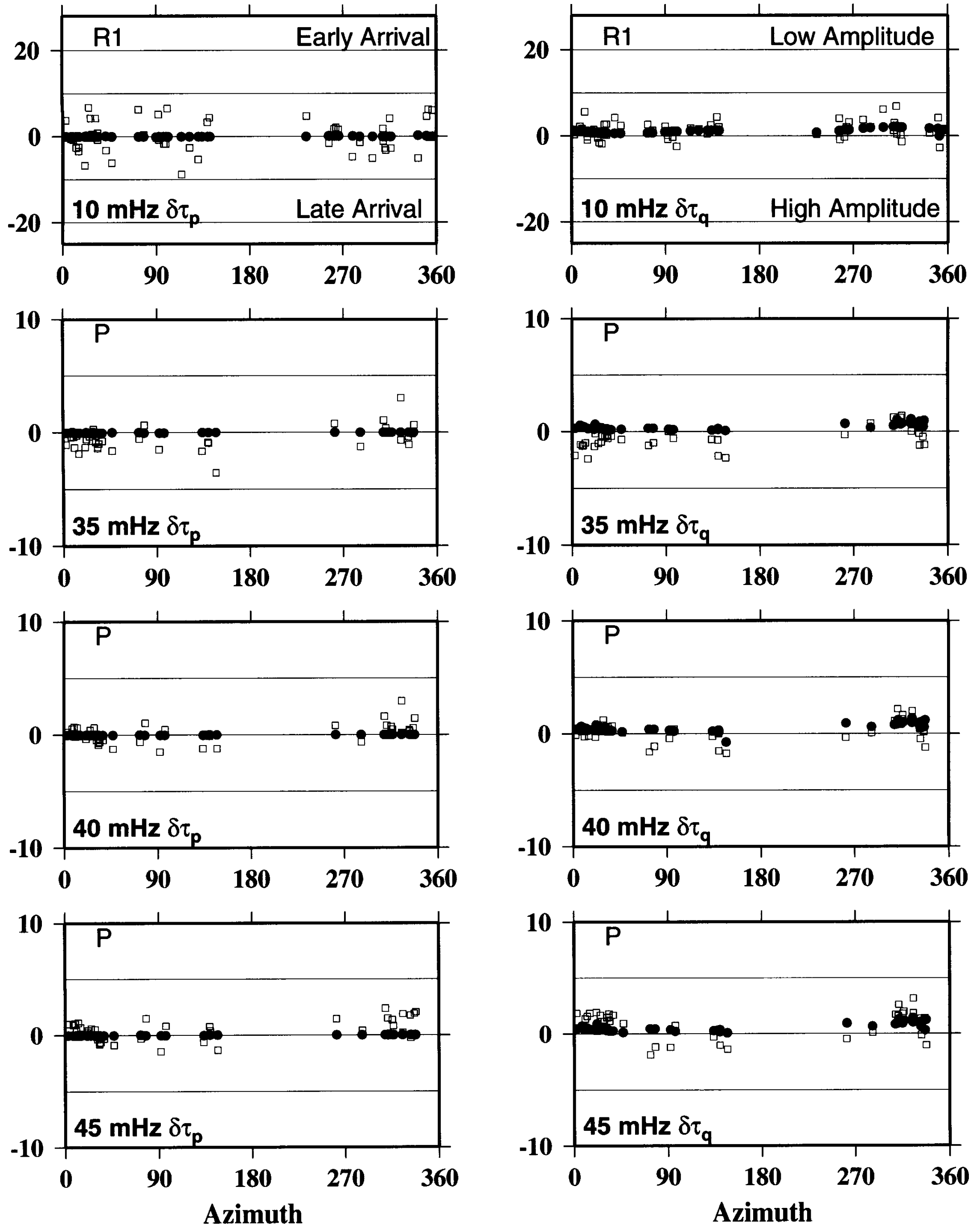

Figure C-10: GSDF measurements (open squares) and fits (solid circles) for the estimates of the 0th, 1st, and 2nd moments (Tables 5.1, 5.2, and 5.3) for the 1999 Hector Mine earthquake.

Bibliography

Abe, K. (1973). Tsunami and mechanism of great earthquakes. *Phys. Earth Planet. Inter.*, **7**, 143–153.

Abercrombie, R. E. and Ekstrom, G. (1999). Oceanic transform earthquakes: Slow or deep? *EOS*, **80**, 718.

Agnew, D. C. and Berger, J. (1978). Vertical seismic noise at very low frequencies. *J. Geophys. Res.*, **83**, 5420–5424.

Backus, G. and Mulcahy, M. (1976a). Moment tensors and other phenomenological descriptions of seismic sources–i. continuous displacements. *Geophys. J. R. astr. Soc.*, **46**, 341–361.

Backus, G. and Mulcahy, M. (1976b). Moment tensors and other phenomenological descriptions of seismic sources–ii. discontinuous displacements. *Geophys. J. R. astr. Soc.*, **47**, 301–329.

Backus, G. E. (1977a). Interpreting the seismic glut moments of total degree two or less. *Geophys. J. R. astr. Soc.*, **51**, 1–25.

Backus, G. E. (1977b). Seismic sources with observable glut moments of spatial degree two. *Geophys. J. R. astr. Soc.*, **51**, 27–45.

Barka, A. (1999). The 17 august 1999 izmit earthquake. *Science*, **285**, 1858–1859.

Beck, S. L. and Ruff, L. J. (1984). The rupture process of the great 1979 Colombia earthquake: Evidence for the asperity model. *J. Geophys. Res.*, **89**, 9281–9291.

Belardinelli, M. E., Cocco, M., Coutant, O., and Cotton, F. (1999). Redistribution of dynamic stress during coseismic ruptures: Evidence for fault interaction and earthquake triggering. *J. Geophys. Res.*, **104**, 14,925–14,945.

Ben-Menahem, A. (1961). Radiation of seismic waves from finite moving sources. *Bull. Seismol. Soc. Am.*, **51**, 403–435.

Beroza, G. C. (1995). Seismic source modeling. *Reviews of Geophysics, Supplement*, pages 299–308.

Beroza, G. C. and Jordan, T. H. (1990). Searching for slow and silent earthquakes using free oscillations. *J. Geophys. Res.*, **95**, 2485–2510.

Bevington, P. R. and Robinson, D. K. (1992). *Data reduction and error analysis for the physical sciences.* McGraw-Hill, New York.

Bonafede, M., Boschi, E., and Dragoni, M. (1983). Viscoelastic stress relaxation on deep fault sections as a possible source of very long period elastic waves. *J. Geophys. Res.*, **88**, 2251–2260.

Bonatti, E. (1990). Subcontinental mantle exposed in the Atlantic Ocean on St Peter-Paul islets. *Nature*, **345**, 800–802.

Bonatti, E., Ligi, M., Gasperini, L., Peyve, A., Raznitsin, Y., and Chen, Y. J. (1994). Transform migration and vertical tectonics at the Romanche fracture zone, equatorial Atlantic. *J. Geophys. Res.*, **84**, 21779–21802.

Bonatti, E., Ligi, M., Borsetti, A. M., Gasperini, L., Nergri, A., and Sartori, R. (1996). Lower Cretaceous depositis trapped near the equatorial Mid-Atlantic Ridge. *Nature*, **380**, 518–520.

Bukchin, B. G. (1995). Determination of stress glut moments of total degree 2 from teleseismic surface wave amplitude spectra. *Tectonophysics*, **248**, 185–191.

Crescentini, L., Amoruso, A., and Scarpa, R. (1999). Constraints on slow earthquake dynamics from a swarm in central Italy. *Science*, **286**, 2132–2134.

Das, S. and Kostrov, B. V. (1997). Determination of the polynomial moments of the seismic moment rate density distributions with positivity constraints. *Geophys. J. Int.*, **131**, 115–126.

Doornbos, D. J. (1982a). Seismic moment tensors and kinematic source parameters. *Geophys. J. R. astr. Soc.*, **69**, 235–251.

Doornbos, D. J. (1982b). Seismic source spectra and moment tensors. *Phys. Earth Planet. Inter.*, **30**, 214–227.

Dreger, D. S. (1994). Empirical Green's function study of the January 17, 1994 Northridge, California earthquake. *Geophys. Res. Lett.*, **21**, 2633–2636.

Dziewonski, A. M. and Anderson, D. L. (1981). Preliminary reference Earth model. *Phys. Earth Planet. Inter.*, **25**, 297–356.

Dziewonski, A. M., Ekström, G., and Salganik, M. P. (1994). Centroid-moment tensor solutions for January-March 1994. *Phys. Earth Planet. Inter.*, **90**, 1–12.

Dziewonski, A. M., Ekström, G., and Salganik, M. P. (1996). Centroid-moment tensor solutions for January-March 1995. *Phys. Earth Planet. Inter.*, **93**, 147–157.

Dziewonski, A. M., Ekström, G., and Salganik, M. P. (1997). Centroid-moment tensor solutions for October-December 1995. *Phys. Earth Planet. Inter.*, **101**, 1–12.

Dziewonski, A. M., Ekström, G., and Materovskaya, N. N. (1999). Centroid-moment tensor solutions for January-March 1998, in press,. *Phys. Earth Planet. Inter.*

Ekström, G. (1989). A very broad band inversion method for the recovery of earthquake source parameters. *Tectonophysics*, **166**, 73–100.

Ekström, G., Tromp, J., and Larson, E. W. (1993). Measurements and models of global surface wave propagation. *Eos Trans. AGU*, **74** (43)(43), Fall Meet. Suppl., 438.

Ekström, G., Tromp, J., and Larson, E. W. (1997). Measurements and global models of surface wave propagation. *J. Geophys. Res.*, **102**, 8137–8157.

Ellsworth, W. and Beroza, G. (1995). Seismic evidence for an earthquake nucleation phase. *Science*, **268**, 851–855.

Fisher, R. L. and Sclater, J. G. (1983). Tectonic evolution of the southwest Indian Ocean since the mid-Cretaceous: Plate motions and stability of the pole of Antarctice/Africa for at least 80 myr. *Geophys. J. R. astr. Soc.*, **73**, 553–576.

Forsyth, D. W., Bechtel, T. D., and Stewart, L. M. (1986). Rupture of separate en echelon segments of an oceanic transform fault in a single earthquake. *Eos. Trans. AGU.*, **67**(16), 359.

Fox, P. J. and Gallo, D. C. (1984). A tectonic model for ridge-transform-ridge plate boundaries: Implications for the structure of oceanic lithosphere. *Tectonophysics*, **104**, 205–242.

Gaherty, J. B., Jordan, T. H., and Gee, L. S. (1996). Seismic structure of the upper mantle in a central pacific corridor. *J. Geophys. Res.*, **101**, 22,291–22,309.

Gee, L. S. and Jordan, T. H. (1992). Generalized seismological data functionals. *Geophys. J. Int.*, **111**, 363–390.

Gusev, A. A. and Pavlov, V. M. (1988). Determination of space-time structure of a deep earthquake source by means of power moments. *Tectonophysics*, **152**, 319–334.

Hanks, T. C. (1977). Earthquake stress drops, ambient tectonic stresses and stresses that drive plate motions. *Pure and Applied Geophysics*, **115**, 441–458.

Henry, C., Das, S., and Woodhouse, J. H. (2000). The March 25, 1998 Mw = 8.1 Antarctic Plate earthquake: Moment tensor and rupture history. *J. Geophys. Res.*, page in press.

Ide, S. and Takeo, M. (1997). Determination of constitutive relations of fault slip based on seismic wave analysis. *J. Geophys. Res.*, **102**, 37,379–27,391.

Ide, S., Takeo, M., and Yoshida, Y. (1996). Source process of the 1995 Kobe earthquake: Determination of spatio-temporalslip distribution by Bayesian modeling. *Bull. Seismol. Soc. Am.*, **86**, 547–566.

Ihmlé, P. F. (1994). *Teleseismic Study of Rupture Processes of Long Duration*. Ph.D. thesis, 238 pp, Mass. Inst. of Technol., Cambridge.

Ihmlé, P. F. (1998). On the interpretation of subevents in teleseismic waveforms: The 1994 bolivia deep earthquake revisited. *J. Geophys. Res.*, **103**, 17,919–17,932.

Ihmlé, P. F. and Jordan, T. H. (1994). Teleseismic search for slow precursors to large earthquakes. *Science*, **266**, 1547–1551.

Ihmlé, P. F. and Jordan, T. H. (1995). Source time function of the great 1994 Bolivia deep earthquake by waveform and spectral inversions. *Geophys. Res. Lett.*, **22**, 2253–2256.

Ihmlé, P. F., Harabaglia, P., and Jordan, T. H. (1993). Teleseismic detection of a slow precursor the the great 1989 Macquarie Ridge earthquake. *Science*, **261**, 177–183.

James, D. *et al.* (1998). Southern Africa Seismic Experiment: Initial results. *Eos Trans. AGU*, **79** (17), Spring Meet. Suppl., S228.

Jordan, T. H. (1991). Far-field detection of slow precursors to fast seismic ruptures. *Geophys. Res. Lett.*, **18**, 2019–2022.

Jordan, T. H. and Sverdrup, K. A. (1981). Teleseismic location techniques and their application to earthquake clusters in the south-central Pacific. *Bull. Seismol. Soc. Am.*, **71**, 1105–1130.

Kanamori, H. (1972). Mechanism of tsunami earthquakes. *Phys. Earth Planet. Inter.*, **6**, 346–359.

Kanamori, H. and Allen, C. R. (1986). Earthquake repeat time and average stress drop. In S. Das, J. Boatwright, and C. H. Scholz, editors, *Earthquake Source*

Mechanics, Geophys. Monog. Ser., vol. 37, pages 227–235. AGU, Washington, D. C.

Kanamori, H. and Anderson, D. (1975). Theoretical basis of some epirical relations in seismology. *Bull. Seismol. Soc. Am.*, **65**, 1073–95.

Kanamori, H. and Cipar, J. (1974). Focal process of the great Chilean earthquake. *Phys. Earth Planet. Inter.*, **9**, 128–136.

Kanamori, H. and Hauksson, E. (1992). A slow earthquake in the santa maria basin, california. *Bull. Seismol. Soc. Am.*, **82**, 2087–2096.

Kanamori, H. and Kikuchi, M. (1993). The 1992 nicaragua earthquake: a slow tsunami earthquake associated with subducted sediments. *Nature*, **361**, 714–716.

Kanamori, H. and Stewart, G. S. (1979). A slow earthquake. *Phys. Earth Planet. Inter.*, **18**, 167–175.

Katzman, R., Zhao, L., and Jordan, T. H. (1998). High-resolution, two-dimensional vertical tomography of the central pacific mantle using scs reverberations and frequency-dependent travel times. *J. Geophys. Res.*, **103**, 17,933–17,971.

Kawasaki, I., Asai, Y., Tamura, Y., Sagiya, T., Mikami, N., Okada, Y., Sakata, M., and Kasahara, M. (1995). The 1992 Sanriku-Oki, Japan, ultra-slow earthquake. *J. Phys. Earth*, **43**, 105–116.

Kedar, S., Watada, S., and Tanimoto, T. (1994). The 1989 Macquarie Ridge earthquake: seismic moment estimation from long period free oscillations. *J. Geophys. Res.*, **99**, 17893–17907.

Kennett, B. L. N. (1995). Approximations for surface-wave propagation in laterally varying media. *Geophys. J. Int.*, **122**, 470–478.

Kennett, B. L. N. and Nolet, G. (1990). The interaction ofthe s-wavefield with upper mantle heterogeneity. *Geophys. J. Int.*, **101**, 751–762.

Kikuchi, M. and Kanamori, H. (1991). Inversion of complex body waves -iii. *Bull. Seismol. Soc. Am.*, **81**, 2335–2350.

King, G. C. P., Stein, R. S., and Lin, J. (1994,). Stress changes and triggering of earthquakes. *Bull. Seismol. Soc. Am.*, **84**, 935–953.

Klinger, Y., Rivera, L., Haessler, H., and Christopre Maurin, J. (1999). Active faulting in the Gulf of Aqaba: New knowledge from the m_w 7.3 earthquake of 22 November 1995. *Bull. Seismol. Soc. Am.*, **89**, 1025–1036.

Kuge, K., Kikuchi, M., and Yoshiko, Y. (1999). Non-double-couple moment tensor of the March 25, 1998, Antarctic earthquake; composite rupture of strike-slip and normal faults. *Geophys. Res. Lett.*, **26**, 3401–3404.

Langston, C. A. and Helmberger, D. V. (1975). A procedure for modelling shallow dislocation sources. *Bull. Seismol. Soc. Am.*, **42**, 117–130.

Lawson, C. L. and Hanson, R. J. (1974). *Solving Least Squares Problems*. 340 pp., Prentice-Hall, Englewood Cliffs, N.J.

Linde, A. T., Gladwin, M. T., Johnston, M. J. S., Gwyther, R. L., and Bilham, R. G. (1996). A slow earthquake sequence on the San Andreas fault. *Nature*, **383**, 65–68.

McClellan, P. H. (1990). Triggered slip on the Calaveras fault during the magnitude 7.1 Loma Prieta, California, earthquake. *Geophys. Res. Lett.*, **17**, 1227–1230.

McGuire, J. J., Ihmlé, P. F., and Jordan, T. H. (1996). Time-domain observations of a slow precursor to the 1994 Romanche transform earthquake. *Science*, **274**, 82–85.

Melbourne, T., Carmichael, I., DeMets, C., Hudnut, K., Sanchez, O., Stock, J., Suarez, G., and Webb, F. (1997). The geodetic signature of the m8.0 oct. 9, 1995 jalisco subduction earthquake. *Geophys. Res. Lett.*, **24**, 715–718.

Naoki, K. and Kiwamu, N. (1998). Continuous excitation of planetary free oscillations by atmospheric disturbances. *Nature*, **395**, 357–360.

Nawa, K. (1998). Incessant excitation of the Earth's free oscillations. *Earth, Planets, Space*, **50**, 3–8.

Nettles, M., Wallace, T., and Beck, S. (1999). The March 25, 1998, Antarctic Plate earthquake. *Geophys. Res. Lett.*, **26**, 2097–2100.

Nostro, C., Cocco, M., and Belardinelli, M. E. (1997). Static stress changes in extensional regimes: An application to Southern Appennines (Italy). *Bull. Seismol. Soc. Am.*, **87**, 234–248.

Okada, Y. (1992). Internal deformation due to shear and tensile faults in a half-space. *Bull. Seismol. Soc. Am.*, **82**, 1018–1040.

Okal, E. A. (1982). Higher moment excitation of normal modes and surface waves. *J. Phys. Earth*, **30**, 1–31.

Okal, E. A. and Stewart, L. M. (1982). Slow earthquakes along oceanic fracture zones: Evidence for asthenospheric flow away from hotspots? *Earth Planet. Sci. Lett.*, **57**, 75–87.

Park, J. (1990). Radial mode observations from the 5/23/89 Macquarie Ridge earthquake. *Geophys. Res. Lett.*, **17**, 1005–1008.

Pavlov, V. M. (1994). On non-uniqueness of the inverse problem for a seismic source-ii. treatment in terms of polynomial moments. *Geophys. J. Int.*, **119**, 487–496.

Pelayo, A. M. and Wiens, D. A. (1990). The november 20, 1960 peru tsunami earthquake; source mechanism of a slow event. *Geophys. Res. Lett.*, **17**, 661–664.

Peltzer, G., Crampé, F., and King, G. (1999). Evidence of nonlinear elasticity of the crust from the mw 7.6 Manyi (Tibet) earthquake. *Science*, **286**, 272–276.

Pinar, A. and Turkelli, N. (1990). The november 20, 1960 peru tsunami earthquake; source mechanism of a slow event. *Tectonophysics*, **283**, 279–288.

Riedesel, M. A. and Jordan, T. H. (1989). Display and assessment of seismic moment tensors. *Bull. Seismol. Soc. Am.*, **79**, 85–100.

Riedesel, M. A., Jordan, T. H., Sheehan, A. F., and Silver, P. G. (1986). Moment-tensor spectra of the 19 Sept 85 and 21 Sept 85 Michoacan, Mexico, earthquakes. *Geophys. Res. Lett.*, **13**, 609–612.

Ruegg, J. C., Campos, J., Armijo, R., Barrientos, S., Briole, P., Thiele, R., Arancibia, M., Canuta, J., Duquesnoy, T., Chang, M., Lazo, D., Lyon-Caen, H., Ortlieb, L., Rossignol, J. C., and Serrurier, L. (1996). The Mw=8.1 Antofagasta (North Chile) Earthquake of July 30, 1995: First results from teleseismic and geodetic data. *Geophys. Res. Lett.*, **23**, 917–920.

Sacks, I. S., Linde, A. T., Snoke, J. A., and Suyehiro, S. (1981). A slow earthquake sequence following the Izu-Oshima earthquake of 1978. In *Earthquake Prediction, and International Review*, volume 4 of *Maurice Ewing Ser.*, pages 617–628. AGU.

Sandwell, D. T. (1995). Ocean basin tectonics revealed with declassified geosat altimeter data. *Eos, Trans. AGU*, **76** (46), Fall Meet. Suppl., F149.

Sandwell, D. T. and Smith, W. H. F. (1997). Marine gravity anomaly from Geosat and ERS 1 satellite altimetry. *J. Geophys. Res.*, **102**, 10039–10054.

Sato, T., Imanishi, K., and Kosuga, M. (1996). Three-stage rupture process of the 28 December 1994 Sanriku-Oki earthquake. *Geophys. Res. Lett.*, **23**, 33–36.

Scholz, C. H. (1990). *The Mechanics of Earthquake Faulting*. Cambridge Univ. Press, Cambridge.

Scholz, C. H., Aviles, C., and Wesnousky, S. G. (1986). Scaling differences between large interplate and intraplate earthquakes. *Bull. Seismol. Soc. Am.*, **76**, 65–70.

Searle, R. C., Thomas, M. V., and Jones, E. J. W. (1994). Morphologyand tectonics of the Romanche transform and its environs. *Mar. Geophys. Res.*, **16**, 427.

Shearer, P. M. (1994). Global seismic event detection using a matched filter on long-period seismograms. *J. Geophys. Res.*, **99**, 13,713–13,725.

Silver, P. G. and Jordan, T. H. (1982). Optimal estimation of scalar seismic moment. *Geophys. J. R. Astron. Soc.*, **70**, 755–787.

Silver, P. G. and Jordan, T. H. (1983). Total-moment spectra of fourteen large earthquakes. *J. Geophys. Res.*, **88**, 3273–3293.

Sonder, L. J. and Pockalny, R. A. (1999). Anomalously rotated abyssal hills along active transforms: Distributed deformation of oceanic lithosphere. *Geology*, **27**, 1003–1006.

Stein, R. S., King, G. C. P., and Lin, J. (1992). Change in failure stress on the southern San Andreas Fault system caused by the 1992 magnitude=7.4 Landers earthquake. *Science*, **258**, 1328–1332.

Su, W. J., Woodward, R. L., and Dziewonski, A. M. (1994). Degree 12 model of shear velocity heterogeneity in the mantle. *J. Geophys. Res.*, **99**, 6945–6980.

Suda, N., Nawa, K., and Fukao, Y. (1998). Earth's background free oscillations. *Science*, **279**, 2089–2091.

Tanioka, Y. and Gonzalez, F. I. (1998). The Aleutian earthquake of June 10, 1996 (Mw 7.9) ruptured parts of both the Andreanof and Delarof segments. *Geophys. Res. Lett.*, **25**, 2245–2248.

Tanioka, Y. and Ruff, L. J. (1997). Source time functions. *Seismological Research Letters*, **68**, 386–400.

Toda, S. and Stein, R. (1999). Stress triggering of aftersocks to the 1998 antarctic event. *Geophys. Res. Let., in press.*

Toda, S., Stein, R., Reasenberg, P. A., Dieterich, J. H., and Yoshida, A. (1998). Stress transferred by the 1995 M_w=6.9 Kobe, Japan shock: Effect on aftershocks and future earthquake probabilities. *J. Geophys. Res.*, **103**.

Tucholke, B. E. and Schouten, H. (1988). Kane fracture zone. *Marine Geophys. Res.*, **10**, 1–39.

Tukey, J. W. (1984). *The collected works of John W. Tukey.* Wadsworth, Belmont Calif.

Vandenberghe, L. and Boyd, S. (1996). Semidefinite programming. *SIAM Review*, **38**, 49–95.

Wald, D. J. and Heaton, T. H. (1994). Spatial and temporal distribution of slip for the 1992 landers, california, earthquake. *Bull. Seismol. Soc. Am.*, **84**, 668–691.

Wessel, P. and Haxby, W. F. (1990). Thermal stresses, differential subsidence, and flexure at oceanic fracture zones. *J. Geophys. Res.*, **95**, 375–391.

Wessel, P. and Smith, W. H. F. (1991). Free software helps map and display data. *Eos Trans. AGU*, **72**, 441, 445–446.

Wilcock, W. S. D., Purdy, G. M., and Solomon, S. C. (1990). Microearthquake evidence for extension across the Kane transform fault. *J. Geophys. Res.*, **95**, 15,439–15,462.

Woodhouse, J. H. and Dziewonski, A. M. (1984). Mapping the upper mantle: Three-dimensional modeling of Earth structure by inversion of seismic waveforms. *J. Geophys. Res.*, **89**, 5953–5986.